RADAR-BASED DRONE TRACK-BEFORE-DETECT AND CHARACTERISTICS ESTIMATION

MASTER THESIS REPORT

Xingzhuo LI

RADAR-BASED DRONE TRACK-BEFORE-DETECT AND CHARACTERISTICS ESTIMATION

MASTER THESIS REPORT

Dissertation

to obatin the degree of Master of Science
in Electrical Engineering
at Delft University of Technology
to be defended publicly on 24 August 2022

by

Xingzhuo LI

born in Chongqing, China

This thesis has been approved by

Promotor: Prof. DSc. A. Yarovoy

Thesis committee:

Prof. DSc. A. Yarovoy,	Technische Universiteit Delft
Dr. R.T. Rajan,	Technische Universiteit Delft
Dr. O.A. Krasnov,	Technische Universiteit Delft

CONTENTS

ABSTRACT

Powered by technological advances, commercial drones have wide applications in areas such as photography, search, and rescue. However, the popularity of drones has raised technical and safety challenges for drone management and supervision. Traditional detect-before-track sensing approaches have reduced performance due to drones' low radar cross section, low velocity, and high maneuverability, and a long integration time is required to perform the spectrogram-based drone characteristics estimation. In this thesis, a coherent electromagnetic scattering model of the drone is applied to the track-before-detect algorithm to provide a better detection performance in low signal-to-noise ratio (SNR) cases and jointly estimate the dynamic state of the drone, including range, velocity, rotation frequency, and signal intensity from drone body and rotors. With the help of tracking results, a fusion of spectrogram-based characteristics estimation approaches is developed to estimate the constructional parameters of the drone, and a novel model-based number of rotor and multi-rotation frequency estimation method is proposed. The algorithms are first verified with simulation data, achieving 85%-95% detection probability at the SNR level below 5 dB and an estimation accuracy up to 96% in the number of rotor estimation. The algorithms are also validated with the experimental data, achieving agreement with the estimation results.

keywords - radar, UAVs, track-before-detect, drone characteristics estimation, multi-rotation frequency estimation

1

INTRODUCTION

This chapter introduces the background, motivation, and problem statement of the research. Section 1.1 describes the background, current sensing approaches, and challenges for sensing of drones. Section 1.2 lists the gaps and research questions in radar-based drone detection and estimation work. Section 1.3 describes the contribution and novelties of the research. Finally, Section 1.4 gives an overview of the structure of the report.

1.1. BACKGROUND

Enabled by the rapid development of technology in communication, positioning, and navigation, unmanned aerial vehicles (UAVs), also known as drones, which were used mainly in military areas, now have increasing applications and are widely used commercially and recreationally. For instance, companies have started to use drones for advertisement, performing light shows, taking aerial photographs, and trying to use drones as communication devices carrying a wireless station to provide Internet access in rural areas [1]. During the COVID-19 period, more drone-based delivery networks are established to transport goods such as masks and medicines to improve the safety and capacity of delivery [2].

However, while providing such functionality, convenience and productivity, drones can be easily misused to violate privacy, enter restricted areas, and carry out cyber attacks such as hijacking the GPS system [3]. In addition, the explosion of the drone market has led to the use of drones outpace the make of regulations by the government and both ethical and safety challenges have been addressed by the public [4]. Therefore, there is an increasing interest and demand to detect, recognize, and identify the drones for the proper management and supervision.

Currently, many techniques have been applied for the sensing of drones and three widely applied approaches, which are acoustic sensors, computer vision, and radar are listed in Table 1.1 with a brief summary of the advantages and disadvantages of each type of sensing.

1

Detection technique	Advantages	Disadvantages
Acoustic signal	• Low cost • Can work in NLOS	• Require prior about noise • Require large database
Computer vision	• High accuracy • Low cost for basic camera sensors • Widely installed and available	• High cost for high precision camera • Require LOS • Performance impact by weather conditions
Radar	• Robust to weather Robust to light condition • Work in NLOS situation	• Small RCS • High path loss in mmWave bands

Table 1.1: Comparison of different techniques for drones sensing [6]

Acoustic sensors such as an array of microphones provide a low size, weight, power and cost solution for sensing of drones by capturing the sound of their rotating components and distinguishing them from other objects [5]. They can deal with non-line-of-sight (NLOS) situations if the drones are still audible. However, acoustic techniques for drone sensing are sensitive to background noise, and a large amount of data is required to build acoustic signatures of different drones for classification.

Computer vision with deep learning-based approaches nowadays can perform drone detection and classification with high accuracy and can deal with moderate changes of illumination, view of point, and scale of the target with low-cost camera sensors [7] [8]. However, such methods require line-of-sight working situation, direct and clear visibility of the target, and thus suffer from deteriorated performance when there is dust, rain, mist or the target is too far away, and the size becomes too small.

Radar sensors, which periodically generate and transmit electromagnetic waves and receive the backscattered signal from the target, are robust to light and weather conditions, capable of working in NLOS cases and long-range sensing, and thus are very effective in drone surveillance. By processing the received signal which is a time-shifted, phase-delayed version of transmitted signal, information such as range and velocity can be further extracted from the signal. However, there are difficulties for the detection and classification of drones with radar:

- Drones' low radar cross section (RCS) can make the power of the backscattered signal lower than other objects and thus can have a very low RCS and poor detection probability.

- Drones' low flying altitude and relatively low velocity could make them difficult to distinguish from other static or low-velocity clutter.

- Drones' high maneuverability could cause range migration during the long integration time processing.

In conclusion, the low RCS, low flying altitude, relatively low velocity, and high maneuverability of drones raise challenges for the detection and tracking of drones. Although many sensing signal processing techniques have been proposed for the drone surveillance sensing system, there still remain challenges due to the low-small-slow characteristics of drones.

1.2. PROBLEM FORMULATION

Based on the challenges listed in the previous section and the review of the literature from Chapter 2, the following summarize the recognized problems and research questions:

- Most of the literature uses the traditional energy-based constant false alarm rate (CFAR) method for drone detection and could suffer from a high false alarm rate or a high miss detection rate due to the small RCS and low SNR of drones.

- The electromagnetic models of drones are usually regarded as a point target with all rotors centered at one position, ignoring the geometry information of the drones, and thus lack the analysis of how the geometry and orientation would influence the Doppler spectrogram signatures.

- Very little research is done to analyze and estimate the number of rotors and corresponding rotation frequencies, which can be significant information providing both constructional and kinematic characteristics of the multipropeller drones for recognizing whether the drone is loaded, classifying which type of drone it is, or possibly further estimating the orientation and posture of the drone.

This thesis work will address these gaps, and the goal is formulated as follows:

To develop and implement a model-based detection algorithm that uses the track-before-detect (TBD) approach based on a particle filter with a more realistic model of drones than in previous studies, to improve the detection performance while jointly estimating the drone and blade reflectivities. Combine the TBD detections results with spectrum-based estimation methods to develop an algorithm for the estimation of constructional and kinematic characteristics of the drone including the number of propellers, their rotation frequencies, the number of blades per propeller, and the length of the blades. The developed algorithms have to be tested/validated with simulated and real radar data.

1

1.3. THESIS CONTRIBUTION
The main contributions and novelties of the proposed research are listed as follows:

- Improved thin-wire multipropeller drone model that considers the detailed design of the drone's geometry. The data simulated with this model have been used to the analysis of how the geometry and orientation of a drone affect the observed micro-Doppler pattern.

- Implemented a novel model-based TBD algorithm that deals with drone detection in cases of small RCS and low SNR.

- Developed a fusion of spectrum-based drone characteristics estimation algorithms in the united processing chain with the detection results from the TBD algorithm to estimate the constructional and kinematic characteristics of drones including the rotation frequencies of propellers, the number of blades per propeller, and the blade's length.

- Developed a novel model-based estimator with false alarms removal algorithms to jointly estimate the number of rotors, each rotor's rotation frequency, and each blade's initial orientation angle.

1.4. THESIS STRUCTURE
The rest of the report is structured as follows. Chapter 2 provides the review of the current research in the electromagnetic modeling of drones, their radar-based detection methods and characteristics estimation approaches. Chapter 3 introduces the radar signals and electromagnetic models of the drones, showing the signatures of the micro-Doppler patterns derived from the drones' radar measurement. Chapter 4 describes the entire pipeline of processing from TBD algorithms, spectrum-based characteristics, to the proposed number of rotor estimator. Then, the results of simulation and experimental data analysis are presented and discussed in Chapter 5. Finally, chapter 6 summarizes the results of the research work and potential future work.

2

LITERATURE REVIEW

This chapter describes the related works in radar-based drones detection and characteristics estimation. Section 2.1 reviews related work on drone detection and localization using energy-based, machine learning-based, and model-based approaches. In Section 2.2, the literature on drone characteristics is analyzed, which is similarly categorized into spectrogram-based, machine learning-based, and model-based methods. Section 2.3 summarizes the current challenges and limitations in drone detection and estimation and provides the novelty and contributions in this work.

2.1. DRONE DETECTION AND LOCALIZATION

Detection and tracking are precondition processing steps for drone characteristics estimation and classification. They provide the decisions of the presence of the drone from the measurements, where the targets are located, and how the targets are moving. The current radar-based drone detection techniques can be mainly separated into 3 categories:

Energy-based detector

In [9], the author first proposed the principle of CFAR detection, an energy-based adaptive detector that is now commonly used in radar systems. The backscattered electromagnetic signal could contain the echo of the target of interest, as well as unwanted clutter and noise. The energy detector directly analyzes the power of the returned signal and sets a threshold to determine whether the received signal originated from a target or not. In these detection procedures, false alarms can occur when a clutter is recognized as a detected target and CFAR adaptively adjusts this detection threshold to the required false alarm rate.

Basic cell-averaging CFAR (CA-CFAR) has the limitation that assumes homogeneous background noise, and thus the detection performance will decrease when there are adjacent targets or clutters. In [10], a review was given to the development of the CFAR such as Greatest of CA-CFAR, Smallest of CA-CFAR, and Ordered Statistic-CFAR which

are modified to deal with environment with interfering targets and clutter boundaries.

For more recent work, CFAR is widely used with some adjustment to deal with radar-based drone detection in different situations. In [11], a Frequency-Modulated Continuous Wave (FMCW) radar working at 24 GHz was used to measure the drone 10 meters away. A 2D CA-CFAR is applied to range-Doppler measurement with the power of clutter modeled as a Weibull distribution. In [12], the detection problem is addressed by implementing the joint range-Doppler-azimuth detection with a FMCW radar working in the C band. A 2D CA-CFAR is implemented in range-Doppler frames along with the angle of arrival estimation for additional improvement in detection verification.

Work from [13] further utilizes the information in the frequency domain of the measurement with CFAR to verify the detection results. The authors used a multistatic radar operating in the S band to measure the drone 60 meters away. The CA-CFAR is first implemented in the range-time profile for initial detection. The detected results include both drones and clutter in the background. Then the micro-Doppler signatures are used to discriminate the drone from the noise to remove the false alarms.

From the literature, the energy-based detector CFAR has been adjusted and improved to deal with different environments and clutters to discriminate drones from noise and clutters. However, such methods all require the measurement to have a good SNR of the target, and the proposed methods are only validated with measurements' SNR usually above 20 dB and still suffer from miss detections due to the fluctuation of the drone's RCS.

Machine Learning-based detector

In addition to CFAR related detection approaches, the prevalent applications of machine learning are also used in the detection of drones and address the problem as a binary classification - whether there is a presence of the drone or not.

In [14], the detection problem is addressed using an L-band holographic radar with a 32 by 8 element receiver array. The range and Doppler data are thresholded to provide a list of candidate detections. Then a decision tree based on the machine learning (ML) algorithm is implemented to remove false alarms, separating drones from clutter with extracted features, including the range, velocity, amplitude, and their derivations. The algorithm achieves 99% true positive accuracy of non-drone targets, but has an 18% miss detection rate due to using a threshold method for initial candidate detection.

Work from [15] considers the detection problem with a distributed radar system and exploits the micro-Doppler features from the cadence velocity diagram. Features are fed to the support vector machine (SVM) and labeled as drone absent and drone present. Additionally, classification results from previous N measurement segments are also considered to help verification and final detection decision, providing detection accuracy up to 99%. The limitation of the work is that only the presence of the drone is given and other information, such as the range and velocity of the drone, requires further estimation. There is also a lack of analysis of the SNR on the drone measurement.

Bayesian track-before-detect particle filter

A Bayesian TBD using particle filter is a weak target detection approach proposed in [16]. Compared to energy-based detection methods which apply a threshold to the

measurement data causing loss of information and miss detection of low SNR target, the TBD is directly applied to the raw measurement and with the help of tracking multiple measurements, the information is integrated to achieve a higher SNR for the detection decision. The algorithm provides a probability distribution of the target state and the probability of target presence.

In [17], TBD is implemented on radar video data dealing with a high-dimensional nonlinear and non-Gaussian problem. In the TBD model, the target state consists of range and velocity. A constant velocity model is used as the system dynamic model, and the measurement model represents the target power in the range-Doppler domain. In [18], a multiple model TBD is considered to detect and track the maneuvering weak target. A constant velocity model combined with a coordinate turn model with a probability transition matrix is used to model the dynamics of the maneuvering target. In [19], the TBD approach is further implemented in small UAVs and the target state is extended to the range, velocity, azimuth angle, and target magnitude. The measurement function in the algorithm represents the target intensity and ambiguity in the range-Doppler-azimuth radar cube. As a result, the estimation of target states and the probability of target presence are obtained.

The most mentioned above literature utilizes the TBD for weak target detection, and several attempts have been done for drone detection. However, most of the work deals with infrared image measurement when the measurement model represents the power and intensity of the pixel. Such measurement model provides limited state information, and there is no verification whether the detected target is a drone or not.

For more recent works in [20] and [21], a coherent radar TBD algorithm is proposed using an electromagnetic scattering model of the drone as the measurement model. The state vector includes not only the range, velocity and angles of the target but a more complex drone model, which includes the reflectivities of the drone body and rotor, as well as the rotor rotation frequency. The last parameters are estimated with maximum likelihood estimation and the detection results also achieve the discrimination of the drone from the noise. However, some assumptions and simplifications are made in the work - the number of rotors in the measurement model is known, all rotors have the same rotation frequencies, and the initial angles of the propellers are not considered.

Table 2.1 summarizes radar-based drone detection approaches and corresponding advantages and disadvantages. For the literature using the CFAR related energy detector, while having good performance with a high SNR target, they all have difficulty detecting the weak target, which can be a common situation for drones and will suffer from either a high false alarm rate or miss detection rate with CFAR and there is no verification of the detected objects whether it is a drone or not. For machine learning-based detection methods, with the drone features extracted in the frequency domain, it is able to implement the binary classification, whether the drone is present or not from the measurement. However, the ML-based detection requires additional work to localize the drone upon a classification of presence to obtain its state, and there is a lack of the extensibility analysis of the ML models to deal with different types of drones, as well as drones under different SNR. The more recent particle filter TBD approach is capable of detecting and tracking the weak target while estimating its state. However, such a method is

2

Type of detector	Approach	Pros and Cons
Energy-based detector	Compare the energy of the signal to a threshold to detect target against clutter and background noise	1. Simple and efficient to implement 2. Good performance when the target has a high SNR 3. Sensitive to statistics of the background 4. Difficult to detect weak targets 5. No verification of the detected objects
Machine learning-based detector	Use the machine learning model trained with features extracted from the measurement to perform the binary classification of presence and absence of the target.	1. Classification results can provide both detection and verification of the target 2. Demand high quality and quantity of the data and heavy labeling 3. Lack of analysis to the extensibility of the environment and target variety
Particle filter track-before-detect	A Bayesian approach which implement tracking and detection with target dynamic and measurement model.	1. Able to detect weak target with low SNR 2. Joint detection and tracking with target state estimation 3. Computational expensive 4. Require accurate dynamic and measurement model

Table 2.1: Comparison of detection techniques for drones sensing [6]

computationally expensive and requires an accurate dynamic and measurement model to have good tracking and estimation results. There is very little work in the literature that specifically exploits the electromagnetic scattering model of the drone in the TBD algorithm.

2.2. DRONE CHARACTERISTICS ESTIMATION

Characteristics of the drone are important information and features for the classification and identification of drones. These characteristics include drone size, drone RCS, the number of rotors, rotation frequencies, the number of blades per rotor, blade length, and payload. The following works provide the presented in literature estimation approaches that can be generally divided into 3 categories.

Spectrogram and transformed domain-based estimations

The work by [22] estimates the number of blades of the helicopter with tomographic imaging techniques. The inverse radon transform (IRT) is used to transform the blade rotation pattern in the time-frequency domain to the Radon Transform domain and obtain the geometry configuration of the propeller. One limitation of the approach is that it requires comparable radar pulse repetition frequency (PRF) to the rotation frequency of the propeller to capture the rotation track of the blade, or the geometry information will be lost.

In [23], a W-band Doppler radar is used to estimate the rotation frequency and blade

length of the drone by analyzing the characteristics in the time-frequency domain. The algorithm estimates the rotation frequencies by analyzing the number of peaks in the micro-Doppler spectrogram and estimates the blade length by finding the edge of the spectrum envelope. An average estimation error of 1.3 % is achieved for rotation frequency and 1.7 % for blade length. However, the measurement used for validation was taken in the chamber room with a short distance and high SNR as well as requires a very high PRF to capture the flash lines of the rotating blades.

In [24], the author extracts the rotation frequency information from the cepstrogram data. The algorithm calculates the cepstrogram by implementing the inverse Fourier transform to the short-time Fourier transform (STFT) spectrogram, which is previously used in speech analysis. For drone measurement, Cepstrogram is able to estimate the rotation frequencies from the rotors. Although the work provides the observation that multiple rotation frequencies from rotors can be discriminated from simulation data, the cepstrogram gives a less distinct pattern of multiple rotors with real measurement and no method is proposed to estimate the exact number of rotation frequencies and rotors.

The paper [25] further improves the rotation frequency estimation of the drone and proposes a multiple frequency detector. The algorithm analyzes the Helicopter Rotor Modulation (HERM) lines of the micro-Doppler spectrogram and implements multiple frequency detection by applying cross-correlation to the HERM lines and chooses the strongest 5 cross-correlation peak. The results show good performance estimating the strongest fundamental rotation component, but require a long observation time (more than 10 seconds) to achieve a reasonable frequency resolution and suffer from miss detection of secondary rotation frequencies.

Machine learning-based estimation

In [26], a classification problem of a 6-rotor drone (DJI Inspire 1) and an 8-rotor drone (HobbyLord F820) was addressed with convolutional neural network (CNN). The ML model learns from the combined micro-Doppler spectrogram (MDS) and cadence velocity diagram (CVD) which include the drone rotor rotation patterns and characteristics. The method is validated with measurements of two hovering drones using a K-band FMCW radar, achieving the classification accuracy up to 94.7%.

From the article [27], other Cespstrogram features in addition to MDS and CVD were used to classify small and medium drones, achieving 96% classification accuracy. Although the work showed the possibility of estimating the blade length and number of rotors from Cepstrogram, more specific methods and performance analysis is still desired.

In [27], the author trained a multilayer perceptron artificial neural network with synthetic drone data in both the time domain and the frequency domain to classify the number of rotors (1 or 4 rotors) and blades (2 or 3 blades), then used the networks in regression mode to estimate the rotation frequencies and blade length. Although a high classification and estimation accuracy is obtained, results (99% for SNR above 10 dB) are lacking and the algorithm is not validated with real measurements.

Model-based estimation

The model-based drone characteristics estimation is a less analyzed field and di-

2

rection. With more drone model-based particle filter TBD approaches being applied in [20][21].The tracking and estimation results are able to provide a more detailed state of drone characteristics. For instance, the range, and velocity of the drone are estimated with the posterior probability distribution of the state constructed by particles, and the rotation frequency and the reflectivity are estimated with maximum likelihood estimation using the simplified electromagnetic scattering model of the drone. However, the currently proposed methods simplify the synchronization of the rotors, assuming that all rotors have initial start angles of 0 and have very close rotation frequencies. As a result, the state would only estimate the rotation frequency of one of the multiple rotors.

2.3. CONCLUSION

In this chapter, the literature on radar-based drone detection and characteristics estimation has been discussed. Based on the review of the existing work, the challenges and limitations of the field are summarized as follows:

- In the detection and localization phase, due to the small size of drones and low RCS, most of the detection approaches using CFAR have the problem of having a high miss-detection rate or a high false alarm rate with low SNR measurements. Although the particle filter TBD provides a solution for the detection and tracking of weak targets, very little work cooperates and utilizes the electromagnetic scattering model of the drone in the TBD algorithms to estimate more characteristics of the drone.

- In the drone characteristics estimation phase, the proposed ML related methods are trained with characteristics and patterns of specific types of drone, having the problem of extensibility for unseen drone models and SNR. Spectrogram- and transform-based approaches require a long integration time to have enough frequency resolution and SNR gain for the analysis. However, this can be a problem without tracking the drone due to the range migration caused by its high maneuverability.

- It is not yet proposed a number of rotor estimations in the literature. Only a few papers provide some observation of multiple rotation frequencies from the HERM lines and Cepstrogram, but beyond such observation, there is no method proposed for this estimation problem.

Based on these gaps and challenges in the literature, this MSc thesis work will improve and solve them in terms of:

- Implement a novel model-based particle filter TBD and utilize the electromagnetic scattering model of the drones to track and estimate the extended drone state that includes the range, velocity, magnitudes of both body and rotor, rotation frequency, and the existence of the drone.

- Develop a novel model-based estimation method for the number of rotors and corresponding multiple rotation frequencies. This is implemented with a fusion of both model-based and spectrogram-based approaches for drone characteristics estimation with the help of tracking results from TBD.

3

ELECTROMAGNETIC MODELS AND MICRO-DOPPLER PATTERN OF DRONES

This chapter presents the development of the drone's electromagnetic scattering model and an analysis of how the drone's parameters would influence its micro-Doppler patterns. Specifically, Section 3.1 introduces the radar signal and the Doppler effect. Section 3.2 introduces the modeling of the drone's blade, propeller, and body. Section 3.3 provides the observation and analysis of the model. Finally, a brief conclusion is given in Section 3.4.

3.1. RADAR SIGNAL AND DOPPLER EFFECT

Radar sensors actively transmit electromagnetic waves and perform detection, ranging, and recognition with the backscattered signal from the objects. Coherent radars capture the information using the phase and frequency of the signal and compare it with a stable oscillator or reference signal source [28]. The backscattered signal of a moving target has the important characteristic that there is a shift in the transmitted frequency when the target has a relative movement to the wave source, which is called the Doppler effect [29]. In radar application, if the target is moving towards the static radar, there is a positive shift in the carrier frequency and this change in frequency, the Doppler frequency f_d, can be expressed in Equation 3.1

$$f_d = -2v/\lambda \tag{3.1}$$

where λ is the wavelength of the target and v is the target velocity. However, in many cases, the target of interest is not a rigid object and can rotate or vibrate during movement. Such motions would introduce additional modulation and sidebands around the main Doppler, which is called the micro-Doppler effect. The micro-Doppler effect includes rich information about the target. For example, a moving drone could provide a

main Doppler shift from the movement of the drone body and a micro-Doppler shift from its rotating propellers. The micro-Doppler signatures could indicate mechanic properties such as the rotation rate, the direction of rotation, and the blade length of the propeller which can be further used to distinguish the target from birds or vehicles.

3.2. SIGNAL MODEL OF THE DRONE

A typical commercial drone consists of three main components: propellers, body frame, and load, which is usually a camera. Depending on the number of rotors, they can be further broken down into helicopter (1 rotor), tricopter (3 rotors), quadcopter (4 rotors), hexacopter (6 rotors), and octocopter (8 rotors) - shown in Figure 3.1. For each propeller, different models could have a various number of blades from 2 to 4, and the length of the blades (provides different levels of lift forces). The electromagnetic scattering model of the drone has to be built on the basis of these components.

Figure 3.1: Different types of drones (a) tricopter, (b) quadcopter, (c) hexacopter, and (d) octocopter

3.2.1. MODELLING OF THE ROTATING BLADE AS A THIN WIRE

Every propeller consists of a few blades that are equally spaced in angle and rotate around the center of the propeller, which is the same as the rotor position. Such rotation is generating the observed with the coherent radar micro-Doppler signatures. These signatures in the relation to the propeller's geometry and dynamic parameters can be described and simulated using the following model of electromagnetic scattered signals.

Figure 3.2 gives the radar configuration setup and the simplified model of a two-blade propeller. The radar is located in the center and the distance between the rotation center of the propeller O and the radar is R_0. The signal of a rotating blade can be represented by two thin wires and is modeled by first looking at a scattering point P on the blade with a distance l_p to the center. The time-varying angle of the blade $\phi_{(t)}$ can be expressed as:

$$\theta(t) = \theta_0 + \Omega t \tag{3.2}$$

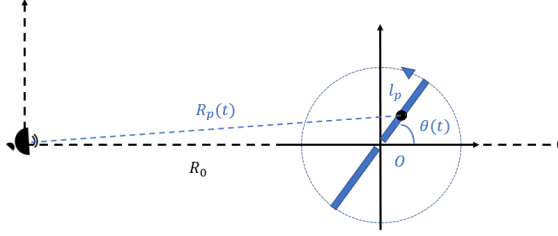where θ_0 is the initial angle of the blade and Ω is the rotation velocity. The distance $R_p(t)$

Figure 3.2: Simplified model of single propeller

from the radar center to P can be expressed as [30]:

$$R_P(t) = \left[R_0^2 + l^2 + 2lR_0 \sin(\theta_0 + \Omega t) \right]^{1/2}$$
$$\approx R_0 + vt + lsin(\theta_0 + \Omega t) \tag{3.3}$$

where v is the radial moving velocity of the drone body. With obtained range function $R_p(t)$, the backscattered signal from the point P is given by:

$$s_p(t) \propto \exp\left\{ j \left[2\pi f_c t + \frac{4\pi}{\lambda} R_P(t) \right] \right\}$$
$$= \exp\left\{ j \left[2\pi f_c t + \frac{4\pi}{\lambda} (R_0 + vt + lsin(\Omega t + \theta_0)) \right] \right\} \tag{3.4}$$
$$= \exp(j(2\pi f_c t + \frac{4\pi R_0}{\lambda})) \cdot \exp(j\frac{4\pi}{\lambda} vt) \cdot \exp(j\frac{4\pi}{\lambda} lsin(\Omega t + \theta_0))$$

where the first exponential part is related to the carrier frequency and the distance of the drone to the radar, the second part is the Doppler contribution from the movement of the body, and the third part is the micro-Doppler signals from the rotating point. In order to analytically analyze the signal model, a closed-form expression of the signal in Equation 3.4 is desired. For a fast rotating object, its rotation period can be comparable to the radar observation interval. Therefore, the Bessel functions are used to replace $sin(\theta_0 + \Omega t)$ and the equation is given [31]:

$$s_p(t) \propto \exp(j(2\pi f_c t + \frac{4\pi R_0}{\lambda})) \cdot \exp(j\frac{4\pi}{\lambda} vt)$$
$$\times \sum_{m=-\infty}^{\infty} J_m(j\frac{4\pi}{\lambda} l) \exp(jm(\Omega t + \theta_0)) \tag{3.5}$$

where J_m are the Bessel functions of the mth order. The last component of this equation describes the signal as the superposition of the harmonics of the rotation frequency Ω with the previous term as the amplitude modulation.

Then, we can come to the whole echo signal from the wire by taking the integration

with respect to the length of the wire L [21]:

$$s_W(t) \propto \exp(j(2\pi f_c t + \frac{4\pi R_0}{\lambda})) \exp(j\frac{4\pi}{\lambda}vt)$$

$$\times \sum_{m=-\infty}^{\infty} \exp(jm(\Omega t + \theta_0)) \int_{l=0}^{L} J_m(j\frac{4\pi}{\lambda}l) dl$$

$$\propto \exp(j\frac{4\pi R_0}{\lambda}) \exp(j\frac{4\pi}{\lambda}vt)$$

$$\sum_{m=-\infty}^{\infty} \exp(jm(\Omega t + \theta_0)) \times \frac{2(-1)^m \lambda}{4\pi} \sum_{m'=0}^{+\infty} J_{m+2m'+1}\left(\frac{4\pi}{\lambda}L\right)$$

(3.6)

3.2.2. MODELLING OF BLADES AND PROPELLERS

In the previous section, the backscattered signal of a rotating wire s_W is acquired. However, real blades have more complex shapes and edges, making their RCS and backscattering characteristics at different angles more complicated than a thin wire. Figure 3.3 (a) shows the geometry of the DJI 2170 propeller which consists of 2 long edges and 2 short edges with different angles related to the rotation center. To reproduce more accurately the scattering of propeller's edges, a multiwire model that uses multiple thin wires to represent the geometry of the blade was proposed in [32] and [31].

Figure 3.3 (b) shows the geometry configuration of the model of multiple wires. 4 wires are used to model the two-blade propeller oriented at $-75°$, $-10°$, $0°$, and $53°$ with a corresponding wire length equal to the real edges sizes of the DJI 2170 propeller. They model the geometry of the main edges, 2 long edges, and 2 short edges of the blade. Therefore, the model of the whole blade can be written as:

$$s_B = \sum_{w=1}^{I} s_w(w, t)$$

$$= \sum_{w=1}^{I} \exp(j\frac{4\pi R_0}{\lambda}) \exp(j\frac{4\pi}{\lambda}vt)$$

(3.7)

$$\sum_{m=-\infty}^{\infty} \exp(jm(\Omega t + \theta_0 + \theta_w)) \times \frac{2(-1)^m \lambda}{4\pi} \sum_{m'=0}^{+\infty} J_{m+2m'+1}\left(\frac{4\pi}{\lambda}L_w\right)$$

where I is the number of wires in the model, for example, $\theta_\mathbf{w} = \begin{bmatrix} -75° & -10° & 0° & 53° \end{bmatrix}$ and $\mathbf{L_w} = \begin{bmatrix} 0.2L & 0.95L & L & 0.1L \end{bmatrix}$.

(a)   (b)

Figure 3.3: (a) Blade of DJI 2170 propeller (b) Multi-wire model of propeller blade

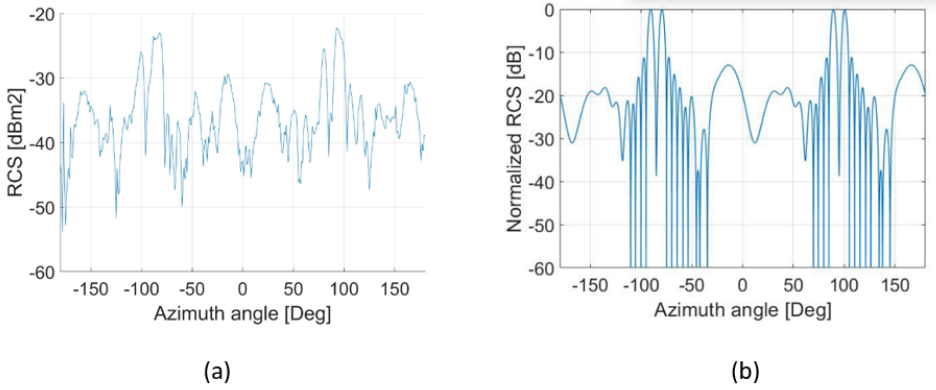(a)   (b)

Figure 3.4: (a) Measured RCS of DJI 2170 at DUCAT chamber (b) Simulated RCS of DJI 2170 from multi-wire model [32]

In [32], the RCS of the DJI 2170 propeller is measured in Delft University chamber for antenna tests (DUCAT) in the S-band (3 GHz). The measurement is given in Figure 3.4. It can be observed that the highest RCS appearing around $90°$ and $-90°$ are introduced by the longer two edges, where the blade is perpendicular to radar line-of-sight (LOS) reaching the largest backscattered cross-section. Another two peaks occur at $30°$ and $160°$ at the positions where the backscattered signals interfere constructively. Figure (b) provides the RCS of simulated blade model with Equation 3.7. It can be observed that the strong peaks of RCS at $90°$, $-90°$, $30°$ and $160°$ are successfully reproduced by multi-wire configuration and thus give better modeling of the backscattered electromagnetic characteristics of the blade.

3.2.3. MODELLING OF DRONE BODY AND GEOMETRY

The full signal model of the drone consists of the echo signal from both propellers and the body. Unlike propellers which contain multiple rotations in a short observation time, the drone body has fewer rotations and a change of RCS in such an observation interval. Therefore, the body is modeled as the point target given as:

$$s_{Body} \propto \exp(j\frac{4\pi R_0}{\lambda})exp(-j\frac{4\pi}{\lambda}vt) \tag{3.8}$$

For a radar system working at S-band and having a wavelength around 9 cm, commercial drones, for instance, DJI M200 having arm length of 32 cm, are the extended targets with multiple scattering spots. The echo signals from multiple propellers and the body are interfering at the radar receiver. Therefore, instead of using a point-target model and assuming that all propellers are located at the body center, the geometry design of the drone has to be considered.

Figure 3.5 shows the geometry configuration of the radar and a 4-rotor drone. The radar is located at O, the origin of the radar coordinate system UOV, and the drone is located at point O', at the distance R_0 from the radar. For the analysis of the drone geometry, the target local coordinate $xO'y$, which follows the translation and rotation of
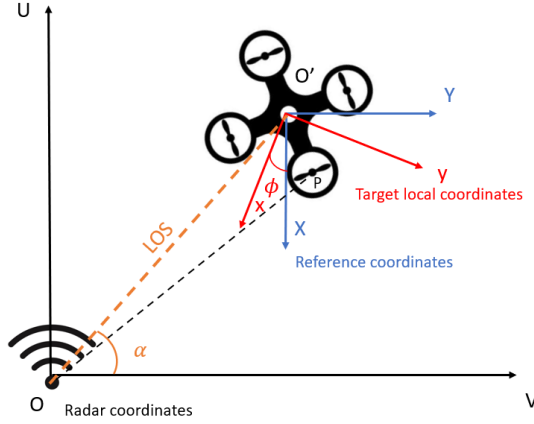
Figure 3.5: Geometry configuration of a 4-rotor drone and radar

the drone, and the reference coordinate, which only follows the translation of the drone, are introduced. α in the figure is the observation angle from radar LOS to coordinate V, and ϕ is the yaw angle of the drone. Based on such a geometry, the distance r_p from the radar to p_{th} propeller can be expressed as:

$$r_p = \sqrt{R_0^2 + d^2 - 2dR_0 cos\Delta\theta},$$
$$\Delta\theta = \frac{\pi}{N} + \pi - \alpha - \frac{\pi}{2} - mod(\phi, \frac{2\pi}{N}),$$

(3.9)

where d is the arm length of the drone and $\Delta\theta$ is the angle from radar LOS to p^{th} propeller, N is the number of propellers.

With different distances from each propeller to the radar, the full signal model of the drone is given as:

$$s_{Drone}(t) = s_{Body}(t) + \sum_{p=1}^{N} s_P(t)$$
$$= \alpha_0 \cdot e^{(j\frac{4\pi R_0}{\lambda})} \cdot e^{(-j\frac{4\pi}{\lambda}vt)}$$
$$+ \sum_{p=1}^{N} \alpha_p \cdot \exp(j\frac{4\pi R_p}{\lambda}) \cdot \exp(j\frac{4\pi}{\lambda}vt)$$
$$\times \sum_{m=-\infty}^{\infty} \exp(jm(\Omega t + \theta_0 + \theta_w)) \cdot \frac{2(-1)^m\lambda}{4\pi} \sum_{m'=0}^{+\infty} J_{m+2m'+1}\left(\frac{4\pi}{\lambda}L_w\right)$$

(3.10)

Simulation variables	Values
Carrier frequency	3.315 GHz
Pulse repetition interval	240 μs
Bandwidth	50 MHz
Propeller number	4
Blade length	0.216 m
Arm length	0.322 m
Rotation frequency	60 Hz

Table 3.1: Simulation parameters of radar and drone

3.3. DOPPLER SPECTRUM AND MICRO-DOPPLER PATTERNS OF THE SCATTERED SIGNALS

3.3.1. DOPPLER SPECTRUM OF PROPOSED SIGNAL MODEL

With the proposed signal model given in Equation 3.10, drone simulation data can be generated with selected parameters given in Table 3.1. The radar is working in the S-band (3.315 GHz) with 240 μs pulse repetition interval (PRI) and 50 MHz bandwidths, providing a range resolution equal to 3 meters. The parameters of the drone are selected to simulate those from DJI M200 which is a 4-rotor drone with 0.216 m blade length and 0.322 m arm length.

Figure 3.6 shows the generated micro-Doppler signal C_n in time domain. A duration of 0.0614 seconds consisting of 256 pulses is selected as a coherent processing interval (CPI) for observation, where in this duration the characteristics of the drone such as range, velocity, and rotation frequency are assumed to be constant. Figure 3.6(a) gives the backscattered signal from one propeller, and 7 equally spaced peaks can be observed. This is defined by the rotation frequency equal to 60 Hz when there are 3.7 full rotations in one observation interval and it corresponds to 7.4 peaks at the moments when the propellers are perpendicular to the radar's line of sight. Figure 3.6(b) illustrates a case of more realistic simulation of signals C_n that considers 4 propellers with random initial angles and the geometry of the drones.

Then, a fast Fourier transform (FFT) is applied to C_n to observe the characteristics of the rotating blades in the frequency domain and the results are given in Figure 3.7. Figure 3.7 (a) illustrates the spectrum of the DJI M200 drone real measurement with the PARSAX S-band polarimetric FMCW Doppler radar in TU Delft. Fig. 3.7(b) shows the traditional simplified drone model using single thin wire for the modeling of the blade and assuming all propellers are located at the body center, and Fig. 3.7(c) presents the spectrum for the proposed multiwire model with geometry information of both blade and multiple propellers considered. In the spectrum, the highest peak located at 0 Hz is the reflection of the drone body which is hovering and thus has a Doppler component with zero velocity. The harmonics around the central frequency are introduced by the rotation of the propellers and are related to both construction and kinematic characteristics such as the length of the blade, synchronization status of multiple propellers, their
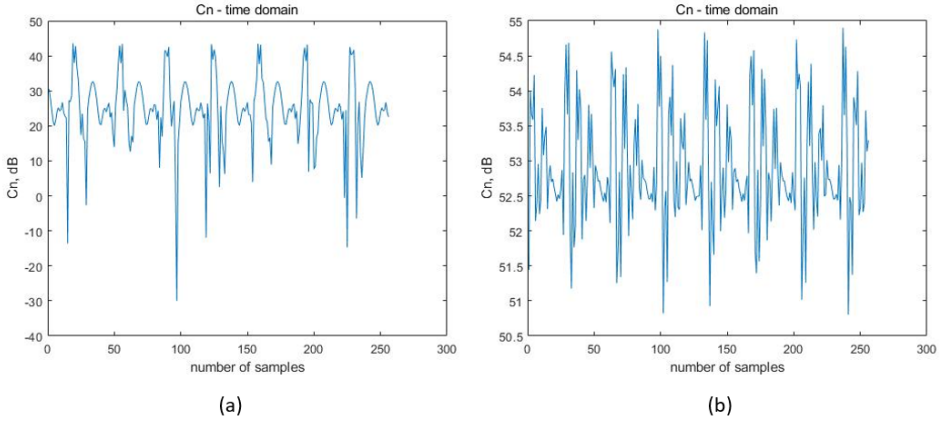
3

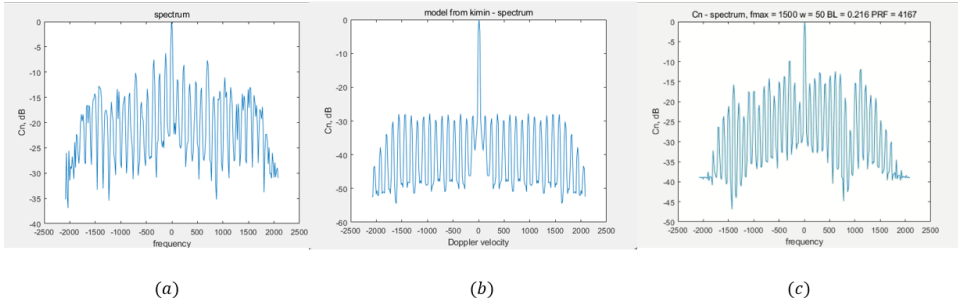Figure 3.6: (a) micro-Doppler signal from 1 rotor (b) micro-Doppler signal from 4 rotors

Figure 3.7: Comparison of micro-Doppler spectrum from (a) measurement from DJI M200 (b) signal model from [33] (c) multi-wire model with geometry information

rotation frequencies, and drone geometry. From the comparison, it can be observed that the proposed model has a better representation of the real data in terms of the shape of the harmonics, the central Doppler-to-the-harmonics ratio, and the dynamic range of the harmonics and noise floor than the traditional simplified model.

For the observation and analysis of the extended electromagnetic model of the drone, the micro-Doppler spectrogram which applies STFT to the C_n is able to reveal the Fourier spectrum of the signal while maintaining the time information. Such micro-Doppler signatures are able to provide additional features and information to help the analysis of drone characteristics. Figure 3.8 gives the micro-Doppler spectrogram with different durations of the processing window. For a short window duration (the observation time is much shorter than one propeller rotation cycle), it is capable of capturing and revealing the flashes of the blade shown in Figure 3.8 (a). The flash lines provide the track of the rotating blades, and it is possible to estimate the rotation frequency by measuring the interval between two flash lines. For a long window duration (the observation time contains one full or multiple propeller rotation cycles), the flash lines are no longer vis-
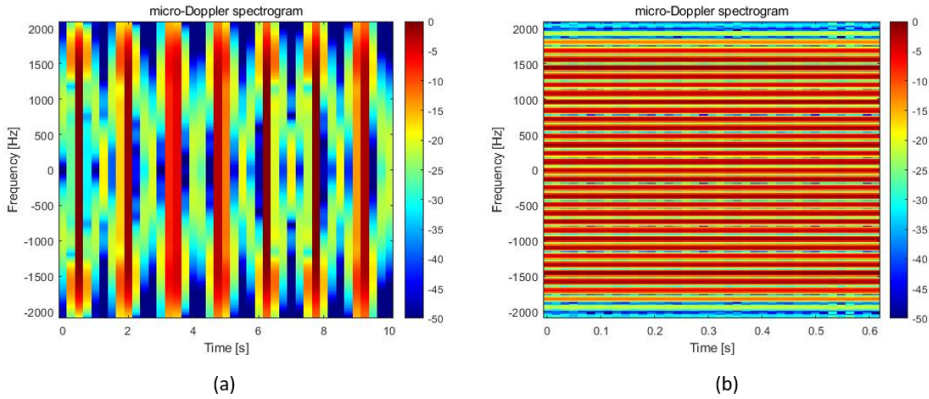
Figure 3.8: Micro-Doppler spectrogram with the window size (a) 16 (b) 128 time samples

ible, and instead, the HERM spectral lines are presented. The HERM lines are separated and periodic on the Doppler axis with a spacing interval related to the rotation frequency and the number of blades per propeller.

3.3.2. Observation and analysis of the influence of drone parameters on the micro-Doppler pattern

From the signal model given in Equation 3.10, the extended model takes into account the presence of scattered signals from different rotors, different initial angles of the propellers, as well as the geometry of the drone. This increased complexity makes the model more realistic, and the micro-Doppler signatures are directly influenced by these parameters. Therefore, an analysis is implemented to investigate how these parameters would affect the micro-Doppler patterns.

For controlling of variables and better observation of the influence of each parameter. The analysis is first given to the independent rotors and then the complete drone model is analyzed. The results of the analysis are given as follows:

Influence of rotor geometry

Figure 3.9 gives the results of the micro-Doppler pattern as a function of the distance between 2 rotors. The vertical axis shows the distance between two rotors expressed in terms of $\Delta R/\lambda$, where ΔR is the range difference. The horizontal axis is the frequency axis of the spectrum and the color bar provides the information on the dependancy of the signal power in dB. Each row in this plot represents the envelope of the spectrum harmonics of the micro-Doppler pattern of the scattered signal for the corresponding distance difference between 2 rotors. This envelope of the spectrum harmonics is plotted in the figure to provide better visualization of the pattern's shape and changes (spectral harmonics themself are quite narrow and not very well visible on such a plot). It can be seen that the maximum power of the micro-Doppler signal is obtained at the top and bottom of the figure, where the range difference is 4λ and 4.5λ, while the minimum power is observed when the range difference is 4.25λ. Such results are due to the coher-
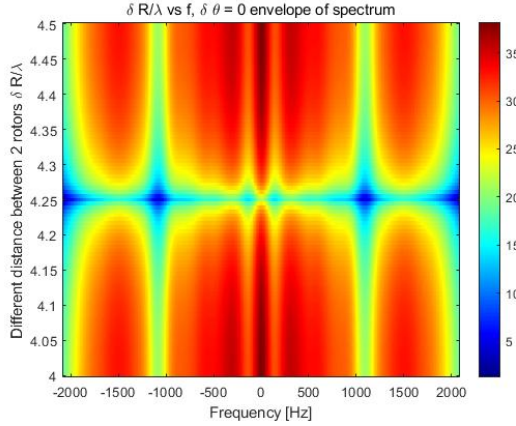
Figure 3.9: The envelop of the Micro-Doppler pattern as a function of the distance between 2 rotors

ent summation of a target's signal harmonics. For example, the RCS of 2 identical point scatter separated by a distance d will be observed by the radar as:

$$
\sigma_r = \left| \sum_{n=1}^{2} \sqrt{\sigma_n} e^{j\frac{4\pi}{\lambda}R_n} \right|^2
$$
$$
= 2\left[1 + \cos\left(\frac{4\pi d}{\lambda}\sin\theta\right)\right] \in [0, 4\sigma_n]
$$

(3.11)

Therefore, when the distance d is integer multiples of λ, the signals are summed in phase and thus have the highest amplitude. And when the distance d is integer multiples of $\lambda/4$, they will sum unconstructively and cancel with each other.

Influence of rotor synchronization

Figure 3.10 illustrates the changes in micro-Doppler patterns as a function of the difference in the blades' initial orientation angle between two rotors that are separated by the distance of 7λ. There are two symmetries that can be observed from this figure, one oriented along the zero Doppler velocity, and the second one oriented along the 90-degree difference between the orientation angles of the two propellers. The first symmetry is related to the velocity and orientation angle of the drone body, - as from Equation 3.10, the exponential part $e^{-j\frac{4\pi}{\lambda}vt}$ would be a frequency shift in the frequency domain moving the center of the spectrum to the Doppler shift of the drone body, and for the case of zero yaw angle or azimuth angle, the signals from 2 rotors would have exactly the same distance to the radar and would have in-phase summation for all the frequency components. The second symmetry relates to the middle position of the 2 blade propeller within the rotation period. Therefore, the micro-Doppler harmonics would have symmetric patterns due to the characteristics of the blade RCS and the coherent superposition of the signal of two rotors.
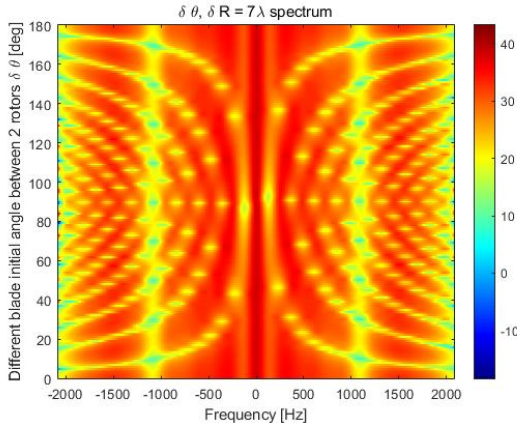
Figure 3.10: Micro-Doppler pattern as a function of the difference between initial angles of 2 rotors blades'

Influence of drone orientation

After analysis of the influence on micro-Doppler patterns from the drone geometry and rotors synchronization, it is also possible to check the influence of the drone's geometry orientation relatively to the radar line of sight of the observed micro-Doppler pattern. More observations are implemented from DJI M200 simulation data with parameters shown in Table 3.1 for the analysis of more complicated and realistic results.

Figure 3.11 illustrates the changes of micro-Doppler patterns as a function of yaw angle. In this Figure the yaw angle of the drone changes from 0° facing the front side of the radar to 90°, giving the side profile to the radar. 4 propellers have a rotation frequency of 60 Hz but are not synchronized, having random initial orientation angles of blades $\Phi = \begin{bmatrix} 172 & 1 & 27 & 166 \end{bmatrix}$. As the distance from each propeller to the radar changes with
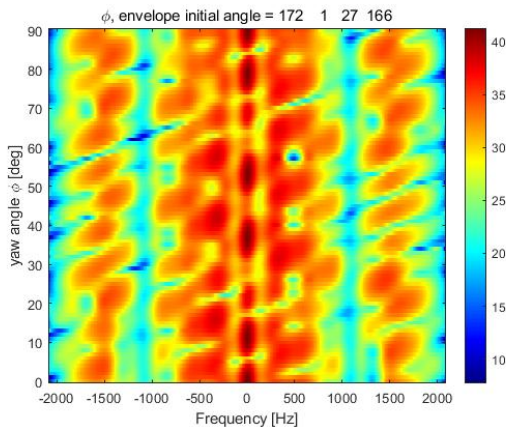

Figure 3.11: Micro-Doppler pattern as a function of yaw angles of the drone
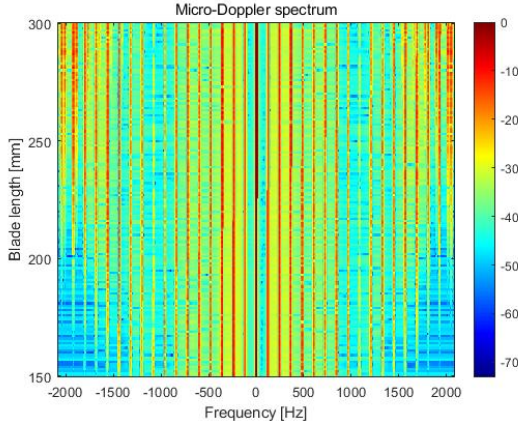
Figure 3.12: Micro-Doppler pattern as a function of blade length

the orientation of the drone, scatters could have constructive and destructive interferences during the change of yaw angle. For the simulated 4-rotor drone which has the arms spaced by 90°, a symmetrical and period pattern during the change of 90° in yaw angle can be observed from the results. At certain angles such as 0°, 12° and 37°, the strongest constructive interferences are obtained while at angles of 5°, 18° and 45°, most of the echo signals are out of phase and canceled with each other. Such results give the orientation-dependent harmonics strength and patterns, which could be possibly further used for the estimation of drone orientation.

Influence of drone blade length

Figure 3.12 indicates the change in micro-Doppler patterns as a function of the blade length. In order to reveal a clear influence of the blade length, each column now directly represents the harmonics from the spectrum instead of taking the envelope. It is shown that with increasing the blade length, the bandwidth of the spectrum is also increasing, and for the blade length above 25 cm, aliasing and folding appear in the harmonics. This is defined by the simulated case with $PRI = 240\mu s$, $PRF = 4167Hz$ and a maximum unambiguous Doppler frequency equals to 2083.5 Hz. For a rotating propeller the maximum linear velocity is:

$$v = L \times \omega \tag{3.12}$$

where ω is the circular rotation frequency and the maximum linear velocity of the propeller is the tip of the blade with L equal to the length of the blade. As result, according to the Doppler effect, the maximum Doppler frequency at the blade tip is given as:

$$f_{max} = \frac{2\omega L}{\lambda} \tag{3.13}$$

Taking the rotation frequency of 60 Hz and the maximum unambiguous frequency into equation 3.13, the maximum blade length for the measurement without spectrum aliasing is equal to 25 cm.
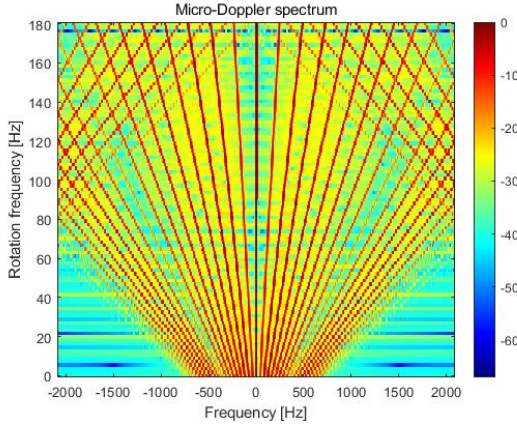
Figure 3.13: Micro-Doppler pattern as a function of propeller's rotation frequency

Influence of the propeller rotation frequency

Figure 3.13 illustrates the change in micro-Doppler patterns as a function of rotation frequency. With the increase in rotation frequency, the bandwidth of the spectrum also increases. As given in Equation 3.12, increasing the rotation frequency ω would also increase the maximum linear velocity of the propeller. Therefore, with a blade length of 21.6 cm, the maximum rotation frequency for unambiguous measurement is 69.4 Hz. However, compared to the change of micro-Doppler spectrum from changing of blade length, the number of strong harmonic lines is not increased. Instead, the bandwidth is extended by increasing the spacing between the harmonics. To be more specific, the spacing of the harmonics is given as:

$$f_{spacing} = f_{rotation} = \frac{1}{T_{rotation}} \qquad (3.14)$$

Therefore, with the periodicity property of the harmonics, it is possible to extract and estimate the rotation frequency of one rotor in the frequency domain. The presence of a few rotors with different rotation frequencies will make such estimation not accurate.

3.4. CONCLUSIONS

This chapter introduces the micro-Doppler effect in radar sensing and develops the improved electromagnetic model of the drone, with RCS properties of the blade and geometry of the propellers considered.

The extended model uses the multi-wire configuration to simulate the characteristics of angle-dependent RCS of the blade and considers the coherent superposition of scattered signals from different propellers based on the drone geometry and orientation. From the observation results, a more realistic and better representation of the drone signal is obtained in both the time and frequency domain.

Based on the simulation data, analysis is implemented to find out the influence of the drone's parameters on its micro-Doppler patterns, including the distance and syn-

chronization status between rotors, the blade length, the rotation frequency of the propellers, and the orientation angle of the drone construction relatively to the radar line of sight. The observed results and signatures provide rich features of the constructional and kinematic parameters such as blade-length-dependence of the spectrum bandwidth, rotation-frequency-dependent harmonics period, and the orientation-dependent harmonic strength. The information indicates the possibility to extract and estimate these parameters from the measured micro-Doppler signals.

In the rest of the research work, the focus is on the analysis of multiple number of rotors and every rotor could have separate rotation frequencies and initial angle. Therefore, we decide to concentrate on these most important parameters and set the orientation angle of the drone and arm length to 0 for simplification.

4

JOINT PIPELINE FOR DRONE DETECTION AND CHARACTERISTICS ESTIMATION

4.1. PIPELINE OVERVIEW

In the previous chapter, the electromagnetic scattering model of the drone is presented and analyzed, showing that the shapes of the micro-Doppler patterns of the backscattered signal depend on the constructional and kinematic characteristics of the drone. This section presents an overview of the chain of processing procedures and algorithms that take radar measurement as input and implement drone detection and tracking while estimating its characteristics.

The overview of the proposed pipeline is given in Figure 4.1. The processing starts with the slow time sequence of range profiles. Then a TBD algorithm with particle filtering is implemented to perform joint detection and tracking of the drone while estimating
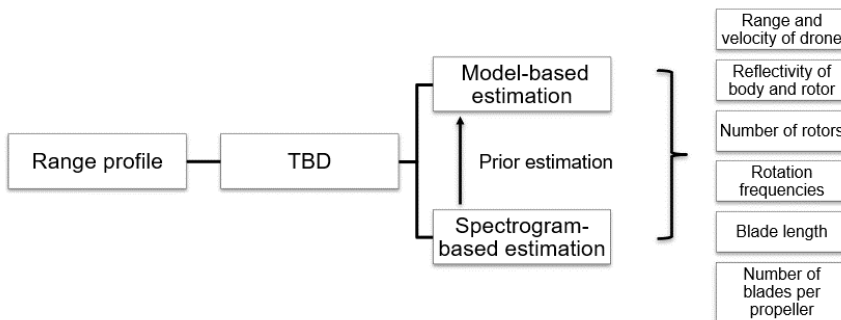

Figure 4.1: Block diagram of the detection and estimation pipeline

27

the range, velocity, rotation frequency, and reflectivity of the drone body and propellers. From the output of the TBD block, a detection decision is made based on the likelihood-ratio test (LRT). If a drone is detected, both model-based and spectrogram-based estimation algorithms will be implemented to further estimate more characteristics of the drone. The detailed descriptions of the modules are as follows:

1. **Generation of range profiles:** The processing pipeline takes the range time matrix as input and will estimate both the range and the velocity of the object in the TBD algorithms. This requires the use of a coherent radar, such as a pulse Doppler radar or FMCW for sensing and measurement. For the synthetic signals simulation, the range profile is directly simulated by mapping the range to the time delay of the received signal as the output of the matched filtering. For the experimental data, the PARSAX radar provides the raw radar data, which are samples of received chirps. They are reshaped into a fast-time slow-time radar matrix, and a FFT is applied to the fast-time data to make the range compression - to extract the beat frequency, which is directly connected to the target range.

2. **TBD:** The TBD module is a model-based detection and estimation algorithm. It takes multiple range-time radar matrix CPI as input and performs tracking and estimation with particle filtering. The output of the module is the estimated range, velocity, and reflectivity and the detection decision of LRT with estimated parameters. The following model-based estimation and spectrogram-based estimation modules will only be implemented when there is a positive detection result.

3. **Model-based estimation:** The model-based estimation is implemented in the time domain. It takes the estimated range, velocity, and reflectivity from the TBD module and the rotation frequency estimation from the spectrogram-based estimation module as a priori information. The module will provide the estimated number of rotors, the angles and rotation frequencies of each rotor as results.

4. **Spectrogram-based estimation:** This module only takes the estimated range from TBD as input and transforms the range time data into the spectrogram for frequency domain-based signature analysis. This module outputs the initial estimation of the rotation frequencies as the prior information for the model-based estimation module and can provide other constructional parameters of the drone, which are blade length and the number of blades per rotor.

4.2. SIMULATION DATA GENERATION
The proposed pipeline is first applied to and validated with the simulated model data. As the input data require a coherent radar to maintain the strict frequency and phase relations, a pulse Doppler radar is simulated with the transmitted signal given by the transmitter.

$$u(t) = Re\left\{\sum_{n=0}^{N-1} \tilde{u}(t - nT)e^{-j2\pi f_c t}\right\} \tag{4.1}$$

where N is the number of pulses, T is the PRI, f_c is the carrier frequency of the signal. To simulate the drone measurements using the PARSAX radar, the PRI for simulated signals
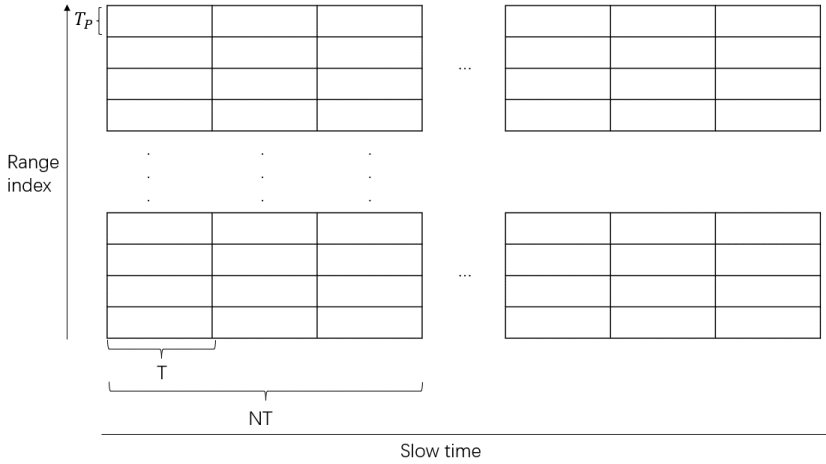
Figure 4.2: The structure of the simulated and acquired radar data

set to 240 us, the bandwidth B_w - to 50 MHz, providing 3-meter range resolution, and the carrier frequency f_c - to the value of 3.315 GHz.

Figure 4.2 shows the structure of simulated and acquired radar data. After matched filtering and sampled in the time period T_P, the raw data are reshaped into a fast-time and slow-time matrix, where the fast-time denotes the range index which is 3 meters each range bin according to $\Delta R = c/2B$ and in the slow-time axis, every N intervals are assumed to be a coherent processing interval (CPI). It is also assumed that during one CPI the location, velocity, reflectivity and other parameters of the drone do not change (there is no range migration).

For the received signal, matched filtering (MF) is performed firstly to find the time delay of the received signal compared to the transmitted signal and thus find the target range. In the simulation, the MF output is simplified and presented by the Dirac delta function denoting the peak position of the MF output where the target exists. Since only the single channel is simulated, the detected state of the object is denoted as $X \equiv [r, v]^T$ where r is the distance from the object to the radar and v is the radial velocity of the object. The drone has modulated complex reflections $\boldsymbol{\alpha} = [\alpha_0, \alpha_1]$ where α_0 represents the reflectivity of the main body and α_1 is the reflectivity related to the rotating characteristics including the superposition of the rotors and the rotating frequency w. Then the modulated received signal is given by

$$
\begin{aligned}
z(t) &= z_{Drone}(t)\Lambda(t - \tau(X) - nT) \\
&= \alpha_0 e^{-j\frac{4\pi r}{\lambda}} e^{-j\frac{4\pi}{\lambda}vt} \Lambda(t - \tau(X) - nT) \\
&\quad + \alpha_P \sum_{p=1}^{N} e^{-j\frac{4\pi r}{\lambda}} e^{-j\frac{4\pi}{\lambda}vt} C_n(\omega)\Lambda(t - \tau(X) - nT) \\
&\quad + \epsilon(t)
\end{aligned}
\tag{4.2}
$$

where $\epsilon(t)$ is the white Gaussian complex noise and $\tau(X) = 2r/c$, $\Lambda(t)$ is the MF output of the signal

$$\Lambda(t) = \tilde{u}(t) * \tilde{u}(-t) = \int_0^{T_p} \tilde{u}(t')\tilde{u}(t' - t)\,dt', \tag{4.3}$$

and $C_n(\omega)$ is the micro-Doppler signal given in Equation 3.7.

$$C_n(w) = \sum_{W=1}^{I} \sum_{m=-\infty}^{\infty} e^{jm(\Omega t+\theta_0+\theta_W)} \times \frac{2(-1)^m \lambda}{4\pi} \sum_{m'=0}^{+\infty} J_{m+2m'+1}\left(\frac{4\pi}{\lambda} L_W\right) \tag{4.4}$$

In the simulation we used a case where a 4-rotor drone with 21.6 cm blade length, 32.2 cm arm length starts at 250 meters away from the radar and is approaching the radar with a radial velocity of 20 m/s. 4 rotors have randomly generated rotation frequency with the interval of 50 to 60 Hz and random initial angle of every propeller's orientation. Figure 4.3 provides the multi-domain representations of different characteristics. In Fig. 4.3(a), one CPI of micro-Doppler signal C_n is observed, where the 40 dB floor defined by the the strong reflection from the drone body and the fluctuations originate from the rotating blades. Due to random initial angle of propellers and different
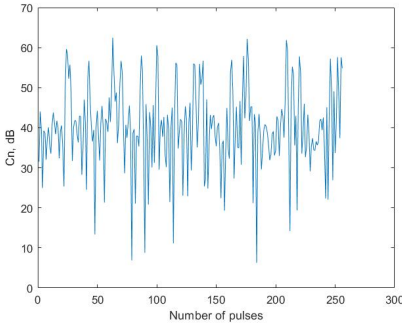
(a) Micro-Doppler signal C_n
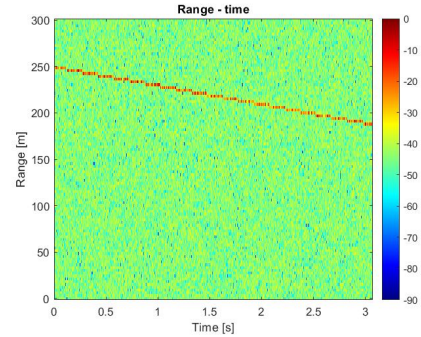
(b) Range-time map
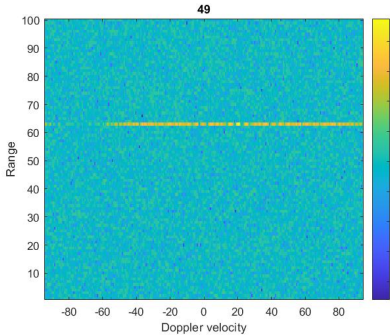
(c) Range-Doppler map
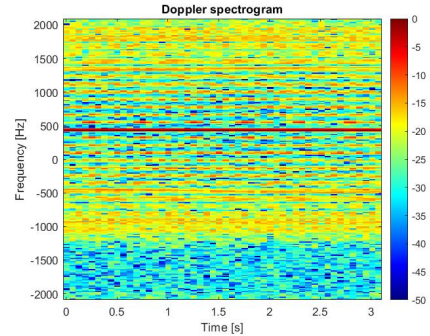
(d) Micro-Doppler spectrogram

Figure 4.3: Simulated drone measurement represented in different domains

rotation frequencies of 4 rotors, the time-domain signal is more complex than the simplified case given in the Figure 3.8. In Fig. 4.3(b), the trajectory of the drone is shown, which is moving linearly to the radar. However, due to 3-meter range resolution, the drone stays in one range cell of 3 meters until it migrates to the next one. In Fig. 4.3(c), a range-Doppler map is shown by implementing an FFT along the slow-time dimension. It illustrates both range and velocity information about the drone in range-Doppler frequency domain. The strongest response in this figure gives the extended in velocity line of the drone response that is centered around drone body velocity of 20 m/s and has extended side bands of harmonics that introduced by the micro-Doppler modulation from the rotating propellers. In Fig. 4.3(d), a STFT with a window duration of 0.0614 s is applied to the signal C_n and the micro-Doppler spectrogram of the drone is obtained. As the time window width includes multiple rotation cycles of the blade, the HERM lines are observed, and the period of these lines could provide information of rotation frequencies. The width of such observed spectrum could be related to the length of the blades.

4.3. TRACK-BEFORE-DETECT WITH PARTICLE FILTERING

In this section, we describe the implementation of the TBD algorithm. Compared to traditional detect-before-track approach, which implement a hard decision of detection and threshold based on current measurement, the TBD is implemented to the raw measurement data with joint tracking and detection. Due to the tracking of the target with multiple measurements, the target presence is determined based on integrated and kinematically correlated energy [17] and thus a higher SNR can be achieved. Therefore, the algorithm outperforms the classical energy-based methods for detecting targets with low SNR. If the detection result is true, the algorithm will also provide the estimated state variables of the drone including the range, velocity, magnitudes of signals scattered from the drone body and rotors, and rotation frequency of the rotor as the prior information for the following spectrogram-based and model-based drone characteristics estimation.

4.3.1. INTRODUCTION OF PARTICLE FILTER

Sequential Monte Carlo (SMC) method as known as particle filter is a technique that use a Bayesian recursive filter to approximate the optimal state in the estimation problem. The key idea of the particle filter (PF) is that the posterior density function of the state can be represented by a set of samples with weights, and the estimation results can thus be calculated using these samples.

In more details it can be expressed as follows. For N particles and associated weights $\{x_{k-1}^i, w_{k-1}^i\}_{i=1}^{N}$ at time step $k-1$, the posterior density $p(x_{k-1}|Z_{1:k-1})$ is approximated as:

$$p(x_{k-1}|Z_{1:k-1}) \approx \sum_{i=1}^{N} w_{k-1}^i \delta(x_{k-1} - x_{k-1}^i) \tag{4.5}$$

where $\delta(.)$ is the Dirac function. Then at the next time step k, a new measurement Z_k is received, and we want to update the posterior to $p(x_k|Z_{1:k})$. This can be done by first predicting the new particle state with an importance sampling function:

$$x_k^i \sim q(x_k|x_{k-1}^i, Z_{1:k}) \tag{4.6}$$

and the importance weights are updated with equation:

$$w_k^i \propto w_{k-1}^i \times \frac{p\left(\mathbf{z}_k \mid \mathbf{x}_k^i\right) p\left(\mathbf{x}_k^i \mid \mathbf{x}_{k-1}^i\right)}{q\left(\mathbf{x}_k^i \mid \mathbf{x}_{k-1}^i, \mathbf{Z}_{1:k}\right)} \tag{4.7}$$

where $p\left(\mathbf{z}_k \mid \mathbf{x}_k^i\right)$ is the likelihood, $p\left(\mathbf{x}_k^i \mid \mathbf{x}_{k-1}^i\right)$ is the prior and $q\left(\mathbf{x}_k^i \mid \mathbf{x}_{k-1}^i, \mathbf{Z}_{1:k}\right)$ is the importance density. With the update $\{x_k^i, w_k^i\}_{i=1}^N$, it is possible to calculate the estimate of the target state. For instance, the minimum mean square error estimation of the state can be written as:

$$\hat{x}_{kMMSE}(Z) = E\{x_k | Z_{1:k}\} = \int x_k p(x_k | Z_{1:k}) dZ_{1:k} \approx \sum_{i=1}^N w_k^i x_k^i \tag{4.8}$$

During the recursive updates, a degeneracy problem would occur, as the variance of the importance weights would keep increasing, leading to very few particles having very high weights, while the contributions of other particles are almost negligible. To solve this degeneracy problem, the resampling step is implemented to remove particles of low weight and duplicate particles of high weight [34][35]. In this way, the particles are re-sampled around the area of the target state with high likelihood, which means that the particles after re-sample are closer to the true values of the state.

4.3.2. Dynamic and measurement models of the drone
For this model-based PF-TBD algorithm, the transition of the drone state and measurement are according to the model:

$$\begin{aligned} s_{k+1} &= f(s_k, v_k) \\ z_{k+1} &= h(s_k, n_k) \end{aligned} \tag{4.9}$$

where f and h are the corresponding dynamic model and sensor measurement model, v_k is the process noise, n_k is random noise in the sensor and drone state s_k is defined as

$$s_k = \begin{bmatrix} r_k \ v_k \ \alpha_{body} \ \alpha_{rotor} \ w_k \ E_k \end{bmatrix}^T \tag{4.10}$$

where r, v are the range and radial velocity of the drone, α_{body} and α_{rotor} are the reflectivity of the drone body and the rotor, w is the rotation frequency of the rotor, and E is the discrete variable representing the existence of the drone.

Dynamic model
For the dynamic model of the first five characteristics of drones, they are assumed to be constant within one short CPI of 0.06 seconds and thus a nearly constant velocity, reflectivity, and rotation frequency model is used, and the dynamic model F is given as:

$$F = \begin{bmatrix} 1 & T & 0 & 0 & 0 \\ 0 & 1 & 0 & 0 & 0 \\ 0 & 0 & 1 & 0 & 0 \\ 0 & 0 & 0 & 1 & 0 \\ 0 & 0 & 0 & 0 & 1 \end{bmatrix} \tag{4.11}$$

and the process noise v_k is the zero mean white Gaussian noise (WGN) with the covariance matrix Q given as:

$$Q = \begin{bmatrix} \frac{\sigma_v}{3} T^3 & \frac{\sigma_v}{2} T^2 & 0 & 0 & 0 \\ \frac{\sigma_v}{2} T^2 & \sigma_v T & 0 & 0 & 0 \\ 0 & 0 & \sigma_{\alpha_b} T & 0 & 0 \\ 0 & 0 & 0 & \sigma_{\alpha_r} T & 0 \\ 0 & 0 & 0 & 0 & \sigma_{w_r} T \end{bmatrix} \tag{4.12}$$

where σ_v, σ_{α_b}, σ_{α_r}, σ_{w_r} are the standard deviation of the drone velocity, reflectivity and rotation frequency, denoting the process noise level. With modeled process noise, although a nearly constant value model is used for the state dynamics, acceleration in velocity, change in range and rotation frequency, and fluctuations in reflectivity can be accommodated.

The drone existence state E_k is a binary variable, $E_k \in 1, 0$, where 1 denotes that the drone is present and 0 denotes that the drone is absent. The change between 2 states is described by the Markov chain and has the transition matrix given by:

$$\Pi = \begin{bmatrix} 1 - P_b & P_b \\ P_d & 1 - P_d \end{bmatrix} \tag{4.13}$$

where P_b is the probability of birth, denoting the state transits from 0 to 1 and P_d is the probability of death, denoting the state transits from 1 to 0.

Measurement model

Equation 4.2 gives the continuous-time model of the received radar sensor signal, after sampling at period T_P, each pulse interval is sampled in discrete time with Γ samples. Then in one CPI, which consists of N pulses, the signal is represented by

$$\mathbf{z}[\gamma] \triangleq \mathbf{z}(\gamma T_P), \gamma = 1, ..., \Gamma \times N \tag{4.14}$$

and the radar matrix can be represented in matrix form

$$\begin{aligned} \tilde{\mathbf{Z}}(r) &\triangleq [\mathbf{z}[r], \mathbf{z}[\Gamma + r], \cdots, \mathbf{z}[(N-1)\Gamma + r]] \\ &= (\mathbf{t}(X, \omega)\boldsymbol{\alpha})^T \Lambda \left(r T_p - \tau(X) \right) \\ &\quad + \boldsymbol{n}(r) \end{aligned} \tag{4.15}$$

$$\boldsymbol{n}(r) \triangleq [\, \epsilon\left(r T_p\right), \boldsymbol{\epsilon}\left(r T_p + T\right), ..., \boldsymbol{\epsilon}\left(r T_p + (N-1) T\right)]^T$$

where the term t is the temporal steering matrix and denotes the main Doppler caused by the body of the drone and the micro-Doppler induced by rotating components.

$$\mathbf{t}(X, \omega) \triangleq e^{-j \frac{4\pi r}{\lambda}} \begin{bmatrix} 1 & C_0(\omega) \\ \vdots & \vdots \\ e^{j \frac{4\pi v}{\lambda}(N-1)T} & C_{N-1}(\omega) e^{j \frac{4\pi v}{\lambda}(N-1)T} \end{bmatrix} \tag{4.16}$$

Then, depending on whether the target is presented or not, $z(r)$ can be given.

$$\mathbf{z}(r) = \begin{cases} \mathbf{H}(r, X, \omega)\boldsymbol{\alpha} + \mathbf{n}(r) & , E_k = 1 \\ \mathbf{n}(r) & , E_k = 0 \end{cases} \tag{4.17}$$

where the measurement model $\mathbf{H}(r, X, \omega)$ is $\mathbf{t}(X, \omega)\Lambda\left(r\, T_p - \tau(X)\right)$. The binary state E_k represents 2 hypotheses of the existence of the drone. $E_k = 1$ denotes the target is presented in the range bin r and $E_k = 0$ denotes the target is absent and thus there is only background noise. The likelihood functions based on two hypotheses can then be formulated as follows.

$$l\left(\mathbf{Z}_k(r) \mid X_k, \boldsymbol{\alpha}_k, \omega, E_k = 1\right) = \mathscr{CN}\left(\mathbf{Z}_k(r); \mathbf{H}\left(r, X_k, \omega\right)\boldsymbol{\alpha}_k, \Sigma\right) \tag{4.18}$$

$$l\left(\mathbf{Z}_k(r) \mid X_k, \boldsymbol{\alpha}_k, \omega, E_k = 0\right) = \mathscr{CN}\left(\mathbf{Z}_k(r); 0, \Sigma\right) \tag{4.19}$$

In this work, both likelihood functions have a circularly symmetric complex Gaussian random distribution and Σ is the covariance matrix. For the detection of the drone, the likelihood ratio can be formulated as

$$L\left(\mathbf{Z}_{1:K} \mid \hat{X}_{1:K}, \hat{\boldsymbol{\alpha}}_{1:K}, \hat{\omega}\right) \triangleq \frac{l\left(\mathbf{Z}_{1:K} \mid \hat{X}_{1:K}, \hat{\boldsymbol{\alpha}}_{1:K}, \hat{\omega}; E_k = 1\right)}{l\left(\mathbf{Z}_{1:K} \mid E_K = 0\right)}, \tag{4.20}$$

For a LRT problem, the detection decision between E_1 and E_0 can be made based on a desired threshold Γ_K shown as the equation:

$$L\left(\mathbf{Z}_{1:K} \mid \hat{X}_{1:K}, \hat{\boldsymbol{\alpha}}_{1:K}, \hat{\omega}\right) \underset{E_0}{\overset{E_1}{\gtrless}} \mathscr{T}_K \tag{4.21}$$

However, in the TBD algorithm, the detection will be determined with the posterior probability of the target existence constructed by the particles which will be introduced in the following sections.

4.3.3. A PARTICLE FILTER FOR TRACK-BEFORE-DETECT

Then, a PF for TBD algorithm is implemented to detect the presence of the drone and estimate its dynamic state. The pseudocode of TBD is given in the algorithm 1. With defined target and measurement models, the TBD with particle filter algorithm is initialized with the following settings:

- **Dynamic model and measurement model** - a nearly constant value model is used, given by equation 4.11 and the electromagnetic scattering model of the drone is used as the measurement model given by equation 4.16.

- **Process noise and random noise** - the process noise is the WGN with covariance matrix given in equation 4.12 and the level of the process noise is defined with a priori information from empirical observation of drone flight. The random noise of the measurement is also modeled as WGN with the variance estimated from the measurements of the background (clutter or noise).

- **Initialization of particles** - the particle state of the drone at time step 0 is initialized and has a uniform distribution within its normal operating range; the transition probability of the drone existence state is assumed to be known, and an initial existence probability is used to generate E_0. The weights of the particles are initialized uniformly, as $1/N$ where N is the number of particles.

With the initialized particles $\{s_0^i, w_0^i\}_{i=1}^N$, we would like to utilize the coming measurement and information from multiple CPIs to recursively detect, track the location, and estimate the drone state given in equation 4.10 with the posterior density function constructed by a set of weighted samples described in Section 4.3.1. This is implemented with the prediction and the update steps that applied to the particles and weights as follows:

Prediction step

Firstly, the existence states are drawn based on the transition matrix given by:

$$\left\{E_k^i\right\}_{n=1}^N = RT(\left\{E_{k-1}^i\right\}_{n=1}^N, \Pi) \tag{4.22}$$

where RT is the regime transition function and its algorithm is given in the Appendix A.2. Due to the value of the existence state E, the prediction of the particles can be classified into 2 categories:

- **Newborn particles.** For newborn particles which have a state change from 0 to 1, these types of particles will be initialized having the uniform distribution of the drone dynamic state within its normal operational range as described in the previous initialization step at time step 0.

- **Existed particles.** For the existed particles which remain in the state $E_k = 1$ from previous time step, the new particles state will be drawn from the equation 4.6. For the importance sampling function, it is chosen as the transitional prior given by:

$$p(x_k|x_{k-1}^i) = \mathcal{N}(x_k; f(x_{k-1}^i, Q_{k-1})) \tag{4.23}$$

where f is the dynamic model and Q is the covariance matrix described in equation 4.11 and 4.12.

Update step

With the predicted particles s_k^i, the importance weights are drawn based on LRT given by:

$$
\begin{aligned}
l(z_k|s_k^i) &= \frac{p(z_k|s_k^i, E_k = 1)}{p(z_k|E_k = 0)} \\
&= \frac{e^{-\frac{1}{2}\left\{(z_k - h(x_k^i))^H \Sigma^{-1}(z_k - h(x_k^i))\right\}}}{e^{-\frac{1}{2}\left\{z_k^H \Sigma^{-1} z_k\right\}}}
\end{aligned}
\tag{4.24}
$$

For WGN in the measurement where $\Sigma = \sigma^2 I$, the equation can be further simplified as follows.

$$
\begin{aligned}
l(z_k|s_k^i) &= e^{-\frac{1}{2\sigma_n^2 I}\left\{(z_k - h(x_k^i))^H(z_k - h(x_k^i)) - z^H z\right\}} \\
&= e^{-\frac{1}{2\sigma_n^2 I}\left\{h(x_k^i)^H h(x_k^i) - z_k^H h(x_k^i) - h(x_k^i)^H z_k\right\}}
\end{aligned}
\tag{4.25}
$$

By substituting the importance sampling function in equation 4.6 into the weights update equation 4.7, the new importance weights can be drawn as:

$$w_k^i \propto w_{k-1}^i l(z_k | x_k^i) \tag{4.26}$$

In the application of the proposed TBD algorithm, the sequential importance resampling (SIR) particle filter is used because of its advantages in calculating the importance weights and sampling the importance function. SIR filter deal with particle degeneracy problem by implementing resampling in iteration, and the resampled weights always have the uniform distribution. Therefore, the importance weights are calculated and normalized by:

$$\tilde{w}_k^i = l(z_k | x_k^i)$$
$$w_k^i = \frac{\tilde{w}_k^i}{\sum_{i=1}^N \tilde{w}_k^i} \tag{4.27}$$

Then the resampling algorithm is implemented to remove the particles with low weights by mapping them to the particles with higher likelihood. Recursively updated particles can be obtained by:

$$\left\{s_k^i\right\}_{i=1}^N = RESAMPLE[\left\{s_k^i, w_k^i\right\}_{i=1}^N] \tag{4.28}$$

and the posterior density function of the target existence and the estimation of drone dynamics can be obtained by:

$$\hat{P}_k = \frac{\sum_{n=1}^N E_k^n}{N}$$
$$\hat{x}_k = \frac{\sum_{n=1}^N x_k^n E_k^n}{\sum_{n=1}^N E_k^n} \tag{4.29}$$

The detection decision can then be made if the existence probability is higher than a desired threshold.

4.4. MODEL-BASED DRONE CHARACTERISTICS ESTIMATION

In this section, the model-based drone characteristics estimation algorithm based on spectrograms is introduced in the processing pipeline of the proposed estimation algorithm given in Figure 4.4.
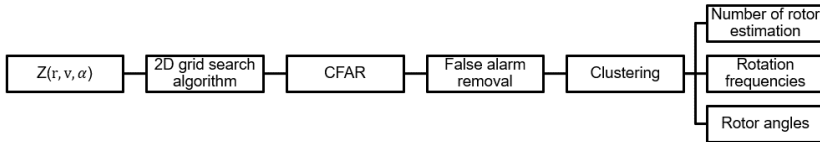

Figure 4.4: Pipeline of model-based estimation algorithm

Algorithm 1 Particle Filter for Track-Before-Detect

Input: F, $h(.), Q, \sigma_n, \{x_0^i, w_0^i\}_{i=1}^N$ ▷ Parameter initialization
Input: $Z_{1:K}$ ▷ Measurement from K CPIs
for $k = 1 : K$ **do**
    $\{E_k^i\}_{n=1}^N = RT(\{E_{k-1}^i\}_{n=1}^N, \Pi)$ ▷ Prediction of existence state
    for $n = 1 : N$ **do**   ▷ Prediction of particles
       if $E_k^n = 1$ and $E_{k-1}^n = 0$ **then**   ▷ Newborn particles
          Initialize x_k^i
       end if
       if $E_k^n = 1$ and $E_{k-1}^n = 1$ **then**   ▷ Existed particles
          $x_k^n = p(x_k | x_{k-1}^n, z_K)$
       end if

       if $E_k^n = 1$ **then**
          $\bar{w}_k^i = l(z_k | s_k^i)$ ▷ Calculate importance weights
       else if $E_k^n = 0$ **then**
          $\bar{w}_k^i = 1$
       end if
    end for
    Normalize importance weights
    Resampling with the algorithm in the Appendix A.1
    $s_k^n = RESAMPLE[\{s_k^i, w_k^i\}_{i=1}^N]$
end for
Return s_k^n

4

For an overview of the processing, the algorithm takes the output of the estimated range, velocity, and reflectivity from TBD algorithm as inputs and uses the likelihood function given in Equation 4.25 as the system model. Then, a two-dimensional grid search is implemented by going through possible values of rotation frequencies and angles to optimize the model and find the best combination of parameters for each rotor. As each rotor could have a specific combination of the blade angle and rotation frequency, the output of the grid search results would have multiple strongest responses, and the number of them is related to the number of rotors. To obtain the final estimation, a CFAR detector is applied to find the strongest detected responses and then a false alarm removal algorithm is used to remove the wrong detections from noise and harmonics. Finally, the number of rotors is found by clustering the adjacent strong response points that originate from one rotor. With detected clusters (rotors), the associated angles and rotation frequencies can be obtained automatically. The details of each processing step are given in the following subsections.

4.4.1. SIGNAL MODEL AND GRID SEARCH ALGORITHM

In the TBD algorithm, a simplified model is used that does not consider the number of rotors and the initial angles of their propellers. It means the assumption of unknown type of drone and is aimed at avoiding high-dimensional particle filtering and reducing the computational load. Then, after obtaining the detection decision and the estimated range, velocity and reflectivity from the TBD algorithm, the complete signal model can be analysed analyzed. It is given as:

$$\mathbf{z}(r) = \mathbf{H}(r, \omega, M, \phi)\boldsymbol{\alpha} + \mathbf{n}(r) \tag{4.30}$$

The measurement model $\mathbf{H}$ can be written as:

$$\mathbf{H} = \begin{bmatrix} 1 & C_0(\omega_1, \phi_1) & \cdots & C_0(\omega_M, \phi_M) \\ \vdots & \vdots & \cdots & \vdots \\ e^{j\Omega(N-1)T} & C_{N-1}(\omega_1, \phi_1)e^{j\Omega(N-1)T} & \cdots & C_{N-1}(\omega_M, \phi_1)e^{j\Omega(N-1)T} \end{bmatrix} \Lambda\left(rT_p - \tau(X)\right) \tag{4.31}$$

where M is the number of rotors. The first column corresponds to the main Doppler velocity component that introduced by the drone body, while columns from 2 to $M+1$ represent the micro-Doppler modulations introduced by each rotor with the corresponding rotation frequency ω and the initial orientation angle of the blade ϕ. The fitting of the parameters is evaluated by the likelihood:

$$\begin{aligned} l\left(\mathbf{Z}(r) \mid \omega, M, \phi\right) &= \mathscr{CN}\left(\mathbf{Z}_k(r); \mathbf{H}\left(\omega, M, \phi\right)\boldsymbol{\alpha}, \Sigma\right) \\ &= \frac{1}{\pi|\boldsymbol{\Sigma}|}e^{\left((\mathbf{Z}-\mathbf{H}\boldsymbol{\alpha})^{\mathrm{T}}\boldsymbol{\Sigma}^{-1}(\mathbf{Z}-\mathbf{H}\boldsymbol{\alpha})\right)} \end{aligned} \tag{4.32}$$

To estimate the number of rotors and the corresponding rotation frequencies and initial angles, the grid search method is used. Grid search is a hyperparameter optimization method used in machine learning to tune and find an optimal set of parameters for a learning algorithm. For example, if we want to estimate a set of parameters $V = [v_1, v_2, \cdots, v_m]$ that optimize the proposed model, in the grid search, a set of lower

bounds l = $[l_1, l_2, \cdots, l_m]$ and upper bounds u = $[u_1, u_2, \cdots, u_m]$ are defined for each parameter. Then the N equally separated values will be chosen in each interval $[l_i, u_i]$ of v_i. The model will check the total number of N^m combinations of variable values and the combination with the best performance will be chosen in the evaluation function. This project borrows the idea from grid search in machine learning to estimate the parameters of the drone model by maximizing the likelihood function given in Equation 4.32.

In this drone's characteristics estimation algorithm, the parameters that need to be optimized in the model are the number of rotors, the rotation frequency of every rotor ω, and the orientation angle of every rotor's propeller at the beginning of one CPI. The boundary of the rotation frequencies can be defined as $\omega \in [0 : 160]$ Hz, which contains the possible operational rotation frequency during flight. The limit for the angle of the blade is given as $\phi \in [0 : 2\pi/B]$, where B is the number of blades per rotor, and for a two-blade rotor it is $[0 : 180]$ degrees. The possible number of rotors of a drone M can be $M = [1, 2, 3, 4, 6, 8]$. In this study, we used the grid increment of 0.1Hz for the interval of rotation frequencies, $1°$ increment for the grid of angles, and set $M = 4$. We also assume each rotor to be independent. As a result, there will be a total number of combinations of $(1601 \times 181)^4 = 7 \cdot 10^{21}$ parameters to be checked. Therefore, it is not possible to use a brute-force search to go through all combinations.

Instead, from the signal model given in equation 4.31, the measurement data is the superposition of all the rotors with the corresponding rotation frequencies and angles (ω_i, ϕ_i). Therefore, another approach is developed using the signal model given by

$$\mathbf{H}(\omega, \phi) \triangleq e^{-j\frac{4\pi\hat{r}}{\lambda}} \begin{bmatrix} 1 & C_0(\omega, \phi) \\ \vdots & \vdots \\ e^{j\frac{4\pi\hat{v}}{\lambda}(N-1)T} & C_{N-1}(\omega, \phi)e^{j\frac{4\pi\hat{v}}{\lambda}(N-1)T} \end{bmatrix} \times \begin{bmatrix} \hat{\alpha}_{body} \\ \hat{\alpha}_{rotor} \end{bmatrix} \quad (4.33)$$

where $\hat{r}, \hat{v}, \hat{\alpha}_{body}$ and $\hat{\alpha}_{rotor}$ are the estimation results of TBD given in Equation 4.29. The ω and ϕ are the variables in the proposed 2D grid search. With each combination of the variables, the likelihood measuring how likely this current parameter combination
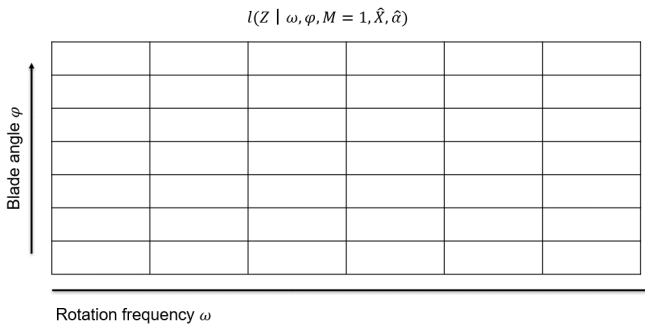

Figure 4.5: 2-dimensional grid search over rotation frequency and blade angle

under test (ω, ϕ) is from one of the rotors is calculated, given by:

$$l(z_k|\hat{x}_n, \omega, \phi) = \frac{1}{2\pi|\Sigma|} e^{-\frac{1}{2}(z_k - H(\omega,\phi))^H \Sigma^{-1}(z_k - H(\omega,\phi))} \tag{4.34}$$

The 2D grid search results are illustrated in Figure 4.5 and each grid represents the likelihood calculated with the corresponding blade angle and rotation frequency. From the results, a higher likelihood response would be observed when the combination of (ω_i, ϕ_i) in the test matches one of the true values of $(\omega_{i=1:M}, \phi_{i=1:M})$. In this way, at least M strong responses from rotors can be observed, and by estimating the number of strong peaks from grid search output, the number of rotors and the corresponding rotation frequency and angle can be estimated.

4.4.2. NUMBER OF ROTORS ESTIMATION

With the obtained 2D grid search results, 3 processing steps are implemented to get the estimation results of the rotor numbers, which are 2D CFAR detection, false alarm removal, and clustering.

2D-CFAR

To detect the number of peaks in gird search output, a cell averaging detector 2-dimensional constant false alarm rate (2D-CFAR) is applied to the grid search results.

Figure 4.6 illustrates the window of 2D-CFAR. A 2D-CFAR window contains cell under test (CUT), training cells (TC), and guard cells (GC) that separate CUT and TC to prevent signal leakage. The method compares the energy level of CUT with the average energy of TC with a scale factor. The detection threshold T is defined as:

$$T = \alpha P_n \tag{4.35}$$

where P_n is the average noise power of the GC and the scalar α is adjusted to the desired
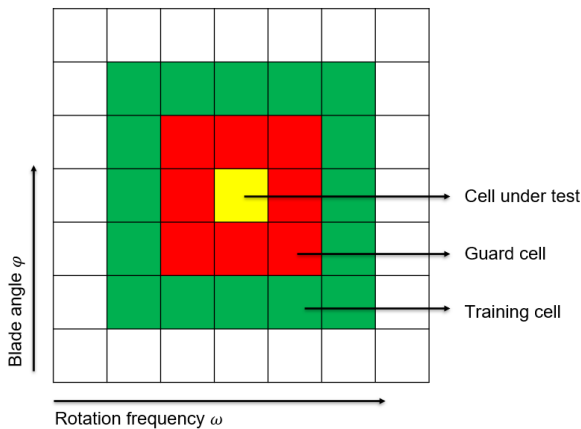

Figure 4.6: 2D CFAR window

false alarm rate given as:

$$\alpha = N\left(P_{FA}^{-1/N} - 1\right) \tag{4.36}$$

The 2D-CFAR window will slide through the pixels from the grid search output and make the detection decision. However, due to the cells used for training and guarding, the pixels at the edges and corners will not be tested, and some blind area is left.

False alarm removal

For the detection results of 2D-CFAR, false alarms that report clutter noise or harmonics of true rotation frequencies as a rotor signal could be the main challenges, which not only increase computational load during processing, but also greatly impact the accuracy of the estimation of the number of rotors. In this work, threshold-based and tracking-aided false alarm removal techniques are implemented.

- Threshold-based false alarm removal
  The first type of approach used for false alarm removal is the rotation frequency threshold. The detection outputs of 2D-CFAR are combinations of blade angles and rotation frequencies. However, not all results are introduced by the actual rotors and some results with extremely slow or extremely fast rotation frequency which are out of the drone's operational range can easily be filtered out. Therefore, 3 thresholds listed below are applied:

  – **Fixed threshold from normal operational rotation frequency range**
    From the 2D-CFAR results, there can be some detections with rotor rotation frequency far outside the normal operating range of small commercial drones, which is typically between 4,000 and 6000 revolutions per minute (RPM) [36]. Therefore, a fixed threshold of rotation frequency from 30 Hz to 100 Hz that corresponds to 1800 RPM to 6000 RPM is first applied to the detection results which define the rotation frequencies of interest under drones' normal working circumstances. This would also remove the detections from noise and harmonics with very low or very high rotation frequency.

  – **Dynamic threshold based on rotor mechanics**
    During the flight, the rotation frequencies between different rotors are within specific limits to maintain the posture and balance of the drone. For instance, when a 4-rotor drone is hovering, all 4 rotors would have very close rotation frequencies to hover still. When the drone is moving forward, its front-pair rotor would decelerate, while the back-pair rotor would accelerate to make the body of the drone lean forward, and the maximum rotation frequency difference can appear in this case. Figure 4.7 provides the flight log of the DJI M200 drone, which shows the rotation speed of four rotors in RPM. The recorded drone flew forward and back with a rotation speed difference of around 1000 RPM when flying stably. Therefore, in the detection results, the highest likelihood peak detection is considered the center rotation frequency f_{center} and the dynamic threshold is applied as $\left[f_{center} - 25, f_{center} + 25\right]$.

  – **Threshold from spectrogram-based and model-based estimation**
    In the spectrogram-based estimation, the Cepstrogram analysis is implemented,
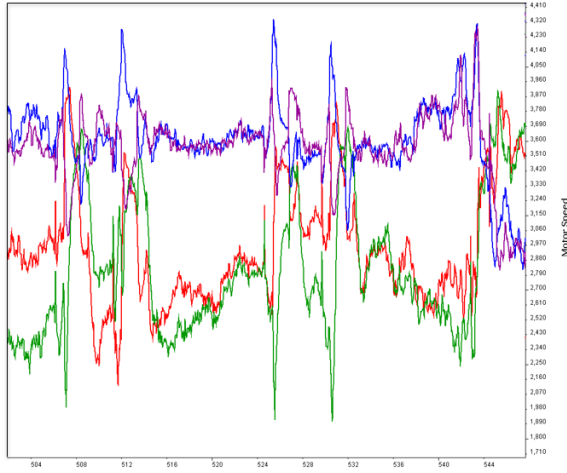
Figure 4.7: flight log of drone DJI M200

taking the inverse FFT of the STFT power spectrogram. This analysis can extract the periodicity information of the harmonic lines, which is proportional to the rotors' rotation frequency. Therefore, the third threshold is applied centered on the estimated rotation frequency of the cepstrogram f_{ceps} with an allowed error tolerance $f_{tolerance}$ and given as $[f_{ceps} - f_{tolerance}, f_{ceps} + f_{tolerance}$. In addition to spectrogram-based estimation, another rotation frequency estimation $\hat{f}_{TBD}$ is obtained from the TBD algorithm. This would usually be the strongest component of the rotation frequency of the rotors, and this would be included in the range of $[f_{ceps} - f_{tolerance}, f_{ceps} + f_{tolerance}]$ and will be used to validate the final estimation results.

- Tracking-aided false alarm removal
  The second approach used for false alarm removal is tracking-aided methods. From the output of 2D-CFAR, the current blade angle and the rotation frequency of each detection can be obtained. With the known PRI of the radar, we can predict and track the angle of the blade in the next CPI and use this information to maintain true positive detections and remove others from the noise. 2 specific tracking-aided methods are listed below:

  – **Tracking-assisted detection removal with adjacent CPI**
    Assume at i^{th} CPI, we have detection (ϕ_i, ω_i). Then, the blade angle at i+1 CPI can be predicted by:

    $$\phi_{i+1} = \phi_{i+1} + 2\pi\omega_i T \tag{4.37}$$

    where T is PRI and for 2 consecutive CPIs, the rotation frequency is assumed to be constant:

    $$\omega_{i+1} = \omega_i \tag{4.38}$$

The predicted $(\phi_{i+1}^p, \omega_{i+1}^p)$ at i+1 CPI will be compared to all the detected results at i+1 CPI $(\Phi_{i+1}^d, \Omega_{i+1}^d)$ and if the predicted results are not given in the detected results within a certain tolerance given as $(\phi_{i+1}^p, \omega_{i+1}^p) \notin (\Phi_{i+1}^d, \Omega_{i+1}^d)$, the point $(\phi_{i+1}^p, \omega_{i+1}^p)$ will be considered a false alarm and will be discarded from the detections.

– **Tracking-aided detection removal with multiple CPIs**
The tracking results with adjacent CPI would take an initial removal of the detections introduced by random noise. However, other false alarms caused by the side lobe or harmonics of the rotation frequencies could still exist. Therefore, tracking-aided detection removal with multiple CPIs is implemented. Instead of making an estimation decision with the detection results of one CPI, the detection results of K CPIs are used, which take advantage of a longer integration time to achieve a better SNR in the final estimation. For CPIs 1 to K-1, the predictions will be made recursively with Equations 4.37 and 4.38 until the predictions are made at (ϕ_K^p, ω_K^p). In this way, the detection results from each CPI from 1 to $K-1$ would be considered as initialization in the tracking and have the final prediction at the Kth CPI. All prediction results will be accumulated at K^{th} CPI and thus the final detection results would contain the integrated information from CPI 1 to K.

– **Tracking-assisted integration of rotor likelihood with multiple CPIs**
The tracking results with adjacent CPI would take an initial removal of the detections introduced by random noise. However, other false alarms caused by the side lobe or harmonics of the rotation frequencies could still exist, and miss detections of rotors could occur when there are overlaps of rotors with close rotation frequency and angles. Therefore, a tracking-aided number of rotor estimation with multiple CPIs is implemented. Instead of making an estimation decision with the detection results of one CPI, the detection results of K consecutive CPIs are used, taking advantage of a longer integration time to achieve better SNR in the final estimation. This is implemented with following steps:

⋄ Prediction
For detections $(\phi_{i-1}^d, \omega_{i-1}^d)$ after removal of false alarms, predictions of rotor positions at i^{th} CPI will be made recursively with Equations 4.37 and 4.38 and the prediction $(\phi_{i|i-1}^p, \omega_{i|i-1}^p, w_{i|i-1}^d)$ will be obtained where $w_{i|i-1}^d$ is the likelihood of the point $(\phi_{i|i-1}^p, \omega_{i|i-1}^p)$.

⋄ Update
With prediction (ϕ_i^p, ω_i^p) and detection (ϕ_i^d, ω_i^d), the Euclidean distance between 2 sets is calculated. if the distance between two points is less than a threshold ϵ, they will be assumed to originate from the same rotor

and the update will be implemented:

$$\phi_{i|i}^d = \frac{1}{w_i^d + w_{i|i-1}^p}(w_i^d \phi_i^d + w_{i|i-1}^p \phi_{i|i-1}^p)$$

$$\omega_{i|i}^d = \frac{1}{w_i^d + w_{i|i-1}^p}(w_i^d \omega_i^d + w_{i|i-1}^p \omega_{i|i-1}^p) \qquad (4.39)$$

$$w_{i|i}^d = w_{i|i-1}^p + w_i^d$$

where the predicted angle and rotation frequency are updated with weighted likelihoods and the likelihood value is integrated. Therefore, with observation and tracking of multiple CPIs, the information and likelihood of the rotor parameters are kinematically correlated and integrated making them easier to distinguish from noise and false alarms.

Clustering

Clustering is the task of assigning targets with similar properties such as distance to the same group. Therefore, it distinguishes and divides targets into clusters with the same characteristics. In the grid search output, while the combination of parameters (ϕ, ω) with exact values of the rotors would give the highest likelihood and peak in the results, combinations with close angles or rotation frequencies could also have a high likelihood due to the close modeling of the true signal patterns. Therefore, instead of identifying each strong peak as a detected rotor, clustering is first implemented to associate detection results from the same rotors. From tracking-aided false alarm removal methods, clustering is applied to the results that accumulate the detections from K CPIs. Therefore, the positions that represent the rotors' true parameter combination would have a much denser distribution than others and would have higher integrated likelihood. Therefore, based on how the clusters are formed, the density-based spatial clustering of applications with noise (DBSCAN) algorithm proposed in [37] is used for the clustering.
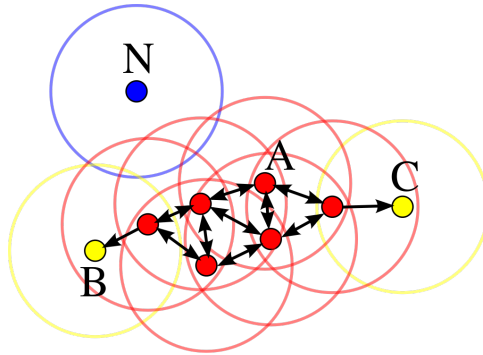

Figure 4.8: Density-based clustring by DBSCAN algorithm

Figure 4.8 illustrates how DBSCAN perform clustering. The algorithm divides the points into core points, directly reachable points, and noise points. The algorithm iterates through the points, and a point A is a core point if it has at least M neighboring points within the distance ϵ from it. A point B is directly reachable if it is connected to a core point p. One cluster is constituted by connected core points A with the edge formed by directly reachable points B. A point N is called a noise point if it cannot be reached by any other points. In this way, DBSCAN is able to form a cluster with a density that exceeds some threshold, and the shape is related to the chosen distance function.

4.5. SPECTROGRAM-BASED DRONE CHARACTERISTICS ESTIMATION

In this section, the drone characteristics estimation algorithm is introduced with the processing pipeline shown in Figure 4.9.
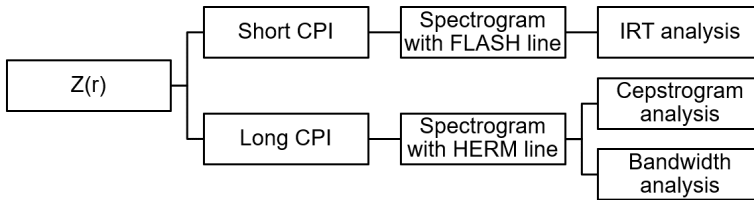

Figure 4.9: Pipeline of spectrogram-based estimation algorithm

For an overview of the processing, the pipeline takes the estimated range bin where the drone appears as the input. Then, a STFT is applied to extract the frequency information that indicates the velocity of the target while maintaining the time information. With an observation time comparable to the rotation period of the propeller, the track of the blades can be captured, and the FLASH lines can be obtained. Then IRT can be applied to find the constructional information of the propeller. With observation time much longer than the rotation period and containing several rotation cycles, the HERM lines can be observed, and based on these characteristics, cepstrogram analysis can be applied to estimate the rotation frequencies of the propellers, and bandwidth analysis of the spectrum can give the blade length estimation.

4.5.1. SHORT-TIME FOURIER TRANSFORM AND MICRO-DOPPLER SPECTROGRAM

Although the Fourier transform can extract frequency information from the signal and find the velocity of the drone, it cannot depict the change of the signal over time and lose important information for drones. Therefore, the time-frequency analysis, STFT, is applied to the range-time profile to extract the rotation frequency components of the drone over time [38]. STFT divides the signal into small windows of the same duration with overlaps and applies the Fourier transform on each window. The mathematical

representation is given as:

$$\text{STFT}\{x(t)\}(\tau,\omega) \equiv X(\tau,\omega) = \int_{-\infty}^{\infty} x(t)\,w(t-\tau)\,e^{-i\omega t}\,dt \tag{4.40}$$

where ω is the window function. However, one drawback of STFT is the fixed resolution of time-frequency and the trade-off between them. For a longer window time, a better frequency resolution can be obtained, as the frequency resolution is inversely proportional to the observation time, but the time resolution becomes worse. Based on the properties of STFT, with a short CPI that is comparable to the rotation period of the propeller, the high time resolution makes it possible to extract the flashes of the blade at the cost of a worse Doppler resolution. With a longer CPI that includes several rotation periods, the results STFT provide more detailed frequency information of the rotating components but are no longer able to depict the track of the rotating blade. Figure 3.8 illustrates the different characteristics and features that can be represented in the spectrogram with flash lines and HERM lines, respectively. Then, further spectrogram-based analysis is implemented to extract and estimate the constructional and kinematic parameters hidden behind them.

4.5.2. Transform-based drone characteristics estimation approaches

IRT-based number of blades per rotor analysis

Radon transform (RT) is a domain transformation approach that projects an image matrix in a given direction. The RT is defined by:

$$\begin{aligned}
R(p,\tau)[f(x,y)] &= \int_{-\infty}^{\infty} f(x,\tau+px)dx \\
&= \int_{-\infty}^{\infty}\int_{-\infty}^{\infty} f(x,y)\delta[y-(\tau+px)]dy dx \\
&\equiv U(p,\tau),
\end{aligned} \tag{4.41}$$

where p is the slope of the line and τ is the intercept, and IRT which can be used to reconstruct the image is given as:

$$f(x,y) = \frac{1}{2\pi}\int_{-\infty}^{\infty} \frac{d}{dy} H[U(p,y-px)]dp \tag{4.42}$$

where H is the Hilbert transform. In [39], the author analyzed the application of the RT and IRT with a sinusoidal modulated signal. A point in the (x,y) domain will be transformed into a sinusoidal pattern in the RT domain, and, inversely, a sinusoidal pattern can be transformed back into a point with proper projection angles.

Figure 4.10 illustrates the sinusoidal signals and the corresponding IRT results. Figures 4.10a and 4.10b give an example of a sinusoidal pattern with 2 periods in the observation duration of 1 second, and the pattern in the result IRT is focused at 2 Hz, providing an energy-centered point. Figures 4.10c and 4.10d provide the results for two sinusoidal signals with the same frequency but with a phase difference of 90° and 2 points are observed with a frequency at 2 Hz.

(a) Single sinusoidal signal

(b) IRT results of single sinusoidal signal

(c) Combination of 2 sinusoidal signals
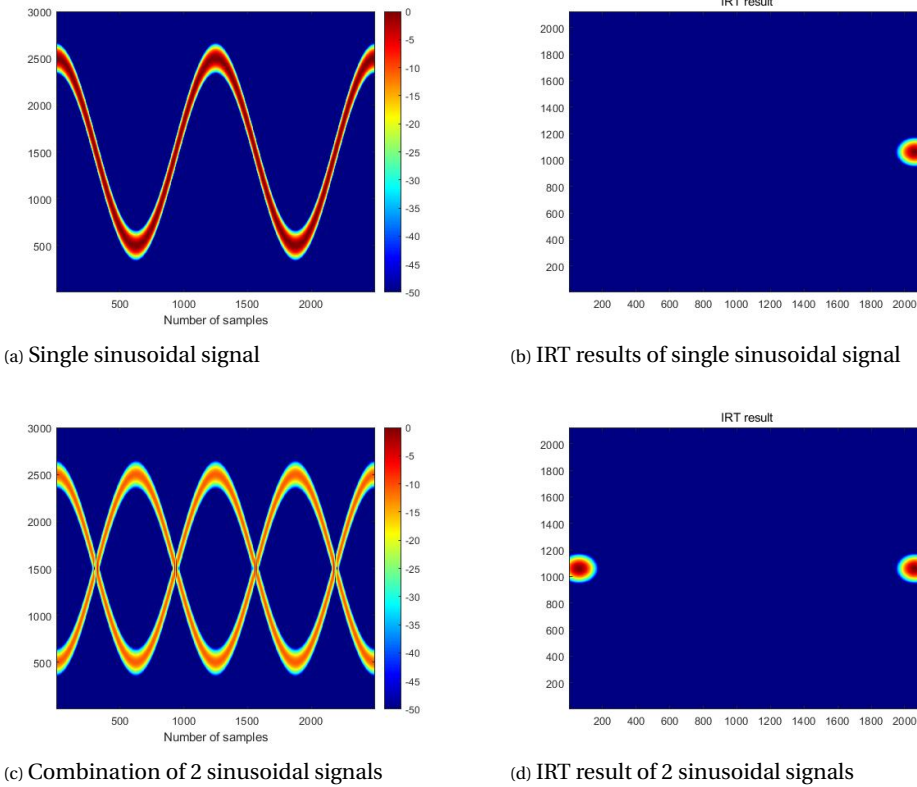

(d) IRT result of 2 sinusoidal signals

Figure 4.10: IRT results of sinusoidal signals

For the application of IRT in drone characteristics estimation, with short integration interval, the flash lines of the rotor which capture the tracks of the rotating blades can be obtained and observed as sinusoidal patterns. Therefore, with proper projection angles that related to the rotation frequency of the rotor, the tomographic structure of the rotor consisting specific number of blades can be reconstructed with IRT. From the output of the IRT analysis, the estimation of the number of blades per rotor $\hat{B}$ would be obtained.

Spectrum-based blade length analysis

In section 3.3.2, the change of drone's micro-Doppler patterns as a function of blade length is discussed. The rotation of the blade will introduce micro-Doppler signatures modulated around the main Doppler caused by the drone body. With the increase of the blade length, the bandwidth of the micro-Doppler signatures also increases because the maximum rotation frequency component is contributed by the tip of the blade where the maximum linear velocity is achieved. The mathematical expression of the maximum

Doppler frequency f_{max} as a function of the blade length L is written as:

$$f_{max} = \frac{2\Omega L}{\lambda}$$

$$\Omega = 2\pi f_{rot}$$

(4.43)

where Ω is the angular rotation velocity and f_{rot} is the rotation frequency that can be estimated from the Cepstrogram analysis. Therefore, from the spectrum, the frequency components contributed by the drone are a frequency band from $f_D - f_{max}$ to $f_D + f_{max}$.

In [40], the frequency $f_D + f_{max}$ is found by taking the derivative of the spectrum envelope and finding the minima of the derivative of the envelope that correspond to the fastest drop in the envelope. However, due to the limited PRF and observation time, this negative peak position is sensitive to fluctuations in the spectrum envelope and the resolution of the spectrum. Therefore, instead of finding the peak position in the derivative, the zero position is used that corresponds to the location at the edge of the pass band where the envelope starts to drop. Therefore, the upper cut-off frequency $f_D + f_{max}$ of the pass band is defined and estimated.

Cepstrogram-based rotation frequency analysis

In [41], the author first proposed the definition of Cepstrum which is obtained by implementing inverse Fourier transform (IFT) to the logarithm of the spectrum given by:

$$C_p = \left| \mathscr{F}^{-1} \left\{ \log \left(|\mathscr{F}\{f(t)\}|^2 \right) \right\} \right|^2$$

(4.44)

It is the method used for analyzing periodic information in the spectrum and therefore has wide applications in investigating the vibration signal. The following work in [42][24][43], the Cepstrogram, is proposed that extracts and investigates the periodicity in the MDS obtained by STFT and the equation is given by:

$$C_p = \left| \mathscr{F}^{-1} \left\{ \log \left(|STFT\{x(t)\}(\tau, \omega)|^2 \right) \right\} \right|^2$$

(4.45)

In the transformed Cepstrogram domain, the variable of the Doppler frequency in the spectrogram now becomes the quefrency which is a measure of time. The inverse of the quefrency would provide the fundamental frequency of the signal. For its application to the rotation frequency estimation of the drone. A rotor with rotation frequency f_0 would generate flash lines with a short integration interval and HERM lines with a long integration interval in the spectrogram that are related to rotation frequency and the number of blades in the rotor. By implementing Cepstrogram analysis to the drone measurement, a peak in the quefrency would be observed according to the equation:

$$f_{quefrency} = \frac{B}{f_0}$$

(4.46)

where B is the number of blades per rotor. This is because the spectrum of the rotor consists of periodic harmonics components, which are multiple integers of the fundamental rotation frequency. Therefore, with an estimated number of blades $\hat{B}$ from IRT and strong peaks in the Cepstrogram, rotation frequencies can be estimated with this spectrogram-based method.

4.6. CONCLUSION

In this chapter, the signal processing pipeline and the methodology used in the algorithm are introduced. The whole signal processing chain can be generalized into 2 blocks and summarized as follows:

- **Detection and tracking with PF-TBD**

  The algorithm implements a novel TBD algorithm combining the electromagnetic model of the drone for joint tracking, detection, and estimation of drone dynamic characteristics. Upon a detection, the estimated drone state including the range, velocity, magnitudes of the drone body and rotor, and rotation frequency will be used in the following drone characteristics estimation block.

- **Characteristics estimation with model-based and spectrogram-based approaches**

  With the estimated state of TBD, a novel model-based number of rotors and the corresponding multiple rotation frequencies estimation algorithm is developed.

  Followed by a unified processing chain, a fusion of spectrogram-based drone constructional characteristics estimation methods is designed to estimate the number of blades per rotor, the blade length, and the rotation frequency for every rotor.

4

5

RESULTS SIMULATION AND VALIDATION USING REAL RADAR MEASUREMENT

This chapter presents the results and analyzes the performance of the TBD and estimation algorithms from synthetic data and experimental measurements. Section 5.1 introduces the simulation parameters and scenarios of the synthetic data. The results of the TBD algorithm and the analysis of the detection and estimation performance are provided in Section 5.2. Section 5.3 gives the results and the performance metric for the estimation of drone characteristics. Section 5.4 shows the results of the algorithm from the experimental measurement and the conclusion of this chapter is given in Section 5.5.

5.1. SIMULATION SETUP

With the proposed TBD algorithm introduced in the previous chapter, the synthetic measurements of the drone are first generated to validate the algorithm and analyze its performance.

For the generation of the synthetic data, the radar and drone parameters are set in Table 5.1. These parameters are chosen based on the experimental measurement data from PARSAX radar working at S-band with $240us$ PRI, 50 MHz bandwidth, providing range resolution of 3 meters. The table also gives some constructional parameters of the simulated drone DJI M200. In particular, the magnitudes α_{body} and α_{rotor} do not represent the real reflectivity of the corresponding components, as the reflectivity of the drone body is usually 100 times greater than that for the blades, and these simulation values accommodate the constant coefficients to make within the simulation data the value of body-to-blade spectrum components ratio comparable to the real measurement.

With configured parameters, the synthetic measurement would be simulated as follows:

Simulation parameters	Value
Carrier frequency	3.315 GHz
Pulse repetition interval	240 us
Bandwidth	50 MHz
Blade length	0.216 m
Magnitude of body	100
Magnitude of rotor	1500

Table 5.1: Simulation parameters

- The drone is located 249 meters away from the radar and approaching the radar with a speed of 2 m/s.

- Each measurement has a duration of 6 seconds and consists of 100 CPIs with each CPI having 256 pulses. The algorithm will provide a state estimation and detection probability for every CPI, and the track of the drone state within this 6 second measurement would be obtained.

- For CPI from 1 to 20 and 70 to 100, the drone signal is removed and filled with WGN to further evaluate the performance of the TBD algorithm in terms of false alarm and miss detection analysis.

Figure 5.1 illustrates the simulation data for a 4-rotor drone configuration. Fig. 5.1(a) gives the received time-domain electromagnetic signal of the rotor, where periodic flashes are contributed by the rotating blades of the rotor. Fig. 5.1(b) gives the received signal of a 4-rotor drone with random initial blade angles and varied rotation frequencies. Due to the coherent summation of 4 rotors, there are more complicated flashes. Fig. 5.1(c) gives the range-time map of the synthetic measurement of 6 seconds, and the movement of the drone can be observed. With a radial velocity of 2 m/s and range resolution of 3 meters, range migrations occur every 1.5 seconds. In Fig. 5.1(d), the drone signal is removed from the CPI number 1 to 20 and from 70 to 100 to evaluate the performance of the algorithm.

5.2. RESULTS FROM TRACK-BEFORE-DETECT WITH PARTICLE FILTER

With generated synthetic measurement, the PF-TBD algorithm is applied with following parameters: number of particles = 10000, particles are initialized as $r_0 \sim \mathcal{U}[200, 300]$, $v_0 \sim \mathcal{U}[-5, 5]$, $\alpha_{body0} \sim \mathcal{U}[50, 150]$, $\alpha_{rotor0} \sim \mathcal{U}[1000, 2000]$ and the initial existence state as well as the death and birth probability of the drone are set to be 0.05. The SNR of the observation measurement is set as 15 dB and the noise level is measured based on the background noise without target. Notably, due to the range resolution of 3 meters, the process noise level of range σ_r is set to be 50 such that, in the prediction procedure of new particles, the range difference of 3 meters can be covered in case of range migration happens.

(a) Time-domain single rotor synthetic data

(b) Time-domain 4-rotor synthetic data

(c) Range-time map

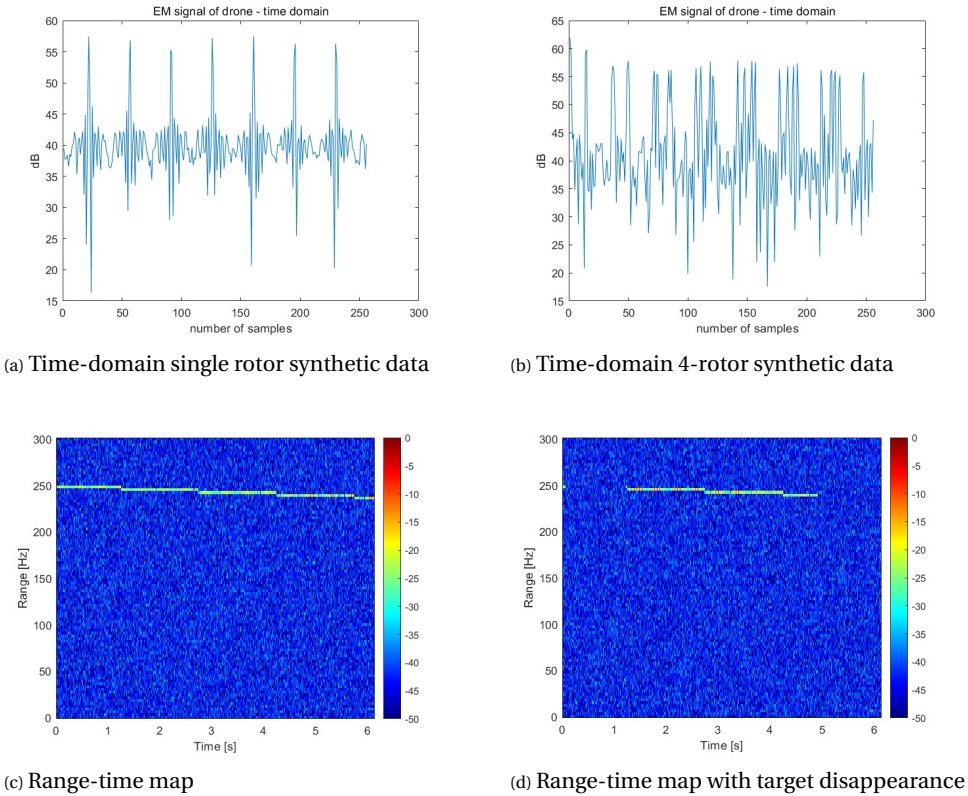(d) Range-time map with target disappearance

Figure 5.1: Synthetic drone measurement represented in different domains

Figure 5.2 provides the estimation results of the drone from the particle filter. Figure 5.2a gives the existence probability of the drone. From CPI 1 to 20 where the drone is absent, a low detection probability is estimated from equation 4.29 as the existed WGN does not match the electromagnetic model of the drone, a low likelihood is calculated from 4.18. As a result, the resampling algorithm will remove the particles with existence $E = 1$ and duplicate the particles with $E = 0$. Another observation is that there are 2 fluctuation and drops in the existence probability at CPI 47 and 72. This is caused by the range migration of the drone from one range bin to another. Due to the 'loss' of the drone, a portion of particles that remain in the previous range bin are transitioned from target presence to target absence state but soon after the reinitialization, the existence probability increase again. Another observation worth noting is that there are some delay in the transition of the existence probability. If choosing 0.6 as the detection threshold of the existence probability. The appearance of the drone at CPI 21 is detected at CPI 24 and the disappearance of the drone at CPI 80 is not observable until CPI 82. Such delay is the processing time and iterations needed for the PF to stabilize the dynamic state estimation and follow the drone. Figure 5.2b gives the results of range bin estimation. The estimated range are converted to corresponding range cells with res-

olution of 3 meters and an accurate track of the target can be obtained. In Figure 5.2c and 5.2d, The estimation results of the velocity and rotation frequency are given. After the presence of the drone, both velocity estimation and rotation frequency estimation quickly locate and follow the dynamic state of the drone from initialization interval of the particles. Similarly, due to the range migration at CPI 47 and 72, 2 outlier estimation appeared but quickly restore and converge back towards the true parameter values of the drone.
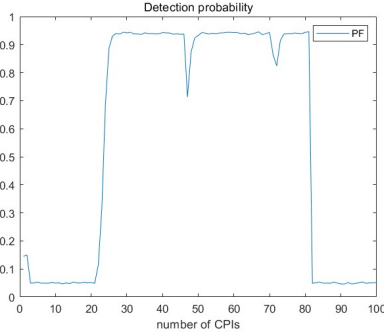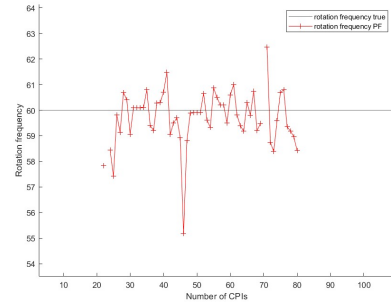

(a) Target existence probability
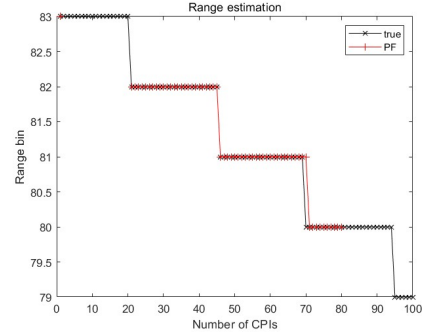
(b) Range estimation results
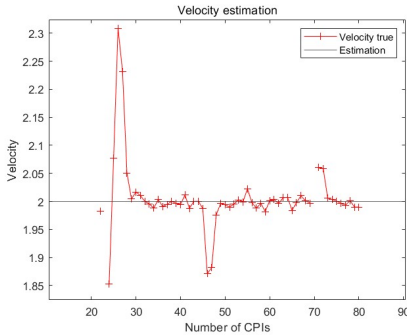
(c) Velocity estimation results

(d) Rotation frequency estimation result

Figure 5.2: Drone state and existence estimation results from particle filter

5.2.1. Performance analysis

Detection performance

For the detection of the TBD algorithm, it is to determine the target state - whether the target is present($E = 1$) or absent($E = 0$) and thus two corresponding hypotheses are defined as:

1. H_1: $E = 1$, drone is present

2. H_0: $E = 0$, drone is absent

Then based on the hypotheses and decisions, 4 types of outcomes can be obtained:

1. Hit: H_1 is true and decision of H_1 is made;

2. Miss: H_1 is true and decision of H_0 is made;

3. False alarm: H_0 is true and decision of H_1 is made;

4. Correct rejection: H_0 is true and decision of H_0 is made;

The probability of case 1 - probability of detection P_D and case 3 - probability of false alarm P_{FA} are evaluated in the performance analysis of the TBD algorithm.

The measurements under test are synthetic data with varying SNR from -5 dB to 10 dB, and each has the duration of 100 CPIs. The drone is present from CPI 21 to 69 and absent in other time. A detection decision is made if the target existence probability is greater than the factor $\gamma = 0.7$. As a comparison, a energy-based detector CFAR is also applied to the measurement of each CPI with a training cell size of 20, guard cell size of 2 and false alarm rate of 0.01. The results of average detection probability and false alarm rate from both detectors after 100 runs of algorithm in each SNR case are listed in Table 5.2. The results show that the PF-based TBD algorithm is able to make true positive detection at low SNR case, having the detection probability of 57% at 5 dB SNR and 87% of detection probability at 0 dB. The detection probability increase with increment of SNR and the false alarm rate decrease correspondingly, achieving the detection probability of 97% and a false alarm rate of 2% at 10 dB SNR. The performance of the energy-based CFAR, however, is deteriorated at low SNR and have 0% detection probability for SNR below 5 dB as the power of the target signal can not be distinguished from the noise floor.

SNR	TBD		CFAR	
	P_D	P_{FA}	P_D	P_{FA}
-5 dB	0.57	0.05	0	0
0 dB	0.87	0.04	0	0
5 dB	0.95	0.032	0.92	0.01
10 dB	0.97	0.02	1	0.02

Table 5.2: Detection performance comparison of TBD and CFAR

Estimation performance

For the estimation performance analysis, the TBD algorithm is implemented to the synthetic measurement with SNR at 10 dB, 15 dB and 20 dB and each SNR case runs on 100 measurements. The root mean square error (RMSE) is calculated to evaluate the estimation error, and the equation is given by:

$$\text{RMSD} = \sqrt{\frac{\sum_{i=1}^{N} (x_i - \hat{x}_i)^2}{N}} \tag{5.1}$$

(a) Velocity estimation results
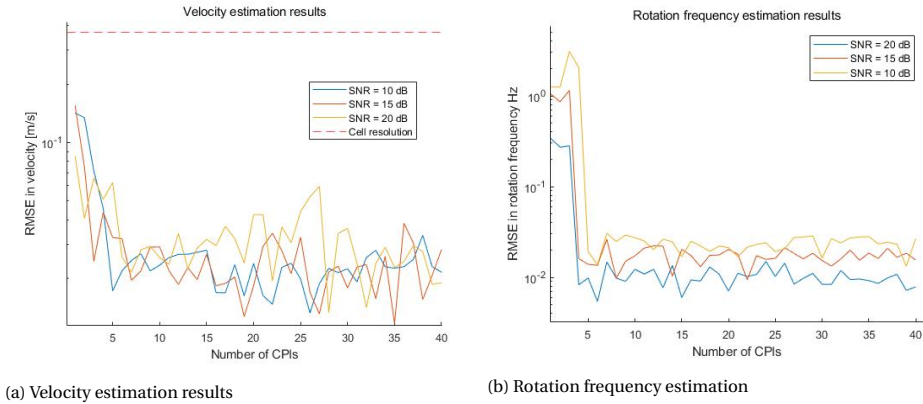
(b) Rotation frequency estimation

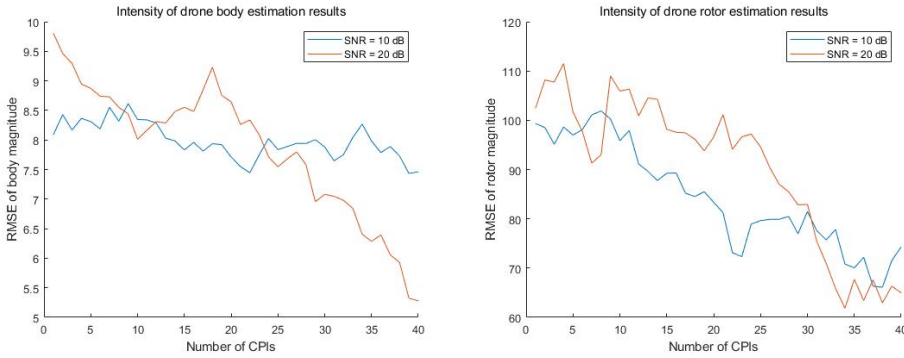Figure 5.3: Estimation results with different SNR

where x_i is the true value of the variable and $\hat{x}_i$ is the estimation result. The RMSE is calculated for the velocity and rotation frequency in terms of the number of CPIs, and the results are illustrated in Figure 5.3.

Figure 5.3a provides the RMSE of the velocity estimation results. The RMSE decreases with the increase of number of CPIs. With higher SNR, a faster convergence and stabilization of the particles can be observed. As a reference, the velocity cell resolution of 0.34 m/s is calculated based on the observation period of one CPI. A better performance beyond the cell resolution can be observed from the results. Figure 5.3b provides the estimation results of rotation frequencies. With increasing SNR, faster convergence and smaller fluctuation can be observed, and average deviations of the rotation frequency within 0.1 Hz are achieved in the estimation results.

However, while accurate velocity and rotation frequency estimation results are achieved, the estimation of body and rotor signal magnitudes has deteriorated performance, as illustrated in Figure 5.4. The result shows that both drone body and rotor intensity estimations have a proportional change with time but do not converge to the true value in 40 CPIs, having an average deviation of 8% and 6% from the true intensity magnitudes. This is due to the relaxed constraints of variables α_0 and α_1. While the likelihood function given in Equation 4.25 is more sensitive to drone dynamic parameters such as range, velocity, and rotation frequency, the signal magnitudes of body and rotor play a less important role during the importance weights update and resampling steps. As a result, a deteriorated performance of the signal magnitudes estimation is observed.

5.3. RESULTS FROM DRONE CHARACTERISTICS ESTIMATION

After obtaining the detection and tracking results of the TBD algorithm, the dynamic state of the drone can already be estimated, including the range, velocity, rotation frequency, and magnitude of the signal. These results are used as prior information in model-based and spectrogram-based characteristic estimation approaches to provide information of the range bin where the drone appears and the initial guess of the rota-

(a) Body intensity estimation results

(b) Rotor intensity estimation results

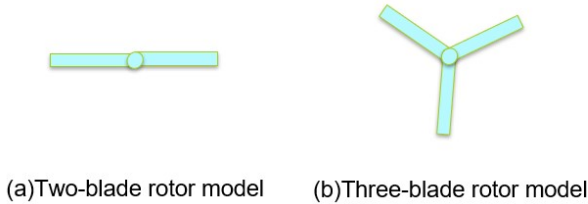Figure 5.4: Estimation results with different SNR

(a)Two-blade rotor model   (b)Three-blade rotor model

Figure 5.5: Rotor model with different number of blades

tion frequency interval.

5.3.1. NUMBER OF BLADES PER ROTOR ESTIMATION

As the spectrogram-based estimation processing pipeline illustrated in Figure 4.9, the processing starts with the number of blades per rotor estimation with IRT. In the processing block of number of blades estimation, it receives the estimated rotation frequency and the range bin where the drone appears as input and return the IRT result where the number of rotor can be extracted as the output.

Figure 5.5 provides the geometry configuration of the rotor with (a) 2 blades and (b) 3 blades. For a 2-blade rotor, the blades are spaced with 180° angle shift and for a 3-blade rotor, they are evenly spaced with angle difference of 120°. Such configuration would directly influence the received signal and different flash patterns can be observed in the MDS.

To obtain the flashes of the rotating blade in MDS, STFT is implemented in the range time profile with a short integration duration of 8 pulses(1.92 us). This is aimed to ensure that the observation window is shorter than the rotation period of the blade, such that

the flash lines and rotation cycles are visible.

Figure 5.6 shows the MDS of the simulated measurement and the corresponding IRT results. In the simulation, the rotor of the drone has the rotation frequency of 60 Hz and in the duration of one CPI which is consisted of 256 pulses, 3.68 periods of full rotation cycles can be observed. In the processing pipeline, the rotation rate can be estimated from the TBD algorithm and the IRT result in 5.6b accurately represents the geometry of the blade construction. Figure 5.6c gives the MDS of the 3-blade rotor measurement and the flash lines now consists of 3 sinusoidal patterns with phase shift of 120°. With properly estimated rotation frequency, the IRT result again is able to reconstruct the tomographic image of the rotor and provide the estimation result.
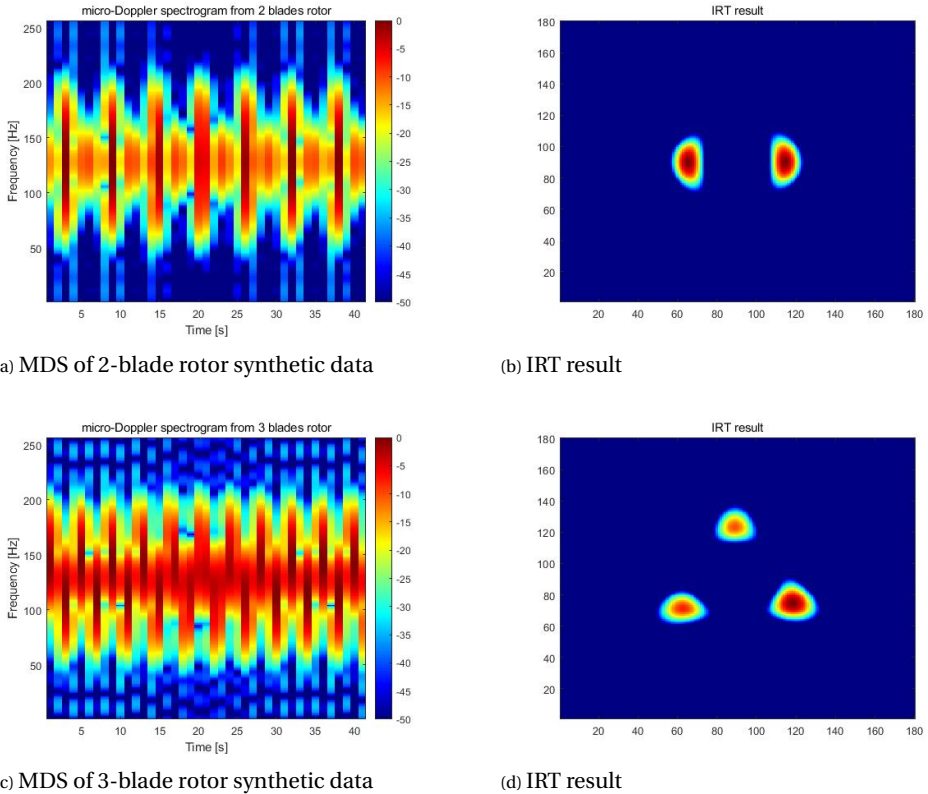

(a) MDS of 2-blade rotor synthetic data

(b) IRT result

(c) MDS of 3-blade rotor synthetic data

(d) IRT result

Figure 5.6: Number of blades per rotor estimation results

5.3.2. ROTATION FREQUENCY ESTIMATION

After the number of blades estimation, the spectrogram-based rotation frequency estimation can be implemented with the detected range bin where the drone locates from TBD algorithm and the number of blades per rotor as input and return the detected rotation frequencies of the drone as output. This procedure is complementary to the rotation frequency estimation from TBD. As for a multi-rotor drone, its rotor could have

multiple different rotation frequencies when it is moving while in the proposed TBD, only the strongest rotation frequency component would be estimated. Therefore, the spectrogram-based rotation frequency estimation with Cepstrogram analysis is implemented to validate as well as complement the rotation information of the drone.

To obtain the Cepstrogram, STFT is firstly applied to the received data. However, unlike the processing in number of blades estimation which selects a short integration duration to capture the flashes of the blade, the Cepstrogram analyze the period information of the harmonics from HERM lines. Therefore, a longer integration interval of 256 pulses (0.06 s) is selected to obtain the HERM lines in the MDS.

Figure 5.7 gives the signal processing results with a long integration interval. In Figure 5.7a, the flashes and rotation cycles of the blade is no longer visible, instead, HERM lines which are separated related to the rotation frequencies and number of blades per rotor are presented. By plotting one column of MDS, the spectrum in Figure 5.7b gives a closer view of the spectral lines. The peak in the spectrum is the strongest reflection contributed by the drone body, while the surrounding spectral lines are contributed by the rotating blades. These spectral lines are harmonics, having the frequency as the integer times of the fundamental rotation frequency with space between adjacent lines equal to $\frac{1}{T_{rot}}$ where T_{rot} is the rotation period. If the drone have multiple rotation frequencies, alignment of multiple spacing period can be observed in the spectrum. Then, the Cepstrogram is obtained by implementing IFT to the logarithm of the spectrogram with the equation given in 4.45.

Figure 5.8 shows the Cepstrograms of the drone measurement and estimated rotation frequencies. Figure 5.8a gives the Cepstrogram of the simulated DJI M200 with all 4 rotors have rotation frequency at 60 Hz, the variable in the y-axis of the Cepstrogram is the quefrency which measure the period of the spectral lines given by the inverse of the rotation frequency. It can be converted to the rotation frequency by the equation:

$$f_{rot} = \frac{B}{f_{que}} \tag{5.2}$$

where B is the estimated number of blades per rotor from the previous section. From the results of the Cepstrogram, while the strongest response is located at quefrency = 8 ms, another strong response can be observed at 16 ms but with a lower signal power which is one harmonic of the fundamental frequency. By converting to rotation frequency, they are 60 Hz and 120 Hz respectively. To reduce the interference from the harmonics, 2 approaches are considered as follows:

- Implement power threshold for rotation frequency extraction. The harmonics components have less concentrated signal power than the fundamental frequency components. Therefore, after the normalization based on strongest fundamental frequency signal, a hard threshold is set at -5 dB and remove the quefrency components below that level.

- Selection of the rotation frequency interval based on the normal operational rotation frequency of the drone. With estimated rotation frequency from TBD as well as normal operating rotation rate of the drone, it is possible to remove the quefrency representing extremely high or low rotation rate and focus on a reasonable region of interest centered around the estimation result from TBD.

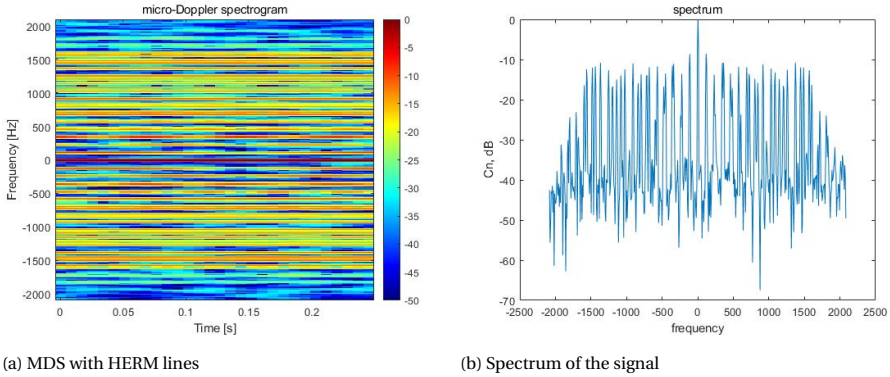(a) MDS with HERM lines

(b) Spectrum of the signal

Figure 5.7: Signal processing results with a long integration interval

With above harmonics removal methods, the extracted rotation rate is given in Figure 5.8b, a single rotation frequency of 59.5 Hz is detected. Figures 5.8c and 5.8d implement the same processing, but for the simulation data with 2 rotation frequencies, one pair of rotors has the rotation frequency of 50 Hz and the other has that of 60 Hz. While 2 strongest peak at 50 Hz and 60 Hz can be clearly obtained, more harmonics can be observed at 25Hz, 30Hz, 100Hz, and 120 Hz. With the help of the selection of the power threshold and rotation interval, Figure 5.8d still accurately extracts the 2 fundamental rotation rate.

However, while multiple rotation rates can be estimated from the Cepstrogram analysis, if the rotors do not have completely different rotation rates in each rotor, it is not possible to estimate the number of rotors from this stage.

5.3.3. BLADE LENGTH ESTIMATION

After number of blades estimation and rotation frequencies estimation, the final spectrogram-based blade length estimation is implemented. This processing block takes the rotation frequencies and the spectrum of the signal as input and return the estimated blade length. The blade length is estimated based on spectrum by implementing FFT to the received signal. Although the maximum angular velocity of the blade can already be observed in the MDS with flash lines as given by Figure 4.10a, the estimation accuracy is greatly limited by the frequency resolution due to the use of short integration interval. Therefore, it is still desired to implement the FFT with a long integration time to achieve a higher frequency resolution and the integration of multiple rotation cycles can also help form a shaper edge in the frequency band contributed by the blade tip, making the estimation of the maximum rotation frequency easier.

By implementing FFT with a integration time of 2 CPIs, the obtained spectrum is shown in Figure 5.9. Due to the existence of 2 rotation frequencies at 50 Hz and 60 Hz, the spectral lines are the combination of the harmonics from these two fundamental frequencies and make the shape of the frequency band more complicated. With the obtained spectrum, the Doppler frequency which corresponds to the moving velocity of the drone body f_{body} can be estimated by locating the peak in the spectrum. Then, the
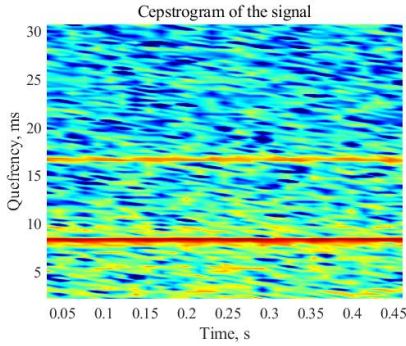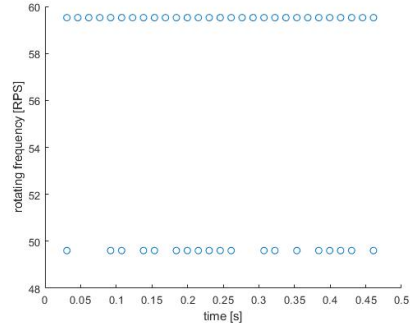
(a) Cepstrogram of simulation data with single rotation frequency
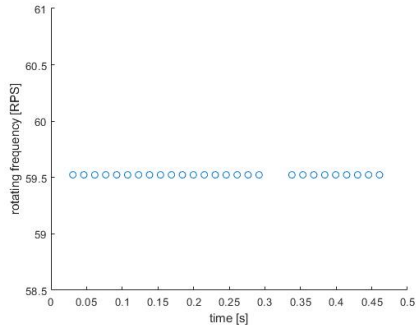
(b) Extracted rotation frequency result
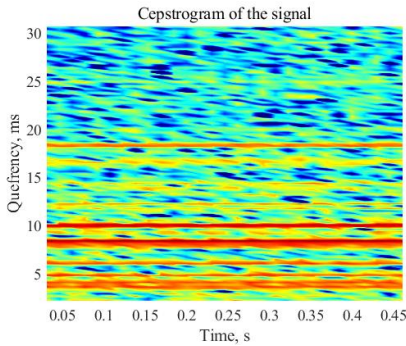
(c) Cepstrogram of simulation data with different rotation frequencies

(d) Extracted rotation frequency result

Figure 5.8: Cepstrogram and rotation frequency estimation

envelope is taken to smooth the peaks of the harmonics with a window length factor of $\frac{N_{nfft}}{30}$ where N_{nfft} is the number of points used in the FFT. Next, the first order derivative is taken to find out the edge of the frequency band which is related to the maximum linear velocity contributed by the blade tip. From Figure 5.9b, the maximum frequency is chosen where the derivative of the envelope is equal to 0. This selection provides a more robust estimation of the edge frequency than selecting the peak in the derivative, which is more sensitive to the shape and patterns of the harmonics. With extracted maximum edge frequency f_{edge}, the maximum frequency introduced by the blade tip can be estimated as $f_{blade} = f_{edge} - f_{body}$ and the blade length L can be calculated with estimated rotation frequency given by:

$$L = \frac{f_{max}\lambda}{2 \times 2\pi \hat{f}_{rot}} \tag{5.3}$$

Table 5.3 gives a short summary of the estimation results from the spectrogram-based drone characteristics estimation. With simulated synthetic data at SNR = 15 dB, the number of blades per rotor can be accurately estimated with an accuracy of rotation
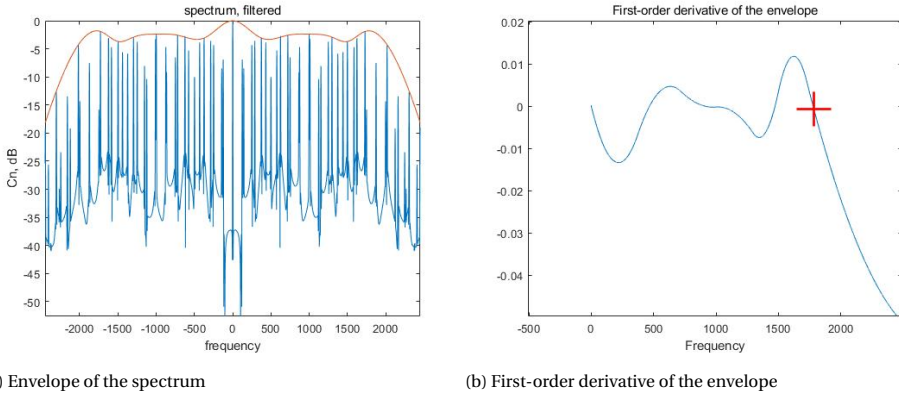
(a) Envelope of the spectrum

(b) First-order derivative of the envelope

Figure 5.9: Spectrum-based blade length analysis

frequency estimation of 99 % and a blade length of 97%.

	Simulation parameters	Estimation results	Accuracy
Number of blades per propeller	2	2	100%
Rotation frequency	60 Hz	59.5Hz	99%
Blade Length	21.6 cm	20.94 cm	97%

Table 5.3: Spectrogram-based estimation results

5.3.4. NUMBER OF ROTOR AND ROTATION FREQUENCY ESTIMATION

With all the information and characteristics estimated from the previous section, the model-based number of rotor estimation will be implemented. The algorithm takes the estimated range, velocity, magnitude of the drone body and rotor, as well as extracted rotation frequencies from the Cepstrogram analysis as prior information. The characteristics, including the number of rotors, corresponding rotation frequencies, and blade angles, will be estimated.

Results from 2D grid search

The number of rotor estimation is implemented in the synthetic data with simulated rotation frequencies given as $[62.4Hz, 62.1Hz, 61.8Hz, 62.7Hz]$ and initial blade angle of $[107°, 3°, 51°, 68°]$ which is difficult to distinguish by spectrogram-based approaches, as it requires a long integration time to achieve enough frequency resolution. Then, the 2 dimensional grid search for the variables of rotation frequency and blade angle is applied. The grid search evaluates the parameters that can best fit the electromagnetic model of the drone given in 4.33 with the likelihood as the scoring parameter, which is
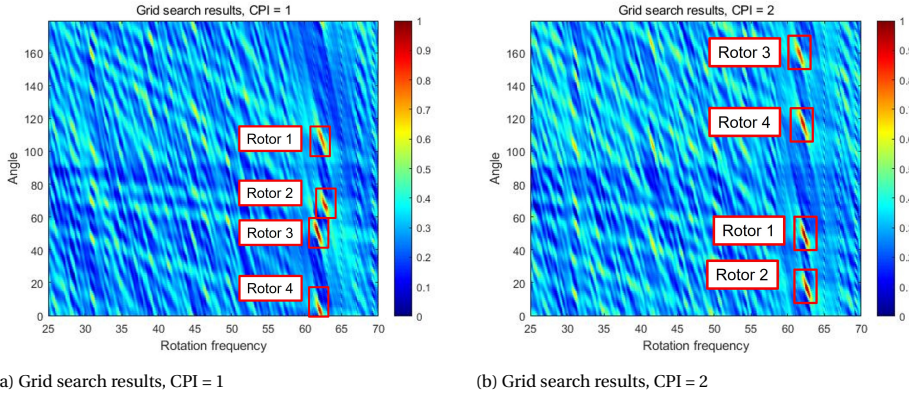
(a) Grid search results, CPI = 1

(b) Grid search results, CPI = 2

Figure 5.10: 2D grid search results of rotation frequency and blade angle

given by:

$$l(z_k|\hat{x}_n, \omega, \phi) = \frac{1}{2\pi|\Sigma|} e^{-\frac{1}{2}(z_k - H(\omega, \phi))^H \Sigma^{-1}(z_k - H(\omega, \phi))} \tag{5.4}$$

In the processing, the grid of rotation frequency is generated from 30 Hz to 70 Hz with increment of 0.1 Hz and the blade angle is initialized from 0° to 179° with increment of 1. Figure 5.10 illustrates the grid search output from 2 consecutive CPIs with scoring metric normalized to the interval from 0 to 1. From Figure 5.10a, Although 4 rotors have very close rotation frequencies, due to the difference in blade angles, 4 strong responses can still be observed. In the next CPI given in Figure 5.10b, the position of each rotor has changed and become more separated due to the rotation of the rotor. Notably, due to the coupling of the rotation frequencies and angles, 4 strongest responses are not centralized and have some spread and ambiguity in rotation frequency and angles. This also causes the result that, along some certain directions in the grid, there are side lobes and harmonics with slightly higher likelihood. To extract the detected rotor parameters, a two-dimensional CA-CFAR is applied to the grid search results with guard band size [2,2] and training band size [3,3]. In particular, the false alarm rate is set to 20% with a scoring metric threshold of 0.65. This is aimed at ensuring that the strong responses from the rotors can be detected from the side lobes and harmonics at the cost of introducing more false alarms. Then the false alarm removal approach is applied.

Results from false alarm removal

In the algorithm, 2 types of approach are considered: rotation frequency interval threshold and tracking-aided noise removal. The first approach takes both a fixed threshold of normal operational rotation frequency to avoid harmonics at low frequencies below 30 Hz and high frequencies above 100 Hz and a dynamic threshold, which is prior information from the algorithm TBD and the results of the Cepstrogram-based frequency analysis. This would further help focus on the rotation frequency interval of interest. The second approach track the frequency and angle of the rotor and predict its position in the next CPI while the noise and some weak harmonics couldn't have the consistent
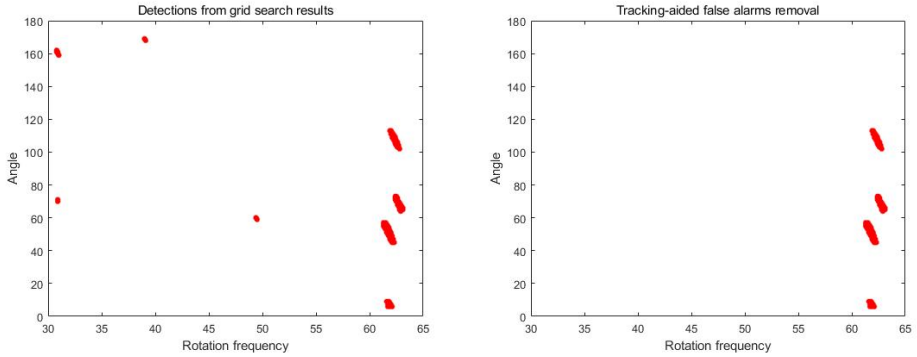
(a) Detection results from CPI 1

(b) Detection results after tracking-aided false alarm removal

Figure 5.11: Detection results from grid search

5

existence in the predicted positions, therefore false alarms can be reduced. Figure 5.11 shows the results of 2D CA-CFAR and the tracking-aided false alarm removal results. In Figure 5.11a, while the presence of 4 rotors can be observed at a frequency around 61 Hz, there are some false alarms introduced by harmonics at 31 Hz and some noises at 40 Hz and 50 Hz. Then, for each detected point, their positions in the next CPI are predicted with the equation given by 4.37. Figure 5.11b shows the filtered detection results of CPI 1, harmonics and noises are successfully removed by comparing the predicted rotor positions and the detected rotor positions at CPI 2.

Results from tracking-aided rotor energy integration and clustering With previous 2D CA-CFAR detection and false alarm removal processing, the parameter combinations that have high likelihood originating from the rotors have extracted for each CPI. Then it is assumed that, in adjacent k CPIs, the rotation frequencies have minor change and can be considered as constant. Then the detections from previous $k-1$ CPIs will predict their positions and sum up at k^{th} CPI. Then, the density-based clustering algorithm dbscan is implemented to estimate the number of rotors existed at k^{th} CPI. Figure 5.12 illustrates the integrated detection points and clustering results. The colored point groups of 1 to 4 denote the recognized rotors, while red points with -1 value are classified as noise. This is achieved with the help of tracking. The parameter combinations $\{w_i, \phi_i\}$ that originate from the rotor would have more consistent existence with higher likelihood in the value. By tracking the position of the detection results in consecutive CPIs, such information is integrated and results in a denser distribution of the points. Then, dbscan with a clustering factor of $r \times k$ where r is the search radius and k is the number of integrated CPIs, the clustered results with information including the number of rotors, the corresponding rotation frequencies and the blade angles can be estimated.

Table 5.4 provides the ground truth of the simulation and the estimated results for the fifth CPI. Besides the properly estimated number of rotors equal to 4, by taking the average of the rotation frequencies and angles in each cluster group, accurate estimation parameters of each rotor can be obtained with 99% estimation accuracy at a SNR level of

	Rotor 1	Rotor 2	Rotor 3	Rotor 4
Simulation {Rotation frequency, angle}	{62.4 Hz, 51.5° }	{62.2 Hz, 101.9° }	{61.8 Hz, 119.5° }	{62.8 Hz, 41.4° }
Estimation results {Rotation frequency, angle}	{62.4 Hz, 51.9° }	{62.1 Hz, 101.3° }	{61.8 Hz, 119.7° }	{62.8 Hz, 41.8° }

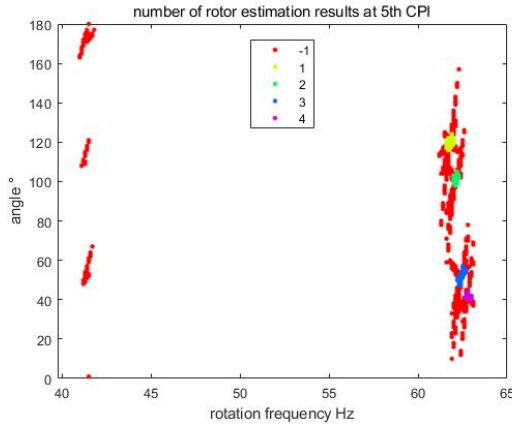Table 5.4: Comparison of simulation parameters and estimation results

Figure 5.12: Number of rotor estimation results with integrated detections

15 dB.

5.3.5. PERFORMANCE ANALYSIS

To analyze the performance of the proposed number of rotor estimation, a set of simulation is implemented as follows:

- The synthetic data is generated with 4 rotors and the rotation frequencies are uniformly distributed in the interval of $[55 Hz, 60 Hz]$ including the cases where the rotation frequencies of 4 rotors are closely aligned and separate away.

- Synthetic data are tested under different SNR from 5 to 25 dB and different numbers of CPIs used in tracking-aided integration, from 3 to 8 CPIs. In total, there are 500 synthetic measurement generated and tested.

Influence of tracking-aided rotor information integration

From the grid search output, the detected points give the information of the parameters including the rotation frequency, blade angle, and the likelihood value measuring how closely these parameters fit the model of the drone and thus are from one of the rotors. While the detection of the grid search output from single CPI with tracking-aided
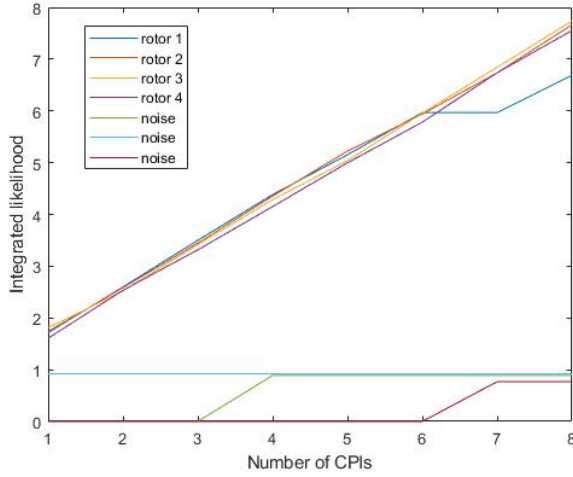
Figure 5.13: Integrated rotor likelihood with different number of CPIs

false alarm removal approach could sometimes provide good estimation of the number of rotors as illustrated in Figure 5.11b where the clusters of 4 rotors can be clearly observed. However, it could immediately lead to wrong estimation results when there is any rotor missing or other false alarms existed. Therefore, the tracking-aided number of rotor estimation approach is considered to track the position of the rotors in consecutive CPIs and integrate the points with high probability to achieve better discrimination from false alarms. Figure 5.13 gives the integrated rotor likelihood with increasing number of CPIs. It can be observed that the clusters with corresponding rotation frequencies and blade angles originated from true rotors have the likelihood values integrated with number of CPIs. In particular, rotor 1 is missing at CPI 6 and thus there is no likelihood integrated at this CPI, but the reappearance of rotor 1 at CPI 7 continues to increase the likelihood of rotor 1. Furthermore, although three false alarms appear at CPI = 0,3 and 6, they have nonintegrated likelihood values over CPIs and thus can be removed with a proper threshold of the likelihood.

Influence of data SNR and number of CPIs

As the number of rotor is a discrete variable. The accuracy of the estimation Acc used for the performance analysis is defined as

$$Acc = \frac{N_{n=M}}{\sum_n N} \tag{5.5}$$

where $N_{n=M}$ is the estimated results with rotor number equal to the true number M, which is 4 in the simulation and $\sum_n N$ is the total number of estimations. Figure 5.14 provides the estimation accuracy in terms of changing SNR and number of pulses.

For a given SNR, each curve shows the relationship that with an increasing number of integrated CPIs, the accuracy of the estimation of the rotor number increases and the
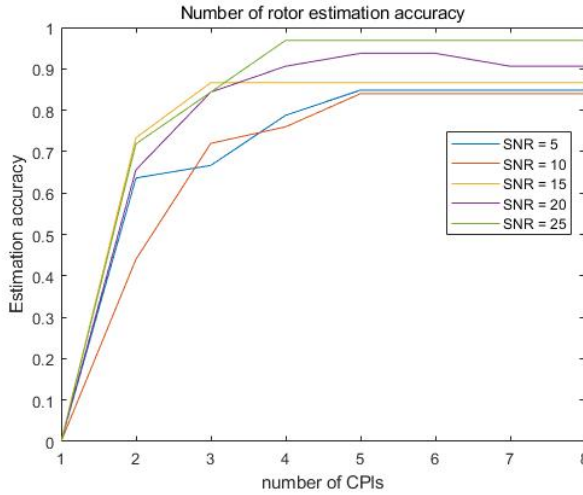
Figure 5.14: Integrated rotor likelihood with different number of CPIs

curves begin to saturate after 5 CPIs. This is due to the integration of the rotor informa-
tion illustrated in Figure 5.13. With increasing number of CPIs observed and tracked, the
cluster points that originate from the rotor are kinematic correlated and their likelihood
could be integrated over CPI making the decision of the number of rotor more confident.
It also has shown that the continuous observation of 5 CPIs is able to form the distinct
discrimination of rotors from the false alarms.

The results also show that for a given number of CPIs, the increase of SNR could also
help improve the accuracy of the estimation. For example, for the integration of 5 CPIs,
an estimation accuracy of 85% is achieved with SNR = 5 dB while an accuracy of 96 % can
be achieved with a SNR of 25 dB. This is because with low SNR, the drone signal is hidden
in the noise floor, leading to more false alarms or miss detection of the grid parameters.

Influence of the duration of CPI and ambiguity

From the grid search output, due to the coupling of rotation frequency and angles,
ambiguity exists in the detected rotor parameters causing a spread of high-likelihood
results in both rotation frequency and angle. Figure 5.15 illustrates the ambiguity of the
rotor position with different processing intervals. For a CPI defined with 512 pulses or
0.12 seconds, a rotation frequency resolution of 0.4 Hz and angle resolution of 9° can be
measured in the position of the main lobe of -3 dB. Then, with decreasing processing
interval of the grid search, the rotation frequency resolution decreases correspondingly
while the angle resolution remain the same. In particular, in Figure 5.15d for a CPI of 32
pulses (0.008 seconds), which is shorter than one rotation period of the blade, which is
69 pulses (0.017 seconds), the grid search output is no longer available to estimate the
rotation frequency.

Table 5.5 provides the comparison of angle and frequency resolution of the proposed

model-based grid search method and frequency resolution of FFT which are given by:

$$\delta f = \frac{N}{f_s} \tag{5.6}$$

where N is the number of samples and f_s is the sampling frequency. From the results, while the angle resolution is independent of processing interval which remains around $9°$, the frequency resolutions from grid search and FFT both improve proportionally with the increase of processing interval and a 20 times better resolution from the model-based approach can be observed.

CPI interval	64 pulses	128 pulses	256 pulses	512 pulses
Angle resolution (Grid search)	9°	9°	10°	9°
Frequency resolution (Grid search)	3.3 Hz	1.8 Hz	0.8 Hz	0.4 Hz
Frequency resolution (FFT)	65 Hz	32 Hz	16 Hz	8 Hz

Table 5.5: Angle and frequency resolution in terms of processing interval

Error analysis

From the simulation results, while the false alarm removal and tracking-aided likelihood integration approaches have shown the effectiveness in improving the estimation accuracy of the rotor number. However, the following factors are found to make the algorithm suffer from worse performance.

- **Mismatch of range and velocity parameters** The proposed model-based number of rotor and rotation frequency estimation is based on the electromagnetic model and the scoring metric of the grid search is calculated based on the likelihood given by equation 4.32 which require the estimated range, velocity, body and rotor magnitudes as prior information and the estimation accuracy would influence the performance of the grid search results. Figure 5.16 illustrates the analysis of grid search results with different parameters. Compared to the results in Figure 5.16a with accurate estimated $\hat{r}$, $\hat{v}$, $\hat{\alpha}_{body}$ and $\hat{\alpha}_{rotor}$, Figure 5.16b calculate the likelihood with a range error of 2 meters. Due to such estimation error in range, a phase offset of $e^{-\frac{4\pi\Delta r}{\lambda}}$ is introduced where Δr is the error in range and a higher noise floor and a phase shift of $90°$ can be observed in the grid search results. Figure 5.16c illustrates the grid search results with a velocity error $\Delta v = 2m/s$, giving the mismatch in Doppler components as $e^{-\frac{4\pi\Delta v}{\lambda}}$. As a result, the positions of the rotors are completely disappeared. The last Figure 5.16d calculate the likelihood with a deviation of 20% in both drone body and drone rotor magnitude and very little influence is observed from the results.

- **Closely aligned rotation frequencies**

(a) Grid search output with CPI of 512 pulses

(b) Grid search output with CPI of 256 pulses

(c) Grid search output with CPI of 128 pulses
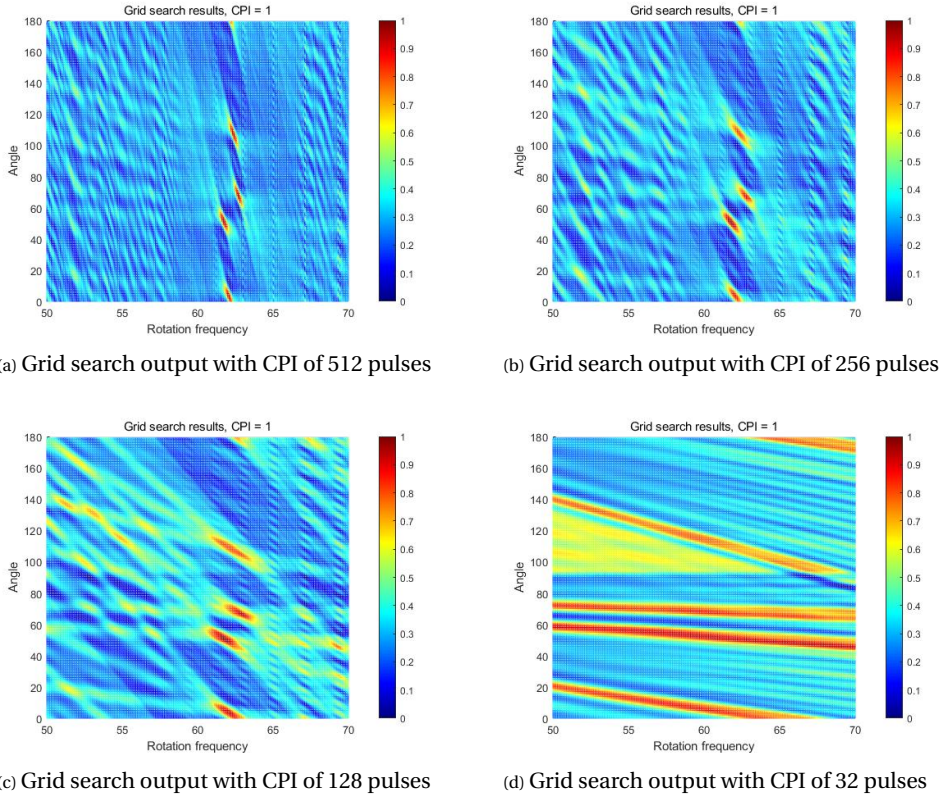

(d) Grid search output with CPI of 32 pulses

Figure 5.15: Grid search output with CPI of different durations

Another factor that would cause the deterioration in estimation performance is the case where all the rotation frequencies and blade angles are synchronized and cause close overlap in the gird search results. Figure 5.17 illustrates an example of the grid search outputs with highly overlapped rotor parameters. In Figure 5.17a, all 4 rotors have the rotation frequency around 62 Hz with slightly different angles. For instance, first 2 rotors on the top have the angle difference of only 20° and the other 2 rotors at the bottom have less separated distance and connected with side lobes which would lead to a miss detection for one of the rotors. Figure 5.17b gives the grid search output from the next CPI, where a worse case is observed. 2 rotors are completely overlapped at 170 Hz with undiscriminating angles, while the other 2 rotors are also overlapped but with a lower likelihood values. While with the help of tracking-aided approach to integrate and correlate the kinetic information of the rotors to achieve a higher likelihood for estimation results, such case with a lot of overlaps and miss detection of the rotor would require a much longer observation duration to achieve a good estimation results.
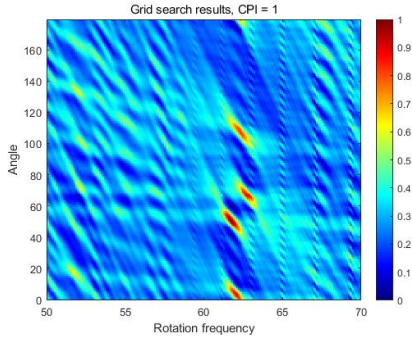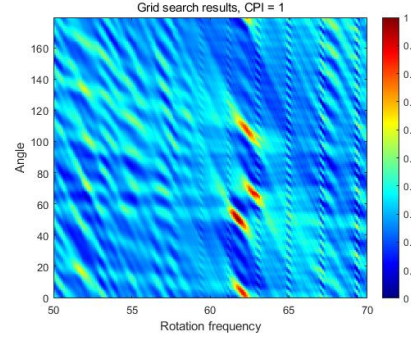
(a) Grid search output with matched parameters
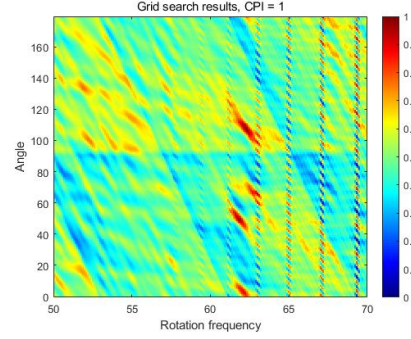
(b) Grid search output with mismatched range
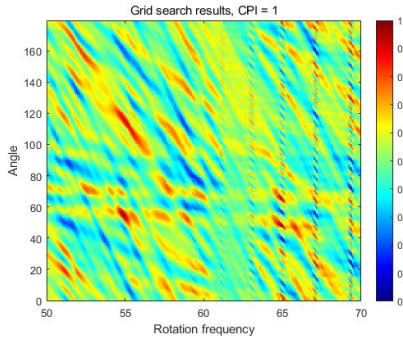
(c) Grid search output with mismatched velocity

(d) Grid search output with mismatched body and rotor magnitude

Figure 5.16: Error analysis of grid search result

5.4. REAL MEASUREMENT VALIDATION

5.4.1. MEASUREMENT SETUP AND SIGNAL PROCESSING

Radar configuration and measurement scenario

To validate the proposed algorithms with experimental results, the PARSAX radar is used to obtain the real measurement. PARSAX is a configurable research FMCW radar located in TU Delft. It has full polarimetric channel including HH, HV, VH and VV channels, high resolution with adjustable bandwidth up to 100 MHz and high sensitivity with receivers' floor around -93 dBm, giving it the possibility to measurement the weak targets at long distance.

Figure 5.18 shows the PARSAX radar and the measurement setup. The radar works on the S band with carrier frequency $f_c = 3.315GHz$, PRI $T_{PRI} = 240us$ bandwidth $B = 50MHz$ with range resolution of 3 meters. Two types of drone DJI 200 and DJI 600 were used in the measurement which are a 4-rotor drone and a 6-rotor drone correspondingly. Figure 5.18b illustrates the location of the radar and the experiment field. The drone is
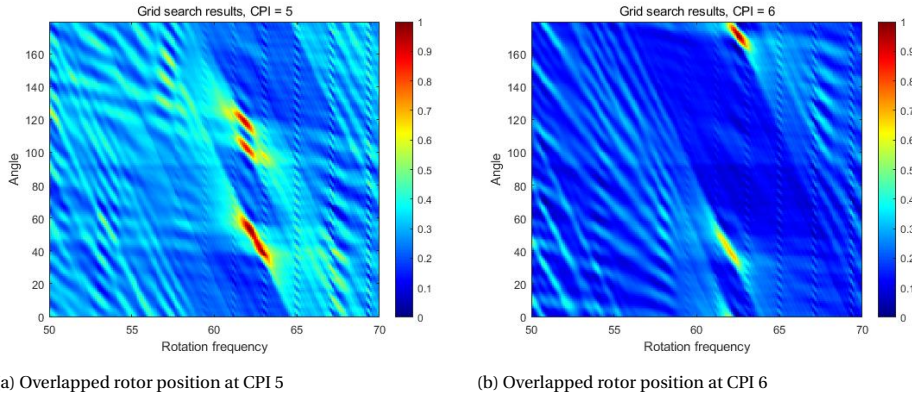
(a) Overlapped rotor position at CPI 5   (b) Overlapped rotor position at CPI 6

Figure 5.17: Grid search results with overlapped rotor positions
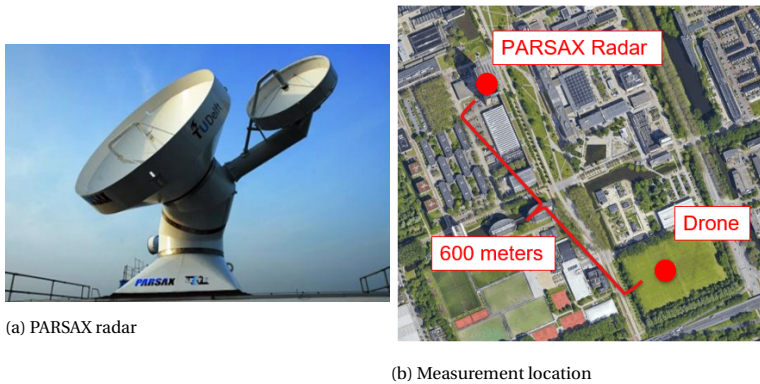

(a) PARSAX radar

(b) Measurement location

Figure 5.18: Measurement setup

approximately 600 hundred meters away from the radar and 2 sets of movement were recorded: (a) hovering, (b) moving forward and backward linearly. In addition to drone measurements, one measurement where the drone is absent was recorded to provide background noise information.

Signal processing and data representation

The raw signals received from the radar are digitized in-phase (I) signals and quadrature-phase (Q) signals, which contain the real and imaginary parts of the reflected signal. By combining the I/Q channels, the complex signals can be restored, which are phase-shifted, time-delayed versions of the transmitted signal and contain the information of the echo target. The measurements from PARSAX radar include full polarization channels and in the analysis of the drones, only horizontal-horizontal (HH) channel is used as the most significant kinematic movement of the drones are the rotation of the rotors in horizontal directions and those characteristics are most captured in HH channel. The
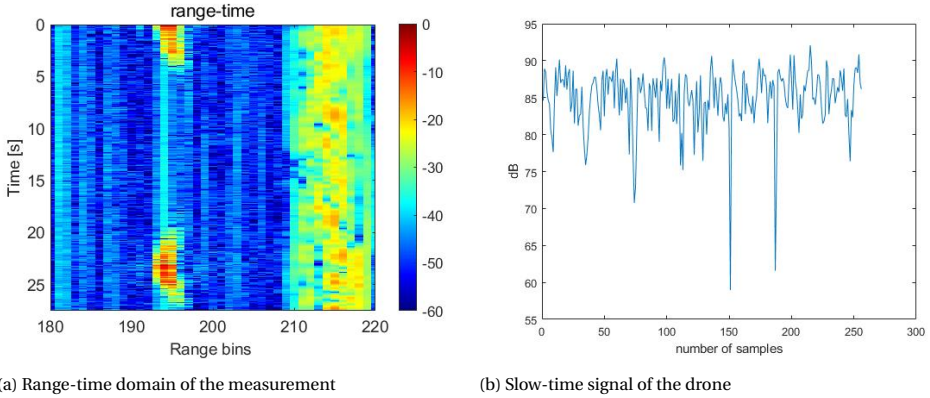
(a) Range-time domain of the measurement   (b) Slow-time signal of the drone

Figure 5.19: Real measurement representation

data is reshaped into a $M \times N$ matrix where M is the number of samples per chirp in fast time and N is the number of recorded chirps in slow time. Then a M points FFT is applied along the fast time axis and the range profile can be obtained. Figure 5.19 illustrates the measured data in the range-time domain and the signal of a range bin in the time domain. In Figure 5.19a, the drone is located in the range bin from 193 to 196 and present from 0 to 4 seconds and 20 to 26 seconds with motions of moving approach and away from the radar. Figure 5.19b gives one CPI of the measurement in the time domain in the 194 range bin where the drone appears. A cyclic period signal pattern similar to Figure 5.1b can be observed, which are the flashes of the rotating blades. These provide the characteristics of the drone, including rotation frequencies, number of rotors, and angles.

5.4.2. RESULTS FROM TRACK-BEFORE-DETECT WITH PARTICLE FILTER
With obtained range-time profiles after signal processing, the TBD is applied to the data to jointly detect and estimate the dynamic parameters of the drone, and the results are given in the Figure 5.20. Figure 5.20a illustrates one period of the measurement from 16 seconds to 27 seconds. The drone is absent in the period from 16 to 20 seconds, then appears from 20 to 26 seconds (from CPI 62 to 179), and then disappears again. The drone has the motion of first moving towards the radar and then away from the radar, and the range migrations occur in this period, which provides a good example for evaluating the performance of the developed algorithm.

Figure 5.20b gives the probability of the existence of the target. In the initial 62 CPIs, the absence of the drone is represented by the particles with drone state $E = 0$ and after the appearance of the drone at 20 seconds, the particles transition from $E = 0$ to $E = 1$ and reach a high probability of target existence at CPI 66. When choosing a threshold of $P_e = 0.6$ for drone detection, a detection probability of 97% is achieved with a false alarm rate of 4%.

Figure 5.20c provides the range estimation of the drone. The range state is not defined before the detection of the drone. After the detection, the range estimation quickly

locate the correct range bin at 195 from 186. 2 range migrations occur at CPI 88 and CPI 146 which accurately represent the trajectory of the drone in the measurement.

Figure 5.20d illustrates the change of the magnitudes of the drone body and the rotor. It represents the trend in the change in drone reflectivity, which increases when approaching the radar in range bin 194 and starts to fade when moving away.

The estimation of drone velocity is shown in Figure 5.20e. The blue line gives the estimation results from the particle filter, the orange line gives the Doppler velocity measured from the spectrum with detected range used as a reference for evaluating the estimation accuracy. For one CPI, the spectrum has the limited Doppler velocity resolution of 0.7 m/s and thus the resolution of the Doppler cell at $v_d \pm \frac{1}{2} v_{resolution}$ are drawn with red dash line. It can be observed that in most cases, the estimated velocity follows the change in velocity and lies within the same Doppler cell. However, some minor outlier and delay in the change of the velocity are observed under the high maneuver of the drone. Figure 5.20f provides the estimation of the rotation frequency, which is only one rotation frequency components from the multiple rotor. The estimated rotation frequency first remains around 57 Hz and then accelerates close to 70 Hz. Although lacking the ground truth of the rotation parameters, the estimated values can be validated with the following spectrogram-based analysis.

As the outputs of the TBD, the algorithm provides the estimated drone existence, range, velocity, signal magnitude and rotation frequency at each CPI where detection is reported. With such information, the following spectrogram-based characteristics estimation can be applied for a more detailed analysis of drone's dynamic and constructional characteristics.

5.4.3. RESULTS FROM DRONE CHARACTERISTICS ESTIMATION

Spectrogram-based characteristics estimation

Figure 5.21a gives the MDS of one CPI. A STFT is applied with a window duration of 8 pulses (0.002 s) to obtain the flashes of the rotating blades at a cost of frequency resolution. Then, an IRT is applied with estimated rotation frequency from TBD results and the configuration of 2 blades is obtained from the Figure 5.21b. It is worth noting that, although the position of 2 blades can be reconstructed with IRT, due to more complicated flashes in the MDS of the real measurement, the IRT results have less centralized energy projection than simulation results in Figure 5.6b.

Figure 5.22a gives the results of Cepstrogram-based rotation frequency analysis. The drone DJI M200 is moving towards and away from the radar. From 0 to 6 seconds, due to the absence of the drone, there is no rotation frequency detected. After 6.5 seconds, multiple rotation frequency components are detected with highly varying frequencies. In Figure 5.22b, it is the M600 drone hovering still with close rotation frequencies around 45 Hz. Although such Cepstrogram-based frequency estimation could provide additional validation and complementary estimation to the rotation frequency of TBD, there exists a compensation between time resolution and frequency resolution. For the highly maneuvering case in the Figure 5.22a, a long integration time would provide a more accurate estimation of the rotation frequencies but a worse resolution and sensitivity in the change of the frequencies, which remain the main limitation in the frequency domain-

(a) Range-time profile of the measurement

(b) Probability of target existence

(c) Estimated range bins

(d) Estimated body and rotor magnitude

(e) Estimated velocity

(f) Estimated rotation frequency
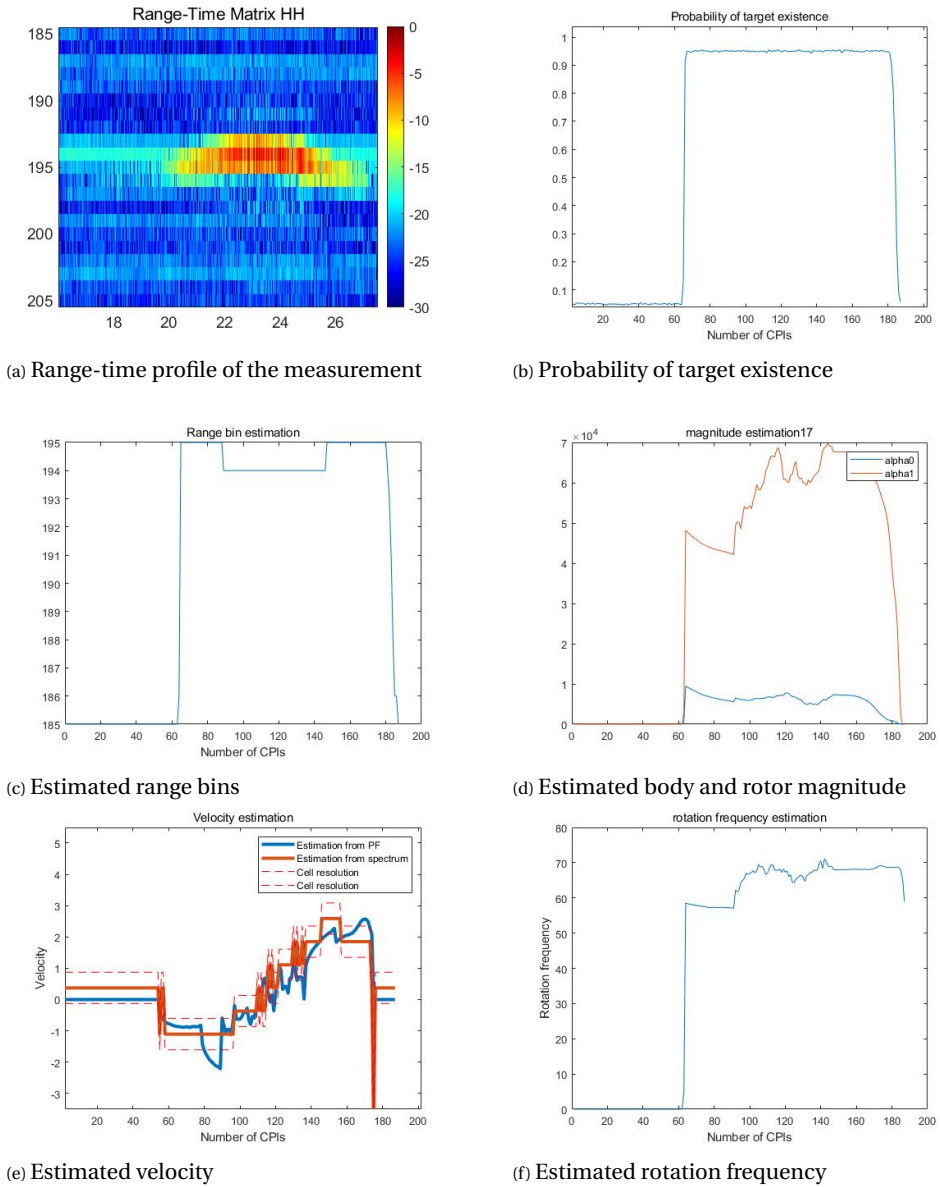
Figure 5.20: Estimation results from a particle filter for track-before-detect

based estimation approaches.

With the help of the tracking, the blade length estimation is implemented based on each CPI where a detection is reported, combined with the measured maximum rotation frequency in each CPI, the average blade length estimation accuracy is obtained. Table 5.6 gives the estimated blade length with measurements of the DJI M200. An average
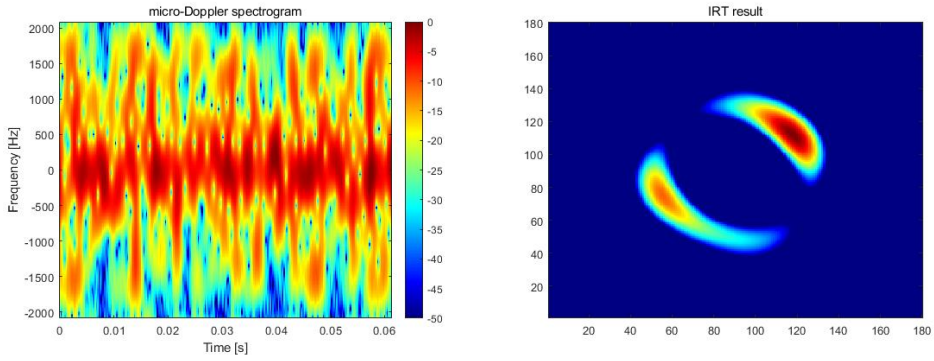
(a) Micro-Doppler spectrogram of 1 CPI

(b) Inverse Radon transform of the spectrogram

Figure 5.21: Number of rotor estimation
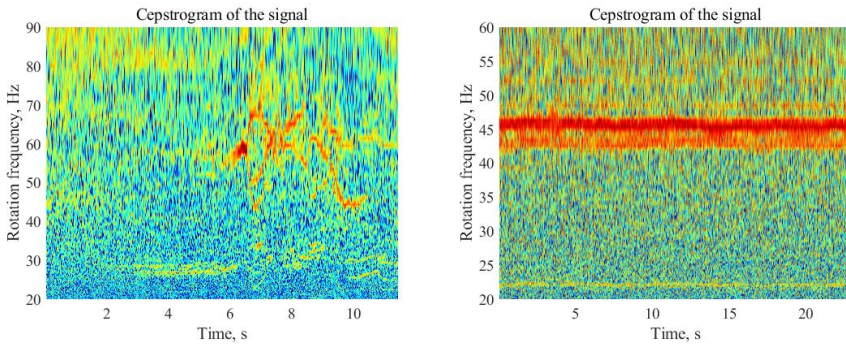
(a) Cepstrogram-based rotation frequency analysis of moving data

(b) Cepstrogram-based rotation frequency analysis of hovering data

Figure 5.22: Cepstrogram-based rotation frequency observation

	Blade length Ground truth	Estimated blade length	Estimated blade length with approach in [40]
DJI M200	0.216 m	0.229 m	0.255 m
Estimation error	-	6%	18%

Table 5.6: Estimation results of DJI M200

	Blade length Ground truth	Estimated blade length	Estimated blade length with approach in [40]
DJI M600	0.267 m	0.289 m	0.202 m
Estimation error	-	8%	32%

Table 5.7: Estimation results from DJI M600

blade length of 0.229 m is estimated with an error of 6% with respect to ground truth. A comparison of the estimation result with proposed methods in [40] is given, where the estimated blade length is 0.255 m with a higher error at 18%. Table 5.7 provides the estimation results from the DJI M600 measurement, while the proposed method achieves a similar estimation error at 8%, the method in [40] suffers from a deteriorated performance due to a superposition of multiple rotation harmonics and a more complicated envelope pattern in the spectrum shown in Figure 5.23a.Due to such fluctuations in the envelope, the peak position of the derivative of the envelope becomes ambiguous and unstable, while the zero-position in the derivative still gives a robust estimation of the edge frequency given in Figure 5.23b.

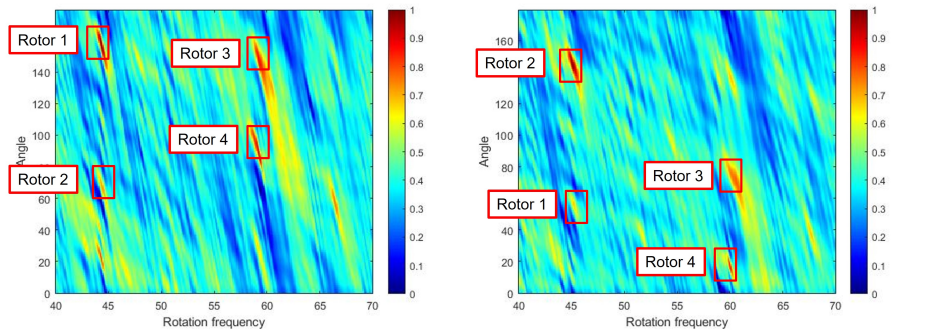**Number of rotor estimation**

Figure 5.24 illustrates the 2D grid search results with estimated range, velocity, and rotor magnitude of the DJI M200 measurement for two consecutive CPIs. The 4 strong peaks can be observed, which correspond to the 4 rotors of the drone DJI M200. However, in addition to these 4 marked positions, there exist other strong peaks at positions such as $\{44 Hz, 23°\}$ and $\{67 Hz, 55°\}$ that are introduced by the more complicated blade geometry and coupling of the rotation frequencies. With false alarm removal approaches and tracking of the rotor position, most of the noise and coupling components can be removed, and the energy of the correct combinations of rotor parameters is integrated, and the final results are illustrated in Figure 5.25. Figure 5.25a gives the integrated detection results of the grid search output. The 4 clusters with the densest distribution and likelihoods are recognized as the rotor positions with estimated parameters given in Table 5.8 where 2 rotors at a rotation frequency around 44 Hz and the other 2 around 59 Hz are estimated. Figure 5.25b gives the results of the rotation frequency estimation from the Cepstrogram analysis and 2 rotation frequencies at 59 and 44 Hz are detected. However, because of limited resolutions, the number of rotors cannot be distinguished. These results are further validated with the motor speed recorded in the flight log data shown in Figure 5.25c where four curves correspond to the rotation speed of four rotors, which are 42.7, 44.9, 59.7 and 59.7 Hz. Therefore, agreement has been reached on the estimation results from the proposed number of rotor and rotation frequency estimation algorithms.
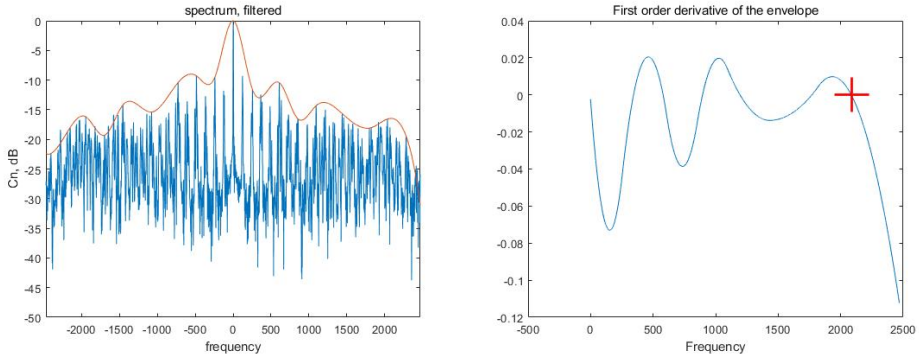
(a) Envelope of the spectrum

(b) First-order derivative of the envelope

Figure 5.23: Spectrum-based blade length analysis from measurement of DJI M600

5

(a) Grid search output for number of rotor estimation at CPI = 40

(b) Grid search output for number of rotor estimation at CPI = 41

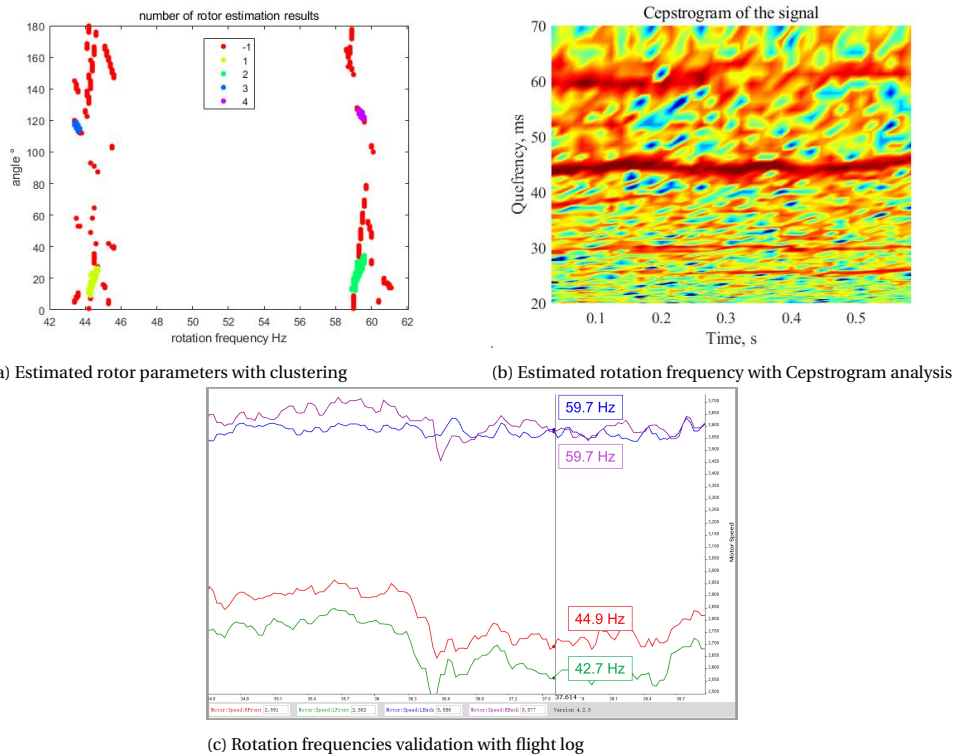Figure 5.24: Grid search result of DJI M200

(a) Estimated rotor parameters with clustering

(b) Estimated rotation frequency with Cepstrogram analysis

(c) Rotation frequencies validation with flight log

Figure 5.25: Number of rotor estimation results

	Rotor 1	Rotor 2	Rotor 3	Rotor 4
Estimation results {Rotation frequency, angle}	{44.4 Hz, 18.3° }	{43.6 Hz, 116° }	{59.3 Hz, 23.6° }	{59.4 Hz, 123.8° }

Table 5.8: Estimated rotation frequencies and angles

5.5. CONCLUSION

In this chapter, the simulation settings and processing procedures of the TBD with particle filter and drone characteristics estimation are presented and evaluated. The proposed method is first validated and analyzed with synthetic data, and then experimental measurements are used to verify the effectiveness of the algorithms. The observations, results and analysis presented in the chapter can be summarized as follows:

1. The simulation environment, radar parameters, and drones are introduced, providing different situations under test.

2. Independent examples are then given for the observations of TBD with a particle filter. With a coherent electromagnetic scattering model of the drone, the drone state including the range, velocity, rotation frequency, magnitude of the body and rotor, and the target existence probability are estimated. The algorithm shows superior performance in the detection of the target with a low SNR, achieving 87% and 95% detection probability at the SNR level of 0 dB and 5 dB, respectively, with a false alarm rate below 4%. The algorithm also provides the estimation results as prior information in the following drone characteristics estimation.

3. A fusion of spectrogram-based drone characteristics is presented to estimate constructional parameters of the drone, including the number of blades per rotor, blade length, as well as detection of multiple rotation frequency components. The results have shown self-consistent and robust estimation results with synthetic data.

4. The proposed model-based rotor number estimation is verified with both synthetic and experimental data. An estimation accuracy greater than 95% is achieved with SNR = 25 dB and 5 consecutive observations. The performance of the algorithm is discussed in terms of different SNR, the number of processing CPIs, and the processing interval of each CPI.

6

CONCLUSION AND FUTURE WORK

6.1. CONCLUSION

Radar-based drone detection, tracking, and characteristic estimation are challenging tasks due to the low RCS, low velocity, and high maneuverability of the drone. This research aims to tackle these difficulties and build a processing pipeline to detect, track, and estimate both dynamic and constructional parameters of the drone. To achieve this, a particle filter for track-before-detect with the coherent electromagnetic model of the drone is developed, and a fusion of spectrogram-based and novel model-based algorithms is proposed for the joint estimation of the rotor number and multiple rotation frequencies. The algorithms are first validated with synthetic data, and the performance is analyzed. The algorithms are then verified with experimental data, providing observations and results in agreement with the simulation.

The main contributions and novelty of the research are summarized below:

- An improved electromagnetic scattering model of the drone that takes into account the geometry of the drone is designed. This is used to develop the time-domain scattered signals simulation framework in relation to the configurable drone's parameters including the number of rotors and blades, their rotation frequency, and blades' length and initial orientation. An analysis is performed on how variations of these parameters would influence the scattered signals in the time and frequency domains, providing the fundamentals for the estimation of the critical drone characteristics.

- A novel particle filter for the TBD method is developed by applying the previously mentioned coherent electromagnetic scattering model of the drone to the measurement model, allowing a more detailed estimation of the dynamic state of the drone including the range, velocity, rotation frequency, intensity of the drone body and rotor as well as the probability of the existence of the target, taking advantage of TBD for detecting and tracking weak targets. The proposed algorithm achieved a detection probability of 95% at 5 dB SNR and 87% at 0 dB, outperforming the conventional CFAR detector.

- Novel fusion of spectrogram-based estimation pipeline with the proposed TBD estimator is developed that utilizes the information from the different spectrogram with short and long processing intervals. With the help of the TBD tracking algorithm, it implements the estimation of constructional parameters of the drone including the number of blades per rotor, the blade length, and their rotation frequencies per rotor.

- A novel model-based method for the number of rotors as well as corresponding rotation frequencies and blades' initial orientation angles estimation is developed. A 2D grid search is used to find the optimal rotation frequencies and blades angles parameters for every rotor. Tracking-aided false alarm removal and rotor likelihood integration are designed to improve the accuracy of the estimation. The proposed algorithm achieved estimation accuracy up to 96% with 25 dB SNR and consecutive observations of 5 CPIs.

From this research, the constructional and kinematic characteristics of the drone are estimated, including the number of rotors, the number of blades per rotor, the length of the blade and the multirotation frequencies. These characteristics could be further used for drone classification and identification. In addition, with precise knowledge of the frequency of the rotors, it provides important features in analyzing the payload of the drone [39][44].

6

6.2. Limitations and Future Work

Although the proposed TBD with particle filter, spectrogram-based, and model-based drone characteristics estimation have shown accurate detection and estimation results with synthetic measurements, the research has the following limitations:

- A simplified electromagnetic scattering drone model with a single rotor component is considered in TBD as the measurement model. This is done to reduce the complexity and dimensionality of the state parameters. However, this model is able to estimate the strongest rotation frequency components if the rotors have very different rotation frequencies, and the estimation accuracy of the state could be decreased if the particles are trapped by local maxima likelihood from other rotor parameters.

- The proposed number of rotor estimation requires an accurate estimation of the drone range and velocity. A large estimation error would introduce a non-negligible phase component and decrease the grid search performance.

- The algorithms are only validated with a limited number of measurements, and there is a lack of more accurate recording and labeling of the rotor dynamics to match specific measurement data and time.

In addition to the limitations mentioned above, a list of future research is formulated that could solve the limitations and further extend the research:

- Introduction of more dynamic models in the TBD algorithm. The current algorithm only uses the nearly constant values model. Although the accelerations and

change of the motion are accommodated by the process noise covariance matrix, this would require an extra number of CPIs for particles to converge and achieve an accurate estimation. By utilizing and transiting between multiple hypotheses of target dynamic models, it would better track and estimate the drone state under different maneuver motions.

- More detailed electromagnetic scattering modeling of the drone. This model is using in the TBD measurement model and the estimation of the rotor number would benefit from a more accurate representation of the drone's scattered signal. This includes consideration of the geometry, orientation, and more accurate RCS modeling of the blade.

6

ACKNOWLEDGEMENTS

Two years of study at TU delft have become a valuable experience for me. I will remember those hard-working days and nights accompanied by the broadcast of the closing of the EWI building. Even those hardest days have turned into my cherished memory as this has been one of my purest periods studying, seeking, and exploring knowledge.

I would like to express my great gratitude to my daily supervisor Dr.Oleg Krasnov. During the weekly meeting, he has provided enthusiastic encouragement, continuous guidance, and inspiring suggestions to my work. He also helps me build the academic skills in writing, documenting, and presenting which would be beneficial to me in the long run. I am deeply grateful to Prof. Alexander Yarovoy. His wonderful lectures on electromagnetic waves and ultra-wideband systems have helped build my fundamental knowledge and lead me to the radar-related field.

I also would like to thank Dr. Francesco Fioranelli and MS3 PhD candidates. From the discussions with them, I have received generous help, insightful suggestions, and critical feedback. I am grateful to my peer students, with whom I have worked together by discussing and overcoming many problems that we encountered.

Last but not least, I would like to thank my families. Their care and concern always support me and help me go through all the hard time.

My time as a student on campus is ending, but the methodology and wisdom I learned would help me explore the road ahead.

BIBLIOGRAPHY

[1] B. Jiang, J. Yang, and H. Song, "Protecting privacy from aerial photography: State of the art, opportunities, and challenges," in *IEEE INFOCOM 2020 - IEEE Conference on Computer Communications Workshops (INFOCOM WKSHPS)*, 2020, pp. 799–804.

[2] R. Merkert and J. Bushell, "Managing the drone revolution: A systematic literature review into the current use of airborne drones and future strategic directions for their effective control," *Journal of Air Transport Management*, vol. 89, p. 101929, 2020. [Online]. Available: https://www.sciencedirect.com/science/article/pii/S0969699720305123

[3] S. M. Giray, "Anatomy of unmanned aerial vehicle hijacking with signal spoofing," in *2013 6th International Conference on Recent Advances in Space Technologies (RAST)*, 2013, pp. 795–800.

[4] J. P. West, C. A. Klofstad, J. E. Uscinski, and J. M. Connolly, "Citizen support for domestic drone use and regulation," *American Politics Research*, vol. 47, no. 1, pp. 119–151, 2019. [Online]. Available: https://doi.org/10.1177/1532673X18782208

[5] M. Benyamin and G. H. Goldman, "Acoustic detection and tracking of a class i uas with a small tetrahedral microphone array," 2014.

[6] I. Guvenc, F. Koohifar, S. Singh, M. L. Sichitiu, and D. Matolak, "Detection, tracking, and interdiction for amateur drones," *IEEE Communications Magazine*, vol. 56, no. 4, pp. 75–81, 2018.

[7] M. Saqib, S. Daud Khan, N. Sharma, and M. Blumenstein, "A study on detecting drones using deep convolutional neural networks," in *2017 14th IEEE International Conference on Advanced Video and Signal Based Surveillance (AVSS)*, 2017, pp. 1–5.

[8] D. K. Behera and A. Bazil Raj, "Drone detection and classification using deep learning," in *2020 4th International Conference on Intelligent Computing and Control Systems (ICICCS)*, 2020, pp. 1012–1016.

[9] H. M. Finn, "Adaptive detection mode with threshold control as a function of spatially sampled clutter level estimates," 1968.

[10] A. Coluccia, G. Parisi, and A. Fascista, "Detection and classification of multirotor drones in radar sensor networks: A review," *Sensors*, vol. 20, no. 15, 2020. [Online]. Available: https://www.mdpi.com/1424-8220/20/15/4172

[11] M. Ezuma, O. Ozdemir, C. K. Anjinappa, W. A. Gulzar, and I. Guvenc, "Micro-uav detection with a low-grazing angle millimeter wave radar," in *2019 IEEE Radio and Wireless Symposium (RWS)*, 2019, pp. 1–4.

[12] M. Jian, Z. Lu, and V. C. Chen, "Drone detection and tracking based on phase-interferometric doppler radar," in *2018 IEEE Radar Conference (RadarConf18)*, 2018, pp. 1146–1149.

[13] F. Hoffmann, M. Ritchie, F. Fioranelli, A. Charlish, and H. Griffiths, "Micro-doppler based detection and tracking of uavs with multistatic radar," in *2016 IEEE Radar Conference (RadarConf)*, 2016, pp. 1–6.

[14] M. Jahangir and C. Baker, "Robust detection of micro-uas drones with l-band 3-d holographic radar," in *2016 Sensor Signal Processing for Defence (SSPD)*, 2016, pp. 1–5.

[15] X. Guo, C. S. Ng, E. de Jong, and A. B. Smits, "Micro-doppler based mini-uav detection with low-cost distributed radar in dense urban environment," in *2019 16th European Radar Conference (EuRAD)*, 2019, pp. 189–192.

[16] D. Salmond and H. Birch, "A particle filter for track-before-detect," in *Proceedings of the 2001 American Control Conference. (Cat. No.01CH37148)*, vol. 5, 2001, pp. 3755–3760 vol.5.

[17] Y. Boers and J. Driessen, "Particle filter based detection for tracking," in *Proceedings of the 2001 American Control Conference. (Cat. No.01CH37148)*, vol. 6, 2001, pp. 4393–4397 vol.6.

[18] B. Zhichao, J. Qiuxi, and L. Fangzheng, "Multiple model efficient particle filter based track-before-detect for maneuvering weak targets," *Journal of Systems Engineering and Electronics*, vol. 31, no. 4, pp. 647–656, 2020.

[19] B. Knoedler, C. Steffes, and W. Koch, "Detecting and tracking a small uav in gsm passive radar using track-before-detect," in *2020 IEEE Radar Conference (RadarConf20)*, 2020, pp. 1–6.

[20] K. Kim, M. Üney, and B. Mulgrew, "Estimation of drone micro-doppler signatures via track-before-detect in array radars," in *2019 International Radar Conference (RADAR)*, 2019, pp. 1–6.

[21] K. Kim, M. Uney, and B. Mulgrew, "Coherent track-before-detect with micro-doppler signature estimation in array radars," *IET Radar Sonar ? Navigation*, 04 2020.

[22] K. Singh, D. Shashikiran, J. S. Rengarajan, and A. Vengadarajan, "Helicopter classification using time-frequency and tomographic imaging techniques," in *2019 10th International Conference on Computing, Communication and Networking Technologies (ICCCNT)*, 2019, pp. 1–5.

[23] A. K. Singh and Y. H. Kim, "Automatic measurement of blade length and rotation rate of drone using w-band micro-doppler radar," *IEEE Sensors Journal*, vol. PP, pp. 1–1, 12 2017.

[24] R. I. A. Harmanny, J. J. M. de Wit, and G. P. Cabic, "Radar micro-doppler feature extraction using the spectrogram and the cepstrogram," in *2014 11th European Radar Conference*, 2014, pp. 165–168.

[25] P. Klaer, A. Huang, P. Sévigny, S. Rajan, S. Pant, P. Patnaik, and B. Balaji, "An investigation of rotary drone herm line spectrum under manoeuvering conditions," *Sensors*, vol. 20, no. 20, 2020. [Online]. Available: https://www.mdpi.com/1424-8220/20/20/5940

[26] B. K. Kim, H.-S. Kang, and S.-O. Park, "Drone classification using convolutional neural networks with merged doppler images," *IEEE Geoscience and Remote Sensing Letters*, vol. 14, no. 1, pp. 38–42, 2017.

[27] L. Fuhrmann, O. Biallawons, J. Klare, R. Panhuber, R. Klenke, and J. Ender, "Micro-doppler analysis and classification of uavs at ka band," in *2017 18th International Radar Symposium (IRS)*, 2017, pp. 1–9.

[28] R. Rzemien, "Coherent radar: Guest editor's introduction," 1997.

[29] N. Giordano, *College Physics: Reasoning and Relationships.* Brooks/Cole, 2013. [Online]. Available: https://books.google.com.cu/books?id=fz8LYAAACAAJ

[30] V. Chen, F. Li, S.-S. Ho, and H. Wechsler, "Micro-doppler effect in radar: phenomenon, model, and simulation study," *IEEE Transactions on Aerospace and Electronic Systems*, vol. 42, no. 1, pp. 2–21, 2006.

[31] O. Krasnov and A. Yarovoy, "Radar micro-doppler of wind turbines: Simulation and analysis using rotating linear wire structures," *International Journal of Microwave and Wireless Technologies*, vol. 7, pp. 1–9, 06 2015.

[32] Y. Cai, O. Krasnov, and A. Yarovoy, "Simulation of radar micro-doppler patterns for multi-propeller drones," in *2019 International Radar Conference (RADAR)*, 2019, pp. 1–5.

[33] H. Hou, Z. Yang, and C. Pang, "Rotor uav's micro-doppler signal detection and parameter estimation based on frft-fsst," *Sensors*, vol. 21, no. 21, p. 7314, 2021.

[34] A. Doucet, S. Godsill, and C. Andrieu, "On sequential monte carlo sampling methods for bayesian filtering," *Statistics and Computing*, vol. 10, 04 2003.

[35] A. Doucet, N. Freitas, K. Murphy, and S. Russell, "Sequential monte carlo methods in practice," 01 2013.

[36] R. Deters, S. Kleinke, and M. Selig, "Static testing of propulsion elements for small multirotor unmanned aerial vehicles," 06 2017.

6

[37] M. Ester, H.-P. Kriegel, J. Sander, and X. Xu, "A density-based algorithm for discovering clusters in large spatial databases with noise," in *Proceedings of the Second International Conference on Knowledge Discovery and Data Mining*, ser. KDD'96. AAAI Press, 1996, p. 226–231.

[38] E. Sejdić, I. Djurović, and J. Jiang, "Time–frequency feature representation using energy concentration: An overview of recent advances," *Digital Signal Processing*, vol. 19, no. 1, pp. 153–183, 2009. [Online]. Available: https://www.sciencedirect.com/science/article/pii/S105120040800002X

[39] M. Daković and L. Stanković, "Estimation of sinusoidally modulated signal parameters based on the inverse radon transform," in *2013 8th International Symposium on Image and Signal Processing and Analysis (ISPA)*, 2013, pp. 302–307.

[40] A. K. Singh and Y.-H. Kim, "Automatic measurement of blade length and rotation rate of drone using w-band micro-doppler radar," *IEEE Sensors Journal*, vol. 18, pp. 1895–1902, 2018.

[41] B. P. Bogert, "The quefrency analysis of time series for echoes : cepstrum, pseudo-autocovariance, cross-cepstrum and saphe cracking," 1963.

[42] B. Lakha, "Short time cepstrum analysis method for pitch estimation of an arbitrary speech signal using matlab," *IJRECE VOL. 5 ISSUE 3 JULY.-SEPT. 2017*, vol. 5, pp. 1–4, 07 2017.

[43] R. Harmanny, J. Wit, and G. Premel-Cabic, "Radar micro-doppler mini-uav classification using spectrograms and cepstrograms," *International Journal of Microwave and Wireless Technologies*, vol. 7, pp. 1–9, 06 2015.

[44] J. J. De Wit, D. Gusland, and R. P. Trommel, "Radar measurements for the assessment of features for drone characterization," in *2020 17th European Radar Conference (EuRAD)*, 2021, pp. 38–41.

A

ALGORITHMS

A.1. RESAMPLING ALGORITHM

$\left[\left\{ \mathbf{x}_k^{j*}, w_k^j, i^j \right\}_{j=1}^N \right] = \text{RESAMPLE} \left[\left\{ \mathbf{x}_k^i, w_k^i \right\}_{i=1}^N \right]$

Initialize the CSW: $c_1 = w_k^1$

for $i = 2 : N$ **do**

    Construct CSW: $c_i = c_{i-1} + w_k^i$

end for

Start at the bottom of the CSW: $i = 1$

Draw a starting point: $u_1 \sim \mathcal{U} \left[0, N^{-1} \right]$

for $j = 1 : N$ **do**

    Move along the CSW: $u_j = u_1 + N^{-1}(j-1)$

    while $u_j > c_i$ **do**

        * $i = i + 1$

    end while

    Assign sample: $\mathbf{x}_k^{j*} = \mathbf{x}_k^i$

    Assign weight: $w_k^j = N^{-1}$

    Assign parent: $i^j = i$

end for

A.2. REGIME TRANSITION ALGORITHM

A

$$\left[\{r_k^n\}_{n=1}^N\right] = \text{RT}\left[\{r_{k-1}^n\}_{n=1}^N, \Pi\right]$$

for $i = 1 : s$ **do**
 $\quad -c_i(0) = 0$
 $\quad$**for** $j = 1 : s$ **do**
 $\quad\quad * \ c_i(j) = c_i(j-1) + \pi_{ij}$
 $\quad$**end for**
end for
for $n = 1 : N$ **do**
 $\quad$Draw $u_n \sim \mathcal{U}[0,1]$
 $\quad$Set $i = r_{k-1}^n$
 $\quad m = 1$
 $\quad$**while** $(c_i(m) < u_n)$ **do**
 $\quad\quad m = m + 1$
 $\quad$**end while**
 $\quad$Set $r_k^n = m$
end for